A COMPREHENSIVE MODEL FOR ENERGY TRANSPORT AND ABLATION OF METAL FILMS INDUCED BY ULTRASHORT PULSED LASERS

A Dissertation

Presented to

the Faculty of the Graduate School

at the University of Missouri-Columbia

In Partial Fulfillment

of the Requirements for the Degree

Doctor of Philosophy

---

by

Yunpeng Ren

Dr. Jinn-Kuen Chen, Dissertation Supervisor

Dr. Yuwen Zhang, Dissertation Co-Supervisor

December 2012

The undersigned, appointed by the dean of the Graduate School, have examined the dissertation entitled

A Comprehensive Model for Energy Transport and Ablation of Metal Films Induced by Ultrashort Pulsed Lasers

Presented by Yunpeng Ren,

A candidate for the degree of Doctor of Philosophy,

And hereby certify that, in their opinion, it is worthy of acceptance.

_____

Professor Jinn-Kuen Chen

_____

Professor Yuwen Zhang

_____

Professor Douglas Smith

_____

Professor Hongbin Ma

_____

Professor Fu-Hung Hsieh

ACKNOWLEDGEMENT

I would like to express my deepest appreciation to my supervisor, Dr. J. K. Chen and Dr. Yuwen Zhang, who continuously direct me in every stage of my Ph.D. study with great patience. Their spirit of hard working and strictness in academy impresses me much and this will be a great treasure in all my life. Without their persistent guidance and support, this dissertation would not be possible.

I would also like to thank the committee for their guidance and participation. Deep appreciation is also given to Dr. Jing Huang, who directed me much in programming and offered valuable discussion in early stage of the research.

A great thank is given to my wife who takes care of and encourage me in every day. Her daily service to me and care both in heart and spirit give me much support without which I cannot continue and finish my work.

Great gratitude is also given to my parents who love and encourage me by standing by me to overcome all difficulties in study and life. Their sacrificial love is my drive to reach my goal in all my life.

Many thanks also are given to my officemates, Tao Jia, Yijin Mao, Nazia Afrin, Sejung Kim, Hamid Seyf, Zheng Li, Pengfei Ji, Xin Dou, Qicheng Chen, Hongbo Kang, for their help and sharing of joy in daily life.

Finally but not lastly, I would like to thank my Holy Father who loves me and gives me strength to face everything.

TABLE OF CONTENTS

LIST OF FIGURES

LIST OF TABLES

NOMENCLATURE

A	average absorption
A_e, B_l	material constants for electron relaxation time
B	weighing factor of Lorentz oscillators in critical point model
B_e	coefficient for electron heat capacity (J/m^3-K^2)
C	heat capacity (J/m^3-K)
c	speed of light in vacuum (m/s)
c_p	specific heat (J/kg-K)
c_s	speed of sound (m/s)
$\hat{e}$	charge of an electron (C)
f	liquid fraction
f_1	normal refractive index
f_2	extinction coefficient
f_L	weighing factor of Lorentz oscillators in extended Drude model
G	electron-lattice coupling coefficient (W/m^3-K)
G_{rt}	electron-lattice coupling coefficient at room temperature (W/m^3-K)
h	Plank constant (m^2kg/s)
h_m	latent heat of fusion (J/kg)
$h_{\ell v}$	latent heat of evaporation (J/kg)
J_o	heat source fluence (J/m^2)
k	thermal conductivity (W/m-K)
k_B	Boltzmann constant
k_F	Fermi velocity (m/s)

L	thickness of the metal film (m)
m_e	mass of an electron (kg)
m_{opt}	effective mass of an electron (kg)
M	molar mass (kg/kmol)
N	density of free electron ($1/cm^3$)
p	pressure (Pa)
p_c	critical pressure (Pa)
q	phonon wave vector (m^{-1})
q''	heat flux (W/m^2)
R	surface reflectivity
R_g	specific gas constant (J/kg-K)
R_u	universal gas constant (J/kmol-K)
s	interfacial location (m)
S	volumetric laser heat source (W/m^3)
t	time (s)
t_p	FWHM pulse width (s)
T	temperature (K)
T_c	critical temperature (K)
T_F	Fermi temperature (K)
T_m	melting point (K)
u	interfacial velocity (m/s)
$\bar{v}$	electron drifting velocity (m/s)
v_c	critical specific volume (m^3/kg)

u_0 maximum interfacial velocity (m/s)

x coordinate (m)

Greek Symbols

α absorption coefficient (m^{-1})

β electric field coefficient (V/K)

γ damping coefficient in critical point model (1/s)

γ_D Lorentz oscillator damping coefficient in extended Drude model (1/s)

Γ broadening of Lorentzian term in critical point model ($rad \cdot s^{-1}$)

Γ_L Lorentz oscillators spectral width in extended Drude model ($rad \cdot s^{-1}$)

δ optical penetration depth (m)

ε total emissivity

ε_1 real part of the dielectric function

ε_2 imaginary part of the dielectric function

ε_d d-band energy (eV)

ε_F Fermi energy (eV)

ε_∞ dielcetric constant

μ_0 mobility of electrons at room temperature ($m^2 s^{-1} V^{-1}$)

ρ density (kg/m^3)

ρ_F distribution of occupied electronic states

σ Stefan-Boltzmann constant ($W/m^2 \text{-} K^4$)

τ variable of integration that denotes temperature (K)

τ_e relaxation time of electrons (s)

ϕ phase of Lorentzian term in critical point model

ω laser frequency (Hz)

ω_D plasma frequency (Hz)

Ω energy of gap of Lorentzian term in critical point model (rad·s^{-1})

Ω_L Lorentz oscillators strength in extended Drude model (rad·s^{-1})

Superscripts

0 last time step

Subscripts

e electron

eq thermal equilibrium state

i initial condition

l lattice

ℓ liquid

ℓv liquid-vapor interface

s solid

$s\ell$ solid-liquid interface

sur surface

∞ ambient environment

ABSTRACT

A comprehensive laser material ablation model, based on classical and semi-classical two-temperature models (TTM) together with a temperature-dependent optical model, was developed to describe energy transport, ultrafast phase changes, and material ablation of metal films irradiated by ultrashort laser pulses.

The extended Drude and the critical point model were proposed in this work to describe temperature-dependent optical reflectivity and absorption coefficient for gold and copper, respectively. After validated with experimental data, the two optical models were incorporated into the TTM to simulate laser energy deposition and the resulting thermal response, ultrafast phase changes from solid to liquid and from liquid to vapor, and phase explosion of metal films irradiated by ultrashort laser pulses. It was found that dynamic optical properties could play a very important role in modeling ultrashort-pulsed laser interactions with metal materials. Those constant reflectivity and absorption coefficient at room temperature (RT) which have been widely used in the TTM modeling are only suited for very low laser fluences.

A study for the classical and semi-classical TTM was performed for gold films. In the semi-classical TTM, due to the effect of electron drifting, slightly lower electron and lattice temperatures were obtained compared to those calculated by the classical TTM under the same laser irradiation conditions. Higher laser fluence and longer pulse duration could result in more distinct difference between the two models. The simulated

melting velocity and depth were also compared, respectively; so were those of the evaporation. It was found that the semi-classical TTM results in less severe melting and vaporization than the classical TTM.

For multi-pulse irradiations, two mechanisms, laser energy absorption and heat conduction loss, are competing with each other for the thermal response. Thus, the effects of pulse number and separation time between two pulses in a femtosecond pulse burst were investigated. The results showed that with the same total energy in a laser burst, more pulses with a shorter separation time, e.g., 1 ps, or fewer pulses with a longer separation time, e.g., 100 ps, could achieve higher lattice temperature. For the dual (nanosecond + femtosecond) laser beams, lattice temperature could be increased by setting the pulse separation time in a femtosecond laser burst as short as possible, e.g., 1 ps.

Laser material ablations were investigated by including phase explosion to the above thermal model. It was shown that for high laser fluences phase explosion is a dominating mechanism in material ablation, while vaporization for low laser fluences. The simulated ablation depths correlated very well with existing experimental data over a broad range of fluences, 0.6 – 30 J/cm^2. For laser ablations by laser bursts, it was also found that with very short separation times, e.g., 1 ps and 10 ps, the advantage of the burst mode is not evident in laser material ablation. However, with longer separation time, e.g., longer than 50 ps, a burst mode can ablate much more material than a single pulse.

Keywords: Ultrafast laser, Two-temperature model, Critical point model, Superheating, Laser ablation, Burst mode

CHAPTER 1: INTRODUCTION

1.1 Introduction

Light Amplification by Stimulated Emission of Radiation (LASER) is a mechanism for emitting electromagnetic radiation via the process of stimulated emission. The emitted laser light is (usually) a spatially coherent, narrow low-divergence beam, which can be manipulated with optical lenses. A laser beam of coherent light differentiates it from light sources that emit incoherent light of random phase varying with time and position. Since invented in 1960s, lasers have been widely used in many things in our life. Based on their property of being highly directional and focused, the following are some examples of different types of applications [1]:

1) Medical Field:

- Bloodless surgery
- Laser healing
- Surgical treatment
- Kidney stone treatment
- Eye treatment

2) Industry:

- Cutting
- Welding
- Material heat treatment

- Non-contact measurement of parts

3) Commercial:

- Barcode scanners
- Thermometers
- Laser pointers

4) Military:

- Marking targets
- Guiding munitions
- Missile defense
- Electro-optical countermeasures (EOCM)

To date, thousands of lasers have been discovered. Basically all these lasers can be divided into following types [2]:

- Gas lasers
- Chemical lasers
- Metal-vapor lasers
- Dye lasers
- Solid-state lasers
- Semiconductor lasers

Due to the unique properties of laser, laser-matter interaction phenomena have been studied and many valuable works have been reported in the past half century. While in the last two decades, the advancement of modern laser technologies has brought laser

pulses into the femtosecond (fs) regime, which brings new challenges to understand physics and mechanism of laser-material interactions and opens up new applications that conventional lasers are unable to achieve [3-11].

1.2 Femtosecond Pulsed Lasers

Femotosecond lasers have distinct advantages over the ordinary even nanosecond pulse lasers [12]. The extremely short pulse widths (as short as a few femtoseconds, i.e., 10^{-15} s) make femtosecond lasers easy to achieve very high peak laser intensity with low pulse energy. For example, the intensity of a femtosecond laser pulse can be as high as 10^{21} W/m^2, compared to that of a nanosecond laser pulse (10^{12} W/m^2) [13]. Together with the very short material interaction time, the extremely high laser intensity makes femtosecond lasers possible to precisely process any kinds of soft and hard material (including diamond) with minimum collateral thermal damage. This is due to the unique feature that a femtosecond pulse laser pulse can interact with its target without or with minimal heat transferring to the surrounding material. Therefore, the heat affected zone (HAZ) can be very precise as desirable for applications that cannot be achieved by nanosecond pulse lasers, for which the surrounding material of the laser spot is significantly affected. The unique feature of extremely high laser intensity in such a short duration of time have many applications with some examples as follows [12,14,15]:

1) Precise surgeries that make more precise incisions and much less collateral tissue damage, such as LASIK (Laser-Assisted in Situ Keratomileusis) surgery, neurosurgery, cancer treatment, etc.

2) Treatment of tooth decay without harming the rest of tooth structure

3) Creation of super clean channels in silicon chips for biomedical applications

4) Nano and micro machining and surface structuring

1.3 Femtosecond Laser-Metal Interaction Phenomena

Due to the advantages of femtosecond lasers mentioned above, in the last two decades, a new wave of research in physics, chemistry, bioscience and material science has been driven by the rapid advancement of ultrafast laser technology [16-20]. Among them, the interactions between femtosecond laser pulses and metals are one of the hottest topics and also an interest of this dissertation. The thermal phenomena resulting from femtosecond laser material interactions are significantly different from those that the traditional Fourier's Law of heat conduction can describe due to the follow reasons [13,21]:

1. The characteristic lengths of various heat carriers are comparable to the characteristic length of target/film thickness under consideration.

2. The characteristic time of the various heat carriers is comparable to the characteristic energy excitation time. During laser-metal interaction, the laser energy is first absorbed by electrons in a subsurface layer and then the following processes compete with one another [21]:

(1) Ballistic motion of the excited electrons into deeper parts of the material with a velocity close to Fermi velocity ($\approx 10^6$ m/s).

(2) Thermalization of electron temperature by collision among the excited electrons.

Once thermal equilibrium of the hot electrons is reached, a second time interval starts which is characterized by the Fermi distribution and electron temperature which in the beginning differs strongly from the lattice temperature. Such hot electron bath is initially localized within either the ballistic range or the optical absorption depth.

(3) Electron thermal energy diffusing into deeper parts of the electrons with a considerably slower speed than the ballistic motion.

(4) Cooling of the hot electrons by transferring their thermal energy to the surrounding lattice through electron-phonon coupling.

Therefore, a comprehensive model that can accurately describe laser energy deposition, ultrafast laser heating, ultrafast superheating and undercooling, and material ablation is needed for predicting the above thermal transport and the response such as melting, vaporization, phase explosion, and cooling.

1.4 Literature Survey

Because of the novel phenomena of interaction between ultrashort-pulsed laser pulses and matters, numerous theoretical and experimental investigations have been conducted in the past several decades. Among these works, various heat conduction models were proposed to describe the non-equilibrium thermal transport during the ultrafast heating process. In 1974, Anisimov et al. [3] pioneered a phenomenological two-temperature model (TTM) that describes non-equilibrium energy transport between electrons and lattice. It is a two-step heating model in which electrons are first heated by a laser pulse

and then transfer their thermal energy to heat up the lattice. A more rigorous, hyperbolic TTM was then derived based on Boltzmann transport equation by Qiu and Tien [22] in 1993. The thermal lagging is included in the constitutive equation of electrons in this model. Meanwhile, Tzou [23] developed a dual-phase-lag model to describe the non-equilibrium thermal transport between electrons and lattice by considering the delay effects of energy transport. In 2001, Chen and Beraun [24] proposed a dual-hyperbolic TTM by including thermal lagging in both heat conduction equations for electrons and lattice. As pointed out by Ashcroft and Mermin [25], an electric field can arise in a non-uniformly heated conductor in the absence of current. Non-equilibrium transport conditions will occur if the electric filed and the carrier gradient become excessively large [26]. This is particularly true for ultrashort pulse laser heating due to the fact that an extremely large gradient of electron temperature rapidly comes up in a very small geometry encountered. In order to accurately describe the non-equilibrium electron effects, Chen et al. [27] proposed a semi-classical TTM based on the Boltzmann transport equation. In this model, the two equations governing the electron momentum and energy are derived from Boltzmann transport equation. For the phonon subsystem, the thermal transport equation is the same as that used in the classical TTM. The main difference between the semi-classical and classical TTM is that the former exclusively takes into account the effect of the electron drifting which is caused by the resulting electric filed and the hot-electron kinetic pressure [27].

Besides the models themselves, thermophysical and optical properties are other key

factors that govern the model solution accuracy. The former, including thermal conductivities, heat capacities and relaxation times of electrons and lattice as well as the electron-phonon coupling factor, controls thermal transport and temperature distributions in a heated medium. The latter, including surface reflectivity and absorption coefficient, dictate laser energy deposition that influences the thermal response. In the early time of the numerical TTM study, the thermophysical properties employed are either constant or only adequate for low temperature and the surface reflectivity (R) and optical penetration depth (δ) are often arbitrarily assumed or kept constant [4,5,22,28]. In 1997, Anisimov and Rethfeld [29] made a progress by proposing an approximate formula for electron thermal conductivity based on the former results, which is suited for a broad range from low temperature to high temperature of low density plasmas. Jiang and Tsai [30] used a full-run quantum treatment to calculate numerically the electron heat capacity up to Fermi temperature. By analyzing the Jiang and Tsai's results of temperature-dependent electron heat capacity [30], Chen et al. [27] proposed a piece-wise function for the electron heat capacity that makes numerical simulation easier. Continuous improvements of electron thermophysical properties were made by Lin and Zhigilei [31] based on the electron density of state (DOS) and the effect of thermal excitation of electrons.

Comparing to the thermophysical properties, optical properties received less attention. In 2004, Jiang and Tsai [32] applied a TTM with Drude model that describes temperature-dependent optical properties to predict the crater shape of dielectrics generated by femtosecond lasers based on lattice temperature distribution. In their

approach, electron relaxation time was made a link between temperature and optical properties such as *R* and absorption coefficient (α). This work was extended to study energy transport and material removal for wide bandgap materials induced by femtosecond lasers [30] and processing of metal films by ultrashort laser pulse-train [33]. However, it is well known that the optical properties calculated by Drude model are generally higher than the experimental values. Recently, Sim et al. [34] studied this problem again. They used a different formula to calculate electron relaxation time but kept the Drude model for optical properties. Fisher et al. [35,36] modified the Drude model by including the interband transition effect to evaluate *R* and α for aluminum [35] and copper [36]. Fairly good comparisons of their model with experimental data for average absorption were demonstrated. Although many valuable works have been done for optical properties of metals so far, it still makes researchers struggling to get a better way to accurately characterize those properties, particularly for high temperatures.

In experiment, many efforts have been made to investigate optical properties in the last several years. Vorobyev and Guo [37] studied the change of absorptance of copper processed by multi-pulse femtosecond laser. It was found that after irradiation, the absorptance of copper has a dramatically increase, meaning that the *R* is in a big reduction. In 2008, the same group studied the same problem with more metals [38]. All the results showed that, the reflectivity of the metal could be very low after irradiated by femtosecond laser. All these investigations have proved that the surface reflectivity is under dramatical change with irradiation of femtosecond laser pulse. This suggests that

use of temperature-dependent optical properties, instead of constant values, is very necessary and crucial for simulating material interactions with ultrashort-pulsed lasers, either a single pulse or multi pulses.

In the investigations of thermal response of metals induced by ultrashort laser pulses, most of the works are confined to lattice temperature below the melting point. Some of them [13,27,39] studied ultrafast melting problems using different phase change models proposed by Kuo and Qiu [39] and Zhang and Chen [13], respectively. Basically, these two models are both good at describing the melting process of metals caused by ultrafast laser heating. Some works [27,40,41] also studied the evaporation using methods derived from Clausius-Clapeyron and Hertz-Knudsen-Langmuir equations. These approaches are valid for thermal equilibrium state but may not be suitable for the ultrafast liquid-vapor (L-V) phase change induced by ultrashort pulsed lasers since the heated material generally undergoes nonequilibrium, superheating process. Recently, Huang et al. [42] employed a vaporization wave model, proposed by Bennette [43] for nonequilibrium, superheating kinetics of volume vaporization in electrically exploded wires, to study the evaporation process in a metal thin film irradiated by a femtosecond laser pulse. The simulated evaporation velocity can be increased by 2-3 orders of those reported by Chowdhury and Xu [44].

It has been seen that until very recently, most of numerical investigations focus on interactions between a single laser pulse and metal materials. In reality, metals are usually treated by multiple laser pulses or even by laser pulse trains. In 2007, Jiang and Tsai [33]

investigated the multi-pulse laser irradiation problem by employing a TTM with temperature-dependent optical and thermophysical properties. Their results showed that the lattice temperature can be increased by splitting a single pulse into several smaller pulses that retain the same total energy. Later, Sim et al. [34] did a similar study and got similar results as Jiang and Tsai's [33]. In both works above, they considered a single laser burst composing of several pulses. Recently, Huang et al. [45] studied phase changes of a thin metal film irradiated by femtosecond laser pulse trains. The study showed that the metal film could be melted by a laser pulse train even when the laser fluence is low. A large melting depth could be obtained by a pulse train consisting of 10 bursts with 3 pulses in each burst.

In the past two decades, a great attention has also been paid to damage and ablation of metals by femtosecond lasers [27,44-46]. Schäfer et al. [47] studied metal ablation by picosecond lasers using a hybridized TTM and molecular dynamics. Their calculation results are in fairly good agreement with experimental results for low laser fluences [48, 49]. In the study finished by Fang et al. [50], the TTM together with temperature-dependent thermophysical and optical properties was employed. For the electron heat capacity, they simply assumed that it is linearly proportional to electron temperature which is only suited for electron temperature up to about one-tenth Fermi temperature (T_F) [25]. As for the optical properties, they used Maxwell equations describe the absorption coefficient and absorptance which only depend on electron temperature. A constant electron-phonon coupling factor was employed, and no heat

conduction was considered in the energy equation for lattice. Again, their numerical results [50] agreed with experimental data fairly well for low laser intensity but for high laser intensity (>10^{14} W/cm^2). Chen et al. [51] studied the damage threshold for a two-layer metal films. In this study, the electron heat capacity and thermal conductivity are similar to those used by Fang et al. [50], temperature-dependent electron-phonon coupling factor is used. However, constant optical properties are used in this study, and because of this, the simulated electron and lattice temperature are quite low for laser fluence 0.1 J/cm^2.

Under irradiation of femtosecond laser pulses, material could be removed due to either thermal ablation or non-thermal ablation. The former includes ultrafast phase changes through melting and vaporization as well as phase explosion if laser fluences are high enough, while the latter is caused by thermal stress, coulomb explosion, and/or hot electron blast when laser fluences are slightly higher than the ablation threshold. Although the non-thermal ablation can precisely process material with minimal damage, it suffers from its slow process due to low fluences. This, therefore, creates a need for developing a more efficient processing approach. One potential means, for example, is to process a material by irradiating high-fluence laser pulses and then followed by relatively low-fluence pulses.

Phase explosion was first proposed by Martynyuk [52] in 1974 for discharging a condensor into a wire, and later was augmented to high-power, very-short (< 1 ns) pulse laser heating [53-55]. For metals and metal-like materials heated by high-power

ultrashort-pulse lasers, the molten material can be heated up to well beyond the normal boiling point without boiling because the heating time is too short for the necessary heterogeneous nuclei to form. Instead, the material which is closer to the irradiated surface could be superheated to more or less the thermodynamic equilibrium critical temperature (T_c). At that high temperature, the tensile strength of the superheated, metastable liquid will fall to zero; consequently, homogeneous bubble nucleation occurs at an extremely high rate. As a result, the superheated material in the subsurface region relaxes explosively (or sputters) into a mixture of vapor and equilibrium liquid droplets and are immediately ejected from the bulk material.

Although an intensive number of the theoretical investigations about interactions between metal films and ultrafast laser pulses have been reported, most comparisons of the theoretical predictions with experimental measurements are confined to low-intensity cases [47,50]. This is because it is difficult to accurately model such ultrahigh intensity and short time events without accurate temperature dependent optical and thermophysical properties.

In this work, the classical and semi-classical TTM are employed to study thermal response of metals irradiated by high power ultrashort laser pulses. The efforts are focused on (1) investigation of temperature dependences of thermophysical and optical properties and (2) their impacts on the prediction of ultrafast thermal response in metal films, including solid-liquid (S-L) and liquid-vapor phase change as well as laser material ablation. The objectives and tasks are described in the following section.

1.5 Dissertation Objectives

The primary objective of this dissertation is to develop a comprehensive model together with accurate temperature-dependent optical properties and thermophysical properties to describe energy transport, phase changes including S-L and L-V phase change, and laser material ablation in metal films irradiated by single and multiple ultrafast laser pulses. In order to achieve this goal, several steps taken are listed below:

1. Obtain proper temperature-dependent thermophysical properties which are valid over a wide temperature range.
2. Propose optical models that are able to accurately characterize surface reflectivity and absorption coefficient for different materials at different temperatures.
3. Find suitable approaches to describe L-V phase change and laser ablation.
4. Validate the above models by comparing the simulation results with existing experimental data.
5. Study the optical and thermal responses of metal films irradiated by multiple ultrafast laser pulses to get better understanding of the phenomena.
6. Investigate ultrafast laser material ablation by employing the above model and compare the simulation results with existing experimental results to reveal the physics behind it.

Once this model is established, it can be used to simulate ultrafast laser heating in metal films either by a single laser pulse or multiple pulses. Thus, a better understanding of physics behind the interactions of ultrafast laser pulses with metals can be achieved,

shedding more light for new applications.

CHAPTER 2: MATHEMATICAL MODELS

2.1 Physical Model

The physical model of the problem considered here is shown in Fig. 2.1. A temporal Gaussian laser pulse is irradiated on the front surface ($x = 0$) of a free standing metal film, which has a thickness of L and initial temperature of T_i. The full width at half maximum (FWHM) and fluence of the laser beam are t_p and J_o, respectively. This problem can be approximated to be one-dimensional since the thermal affected depth is very small compared to the radius of the laser beam.

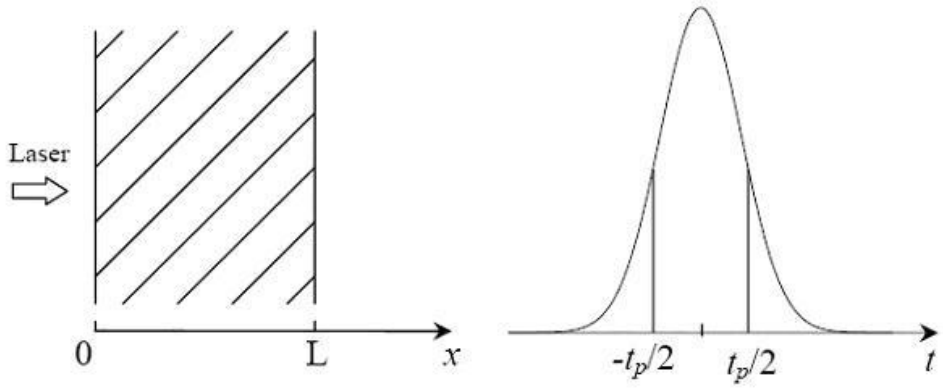

Figure 2.1 Laser irradiation on a thin film

2.2 Governing Equations

2.2.1 Two-Temperature Model

Since melting and vaporization are considered, a simplified version of the dual-hyperbolic TTM proposed by Chen and Beraun [24] is employed in this work. In this model, the energy equation of free electrons is given as

$$C_e \frac{\partial T_e}{\partial t} = \frac{\partial}{\partial x}(k_e \frac{\partial T_e}{\partial x}) - G(T_e - T_l) + S(x,t) \quad (1)$$

which is valid in the entire computational domain. The energy equation for lattice is

$$C_l \frac{\partial T_l}{\partial t} = \frac{\partial}{\partial x}(k_l \frac{\partial T_l}{\partial x}) + G(T_e - T_l) \quad (2)$$

which is valid in both solid and liquid phases but not at the S-L interface.

In the above model, *C* is heat capacity, *T* is temperature, *k* is thermal conductivity, *G* is electron-phonon coupling factor, *S* is laser heat density, *x* is space, and *t* is time. The subscript *e* and *l* denote electron and lattice.

2.2.2 Semi-Classical Two-Temperature Model

The semi-classical TTM proposed by Chen et al. [27] is derived from Boltzmann transport equation. In this model, the effect of electron drifting is considered during the energy transport process. The energy transport equation used for the phonon remains the same with that used in above classical TTM.

The electron momentum governing equation is [27]

$$m_e \frac{\partial \bar{v}}{\partial t} + m_e \bar{v} \cdot \nabla_x \bar{v} + [k_B(1 + \frac{T_e}{C_e}\frac{\partial C_e}{\partial T_e}) - \hat{e}\beta]\nabla T_e = -\frac{\hat{e} T_e \bar{v}}{\mu_0 T_l} \quad (3)$$

where m_e is electron mass, $\bar{v}$ is electron drifting velocity, k_B is Boltzmann constant, $\hat{e}$ is charge of an electron, μ_0 is mobility of electrons at room temperature (RT), and β is electric field coefficient.

The energy equations for electrons and phonons are [27]

$$C_e(\frac{\partial T_e}{\partial t} + \bar{v} \cdot \nabla_x T_e + \frac{2}{3} T_e \nabla_x \cdot \bar{v}) + \nabla_x \cdot \overline{Q_e} = -G(T_e - T_l) + S(x,t) \quad (4)$$

$$C_l \frac{\partial T_l}{\partial t} = \frac{\partial}{\partial x}(k_l \frac{\partial T_l}{\partial x}) + G(T_e - T_l) \tag{5}$$

2.3 Thermophysical Properties

Thermophysical properties control thermal transport and temperature distributions in an ultrafast heated medium. In this work, expressions for these properties which are valid over a broad range of temperature are utilized because high power laser pulses will be considered in this study.

To improve numerical simulation, Chen et al. [27] proposed a piecewise function to describe electron heat capacity (C_e) of gold at different temperature based on Jiang's and Tsai's work [30]:

$$C_e = \begin{cases} B_e T_e, & T_e < T_F / \pi^2 \\ 2B_e T_e / 3 + C_e^{'} / 3, & T_F / \pi^2 \le T_e < 3T_F / \pi^2 \\ Nk_B + C_e^{'} / 3, & 3T_F / \pi^2 \le T_e < T_F \\ 3Nk_B / 2, & T_e \ge T_F \end{cases} \tag{6}$$

where

$$C_e^{'} = B_e T_F / \pi^2 + \frac{3Nk_B / 2 - B_e T_F / \pi^2}{T_F - T_F / \pi^2}(T_e - T_F / \pi^2) \tag{7}$$

and B_e is a constant, T_F is Fermi temperature, N is density of free electron, k_B is Boltzmann constant.

After that, further work was done by Lin and Zhigilei [31] based on the electron density of state (DOS) and the effect of thermal excitation of electrons. They calculated the electron heat capacity by taking the derivative of the total electron energy density with respect to electron temperature. A polynomial function is proposed by Ren et al. [56]

for copper based on Lin's and Zhigilei's results [31]:

$$C_e(T_e)=\begin{cases}117.47T_e, & T_e<2000K\\ -20492.29908-26.64133T_e+0.09953T_e^2-1.12185\times10^{-5}T_e^3\\ +5.73532\times10^{-10}T_e^4-1.52388\times10^{-14}T_e^5+2.0436\times10^{-19}T_e^6\\ -1.09414\times10^{-24}T_e^7, & 2000K\le T_e\le T_F\end{cases} \tag{8}$$

Figure 2.2 shows Lin's and Zhigilei's data [31] and the curve-fitted results [56] for copper.

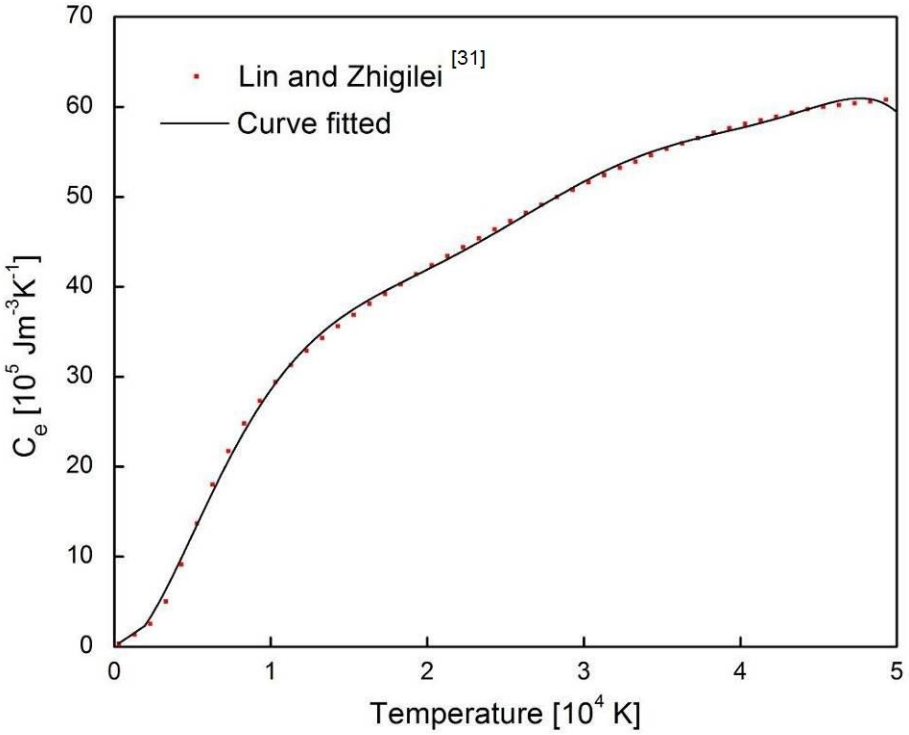

Figure 2.2 Temperature dependent electron heat capacity of copper

As for the electron thermal conductivity k_e, Anisimov and Rethfeld [29] proposed a formula which is valid up to temperature of low density plasmas:

$$k_e=\chi\frac{(\vartheta_e^2+0.16)^{5/4}(\vartheta_e^2+0.44)\vartheta_e}{(\vartheta_e^2+0.092)^{1/2}(\vartheta_e^2+\eta\vartheta_l)} \tag{9}$$

where $\vartheta_e = T_e / T_F$, $\vartheta_l = T_l / T_F$ with T_F denoting Fermi temperature. For the cases that $\vartheta_e << 1$, Eq. (9) reduces to the linear function

$$k_e = k_{eq}(\frac{T_e}{T_l}) \tag{10}$$

For metals at thermal equilibrium state, its thermal conductivity, k_{eq}, is the sum of the electron thermal conductivity, k_e, and the lattice thermal conductivity, k_l. In most cases, k_e dominates k_{eq} because free electrons contribute to the majority part of heat conduction. For the metals used in the study, i.e., gold and copper, k_l is usually taken to be 1% of k_{eq} [57],

$$k_l = 0.01 k_{eq} \tag{11}$$

In TTM, the electron-phonon coupling factor G accounts for heat exchange between hot electrons and lattice through collisions. In many previous works, constant G with different values is frequently employed in the theoretical investigations. Chen [58] derived a temperature-dependent G for gold with the simple form of

$$G = G_{rt}[\frac{A_e}{B_l}(T_e + T_l) + 1] \tag{12}$$

where G_{rt} is the coupling factor at RT, A_e and B_l are material constants for calculating electron relaxation time. Due to the higher collision rate of electrons in liquid, G is taken to be 20% higher than that of the solid [39].

Lin and Zhigilei [31] studied the coupling factor based on the assumption that the square of absolute electron-phonon scattering matrix element, when summed over scattering angles, is independent of electron states. Again the data are curve-fitted for

copper to be

$$G(T_e)=\begin{cases}0.56\times10^{17}, & T_e<2750K\\ 1.34096\times10^{17}-1.406879\times10^{14}T_e+5.987962\times10^{10}T_e^2-7.929516\times10^{6}T_e^3\\ +555.1959T_e^4-0.02327324T_e^5+6.04137\times10^{-7}T_e^6-9.5293\times10^{-12}T_e^7\\ +8.377\times10^{-17}T_e^8-3.15\times10^{-22}T_e^9, & 2750K\le T_e\le T_F\end{cases} \quad (13)$$

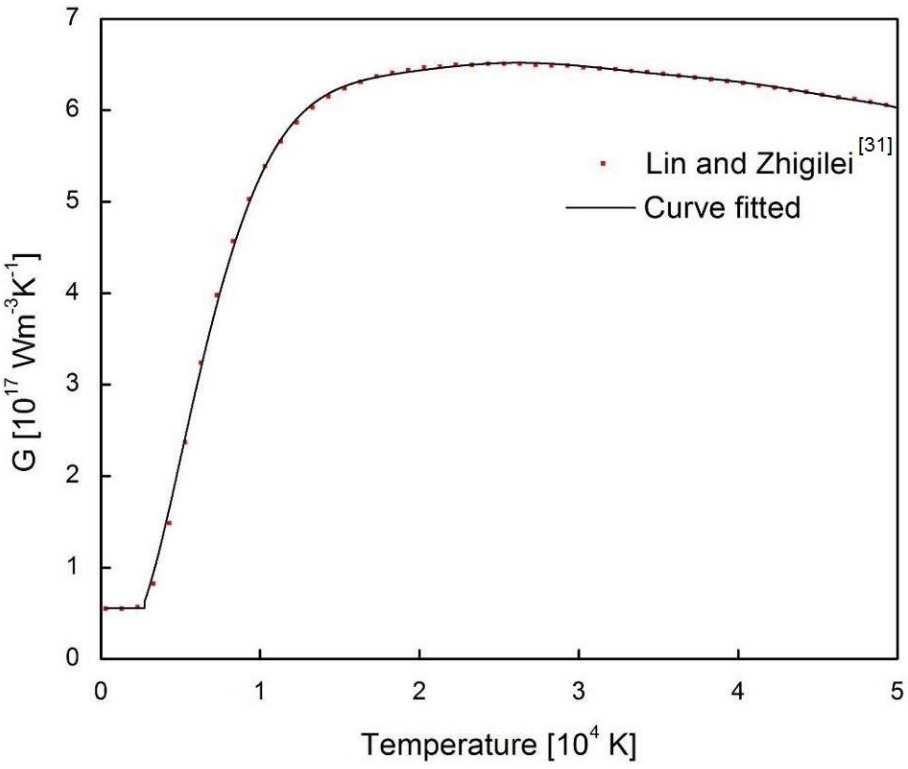

Figure 2.3 Temperature dependent electron-phonon coupling factor of copper

Figure 2.3 shows the computed data from Lin and Zhigilei [31] and the curve-fitted results from Ren et al. [56].

The laser heat source term in Eq. (1) and Eq. (4) can be described by the following equation [56,59] with temperature dependent optical properties *R* and α:

$$S(x,t) = 0.94J_o \frac{(1-R(0,t))}{t_p} \alpha(x,t) \exp[-\int_0^x \alpha(x,t)dx - 2.77(\frac{t}{t_p})^2] \quad (14)$$

Lasering is assumed to start at t = -2t_p and end at t = 2t_p. The laser energy outside this period of time is neglected in this work since it is too small to significantly alter the results.

2.4 Optical Properties

Optical properties dictate laser energy deposition and hence influence the thermal response. However, these properties have received less attention compared to thermophysical properties. Several attempts have been made to determine the optical properties R and α at RT in the range from UV to near infrared. For example, Rakic et al. [60] employed a Lorentz-Drude model with five Lorentzian terms to reflect the interband transition effect. Comparing with experimental data indicated their model was not precise enough in the vicinity of 2.0 eV for gold and 2.2 eV for copper where the interband transition takes place. Recently, Ren et al. [59] proposed an extended Drude model to describe the optical properties of gold at different temperatures. The expression of this model is shown below

$$\varepsilon_{DL} = \varepsilon_\infty - \frac{\omega_D^2}{\omega(\omega + i\gamma_D)} - \frac{f_L \Omega_L^2}{(\omega^2 - \Omega_L^2) + i\Gamma_L \omega} \quad (15)$$

where Ω_L and Γ_L stand for the oscillator strength and the spectral width of the Lorentz oscillators, respectively, and f_L is a weighting factor. With the values optimized for gold: ε_∞ = 5.9673, ω_D = 1.328 ×10^{16} Hz, Ω_L = 4.085 ×10^{15} Hz, Γ_L = 0.659 ×10^{15} Hz, and f_L = 1.09, the model fitted experimental data quite well in the range of 1.24 – 2.48eV (500 – 1000

nm). The details about the model can be found in reference [59].

Later, based on Drude model, Etchegoin [61] proposed a critical point model with two Lorentzian terms to calculate the permittivity for gold. After that, Vial and Laroche [62] found that the critical point model can be fairly good for silver also. Recently, Ren et al. [56] applied the model to copper and obtain satisfactory results in modeling thermal and optical response of copper films induced by ultrafast laser pulses. The critical point model with interband transition is written as

$$\varepsilon(\omega) = \varepsilon_\infty - \frac{\omega_D^2}{\omega^2 + i\gamma\omega} + \sum_{p=1}^{n} B_p \Omega_p \left(\frac{e^{i\phi_p}}{\Omega_p - \omega - i\Gamma_p} + \frac{e^{-i\phi_p}}{\Omega_p + \omega + i\Gamma_p} \right) = \varepsilon_1(x,t) + i\varepsilon_2(x,t) \quad (16)$$

where ε_∞ is dielectric constant, ω_D plasma frequency, ω laser frequency, γ damping coefficient which equals reciprocal of electron relaxation time (τ_e), n number of oscillators, B a weighting factor, and Ω, ϕ and Γ energy of gap, phase and broadening, respectively.

The parameters in Eq. (16) can be best fitted using a simulated annealing method [63]. The results are listed in Table 2 for copper with n = 3.

The electron relaxation time is often expressed in the form

$$\tau_e = \frac{1}{A_e T_e^2 + B_l T_l} \quad (17)$$

where A_e and B_l are material constant to be determined experimentally. The first term in the denominator represents electron-electron collision rates ($\upsilon_{e,e}$) and the second term represents electron-phonon collision rates ($\upsilon_{e,ph}$). However, the electron-phonon collision rate should in fact depend on both T_e and T_l [35]:

$$\upsilon_{e,ph} = \frac{\Xi^2}{8\pi\varepsilon_F k_F \rho s}\frac{m_{opt}}{m_e}\{\int_0^{q_b}\frac{\exp[\beta_l\hbar qs]+\exp[\beta_e\hbar qs]}{(\exp[\beta_l\hbar qs]-1)(\exp[\beta_e\hbar qs]+1)}q^4dq + \eta\int_0^{q_b}\frac{\exp[\beta_l\hbar qs]-\exp[\beta_e\hbar qs]}{(\exp[\beta_l\hbar qs]-1)(\exp[\beta_e\hbar qs]+1)}q^3dq + \frac{\exp[\beta_l\hbar q_b s]+\exp[\beta_e\hbar q_b s]}{(\exp[\beta_l\hbar q_b s]-1)(\exp[\beta_e\hbar q_b s]+1)}\times q_b \times \frac{(2k_F)^4 - q_b^4}{4} - \eta\times\frac{\exp[\beta_l\hbar q_b s]-\exp[\beta_e\hbar q_b s]}{(\exp[\beta_l\hbar q_b s]-1)(\exp[\beta_e\hbar q_b s]+1)}\times q_b^2\times(2k_F)^2\} \quad (18)$$

in which ε_F is Fermi energy, k_F Fermi velocity, ρ density, s longitudinal sound velocity, m_{opt} effective electron mass, m_e mass of an electron, q the phonon wave vector, $\beta_l = T_l/k_B$, $\beta_e = T_e/k_B$, and $\eta = 2m_{opt}s/\hbar$. The first two terms on the right-hand side of Eq. (18) are only significant for low temperature and can be neglected for RT and above. Using the similar method as Fisher et al. [35], the two parameters are found to be: Ξ = 3.99 eV, q_b = 8.97×10^9 m^{-1} for copper with m_{opt} = 1.39 m_e. In this work, the term B_lT_l in Eq. (17) is replaced with the collision rate $\upsilon_{e,ph}$ calculated from Eq. (17).

With known ε_1 and ε_2, the normal refractive index f_1 and extinction coefficient f_2 can be calculated by using following method

$$f_1(x,t) = \sqrt{\frac{\varepsilon_1(x,t)+\sqrt{\varepsilon_1^2(x,t)+\varepsilon_2^2(x,t)}}{2}} \quad (19)$$

$$f_2(x,t) = \sqrt{\frac{-\varepsilon_1(x,t)+\sqrt{\varepsilon_1^2(x,t)+\varepsilon_2^2(x,t)}}{2}} \quad (20)$$

The reflectivity R and absorption coefficient α can be determined by the Fresnel expression [64]

$$R(x,t) = \frac{(f_1(x,t)-1)^2 + f_2^2(x,t)}{(f_1(x,t)+1)^2 + f_2^2(x,t)} \quad (21)$$

$$\alpha(x,t) = \frac{2\omega f_2(x,t)}{c} \tag{22}$$

2.5 Solid-Liquid Phase Change

Under irradiation of laser pulses with high energies, phase changes including melting, evaporation, and even phase explosion could happen. The energy balance at the S-L interface is described by [65]

$$-k_{l,s}\frac{\partial T_{l,s}}{\partial x} - k_{l,\ell}\frac{\partial T_{l,\ell}}{\partial x} = \rho_\ell h_m u_{s\ell} \tag{23}$$

where $T_{l,s}$ and $T_{l,\ell}$ are solid and liquid lattice temperature respectively, ρ is mass density, h_m is latent heat of fusion, and $u_{s\ell}$ is S-L interfacial velocity.

For rapid melting/solidification processes, the moving velocity of the interface is dominated by nucleation dynamics instead of energy balance. For ultrafast laser irradiation, the velocity of the S-L interface is described by [39]

$$u_{s\ell} = u_0[1-\exp(-\frac{h_m}{R_g T_m}\frac{T_{l,I}-T_m}{T_{l,I}})] \tag{24}$$

where u_0 is the maximum interface velocity, R_g is the gas constant for metals, and $T_{l,I}$ is the interfacial temperature. The interfacial temperature, $T_{l,I}$, is higher than melting point, T_m, during melting which is under a superheating process and lower than the melting point during solidification which is under the undercooling process.

The S-L interfacial temperature $T_{l,I}$ can be determined from Eq. (23) after the velocity of melting at the interface $u_{s\ell}$ is calculated from Eq. (24).

2.6 Liquid-Vapor Phase Change

At the L-V interface, energy balance including evaporation rules derived from the kinetics law is:

$$\rho_\ell h_{\ell v} u_{\ell v} + \sigma\varepsilon (T_{\ell v}^4 - T_\infty^4) = -k_l \frac{\partial T_l}{\partial x} \tag{25}$$

where $h_{\ell v}$ is the latent heat of evaporation, $u_{\ell v}$ is the velocity of the L-V interface, σ is Stefan-Boltzmann constant, ε is emissivity factor, $T_{\ell v}$ is the L-V interfacial temperature and T_∞ is ambient temperature which is set to 300 K in this work.

The vaporization wave model proposed by Bennett [43] for studying the non-equilibrium kinetics of volume vaporization in electrically exploded wires is employed to determine the L-V interfacial velocity. In this model, the velocity of dynamic evaporation is limited by the characteristic speed of sound of the two-phase region of the fluid, according to shock wave theory [66]. The chosen speed is that of the coexistence side of the liquidus, which is the lower volume boundary of the two-phase region. The speed of sound (c_s) in a two-phase region is given by [67]

$$c_s = \frac{dp}{dT} \left(\frac{T}{\rho^2 c_{v,liquid}} \right)^{\frac{1}{2}} \tag{26}$$

where ρ and $c_{v,liquid}$ are density and specific heat of the liquid at temperature T.

To find the liquidus of the two-phase region, a method proposed by Kahl [68] is employed to determine the saturate pressure p under specific temperature T

$$p(T) = \frac{\int_{v_3(T)}^{v_1(T)} p_W \, dv - \varphi(T)}{v_1(T) - v_3(T)} \quad , \quad p_W(v_1) = p_W(v_3) = p(T) \tag{27}$$

where v_1 and v_3 are the specific volume on vaporous and liquidus of the two-phase area

respectively, and

$$\varphi(T) = \int_{T}^{T_c} [c_{v,liquid}(\tau) - c_{v,vapor}(\tau)](1 - \frac{T}{\tau}) d\tau \tag{28}$$

with τ denoting the temperature variable of integration. The pressure p_W in Eq. (28) can be determined by Van der Waal's equation

$$p_W = \frac{R_u T}{v - b} - \frac{a}{v^2} \tag{29}$$

where R_u is universal gas constant, v is the volume of container, and a and b are given by

$$a = 3 p_c v_c^2, \;\; b = v_c / 3 \tag{30}$$

in which p_c is critical pressure, and v_c is critical volume.

By solving Eqs. (27) – (30), the liquidus of the two-phase area can be obtained. The L-V interface velocity is then evaluated according to Eq. (26) on the liquidus. With the known interface velocity $u_{\ell v}$ computed from Eqs. (26) – (30), Eq. (25) can be used to calculate the interfacial temperature T_{lv}. As mentioned in the Chapter of Introduction, the interface velocity predicted by the current method is increased by 2 – 3 order magnitudes in comparison to the results obtained based on the equilibrium assumptions [44,69].

2.7 Phase Explosion

For thermal ablation by ultrashort-pulsed lasers with high laser fluences, phase explosion is the main mechanism for material removal. In numerical analysis for ultrafast laser heating, it is frequently assumed that phase explosion takes place when the liquid temperature is about $0.9T_c$ [53-55, 70 , 71]. In this study, vaporization during the superheating, in addition to melting/re-solidification, is simulated before and after the

phase change occurs. When a volume of the superheated liquid temperature reaches $0.9T_c$, that grid point (including both electrons and lattice subsystems) is removed from the model under the assumption of phase explosion. As long as the material points are removed, the boundary condition is enforced on the new surface. Once phase explosion no longer occurs, vaporization could continue until the temperature significantly drops off and then is followed by re-solidification.

2.8 Boundary and Initial Conditions

As given by Eq. (14), the peak of a laser pulse is assumed to occur at time t = 0. Therefore, the initial conditions of the problem are [42]

$$T_e(x,-2t_p) = T_l(x,-2t_p) = T_i \tag{31}$$

In most previous works, adiabatic boundary conditions were applied to both sides of the metal film. In the current work, the adiabatic condition is applied to the left side which has no laser irradiation. On the right side of the film which receives laser irradiation, the heat loss caused by radiation due to high temperature is considered [42]. Thus,

$$\left.\frac{\partial T_e}{\partial x}\right|_{x=0} = \left.\frac{\partial T_e}{\partial x}\right|_{x=L} = \left.\frac{\partial T_l}{\partial x}\right|_{x=L} = 0 \tag{32}$$

$$\left.q_R^{"}\right|_{x=0} = \sigma\varepsilon(T_{sur}^4 - T_\infty^4) \tag{33}$$

where σ is Stefan-Boltzmann constant and ε is emissivity factor. Before evaporation takes place, T_{sur} is the surface lattice temperature at $x = L$. After evaporation begins, T_{sur} is the L-V interface temperature.

CHAPTER 3: NUMERICAL ALGORITHM

The finite difference method is employed to solve the problems including electron and lattice temperature change, melting/solidification and vaporization process, and phase explosion. In each time step, an iterative procedure is applied to deal with the non-linear relationships in electron energy equation, lattice energy equation, and the S-L interface and L-V interface equations. If the classical TTM is adopted, the electron energy Eq. (1) is discretized and solved first using tri-diagonal matrix method algorithm, after that the lattice energy Eq. (2) is solved using the same method. If the semi-classical TTM is applied, the electron momentum Eq. (3) is discretized and solved first by using a central difference method to obtain electron drifting velocity, then the electron energy Eq. (4) is solved using the tri-diagonal matrix method with known electron velocity, after that the lattice energy Eq. (5) is solved using the same matrix method.

At the first iteration in each time step, all the thermophysical properties involved in the equations are updated based on the temperature of the previous time step while the optical properties are only updated during the lasing time. After the electron and lattice temperature fields are obtained, the velocity and temperature of S-L interface, if melting or solidification occurs, will be calculated by using the method mentioned in Chapter 2.

3.1 Solid-Liquid Interface Tracking Method

Many numerical models for melting and solidification in materials have been developed. The numerical models can be divided in two groups [72]: deforming grid

schemes (or strong numerical solutions) and fixed grid scheme (or weak numerical solutions). Deforming grid schemes transform solid and liquid phases into fixed regions by using a coordinate transformation technique. In this method, the governing equations and boundary conditions are complicated due to the transformation. The disadvantage of deforming grid schemes is that it requires significant amount of computational time. On the contrary, the fixed grid schemes use one set of governing equations for the entire computational domain including both solid and liquid phases. The S-L interface is later determined from the resulting temperature distribution. This simplicity makes the computation much faster than the deforming grid schemes, while still providing reasonably accurate results [73]. The fixed grid schemes further includes two main methods: enthalpy method and the equivalent heat capacity method. The enthalpy method [74] can solve heat transfer in mushy zone but has difficulty with temperature oscillation, while the equivalent heat capacity method [75,76] requires large enough temperature range in mushy zone to obtain a converged solution. Cao and Faghri [77] combined the advantages of both enthalpy and equivalent heat capacity methods and proposed a temperature transforming model. Recently, Zhang and Chen [13] proposed another interfacial tracking method to model the rapid melting and re-solidification process of a free standing metal film irradiated by ultrashort laser pulses. In their method, the implicit finite difference equations are obtained by integrating Eqs. (1) and (2) in each control volume and time step. This algorithm is employed in this work and will be described below.

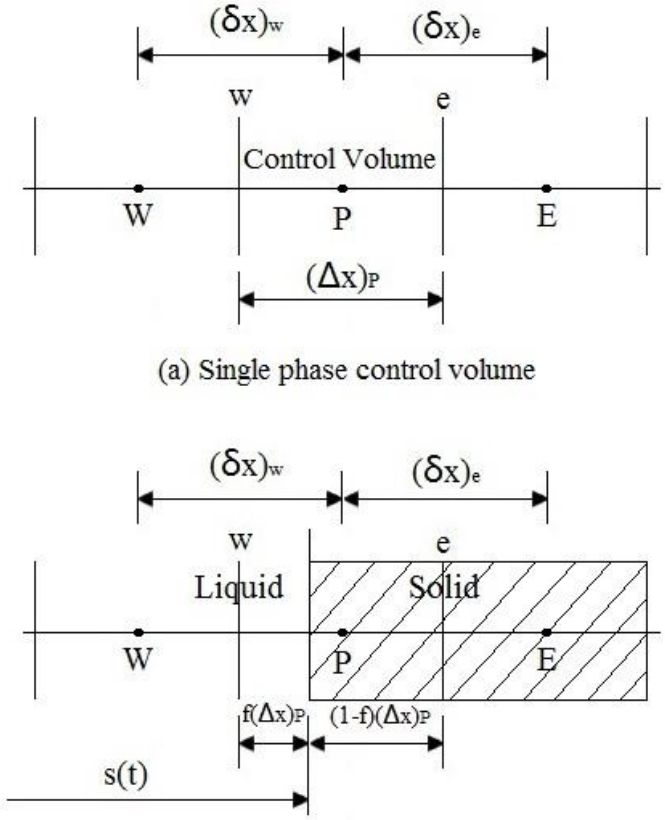

Figure 3.1 Grid system [13]

The electron temperature can be obtained by

$$a_{e,P}T_{e,P} = a_{e,W}T_{e,W} + a_{e,E}T_{e,E} + b_e \tag{34}$$

where $T_{e,P}, T_{e,W}, T_{e,E}$ are electron temperatures at grid *P*, *W*, *E* at the current time step (see Fig. 3.1), respectively. The coefficients in Eq. (34) are as follows:

$$a_{e,W} = \frac{k_{e,w}}{(\delta x)_w} \tag{35}$$

$$a_{e,E} = \frac{k_{e,e}}{(\delta x)_e} \tag{36}$$

$$a_{e,P} = a_{e,P}^0 + a_{e,W} + a_{e,P} + G_p(\Delta x)_P \tag{37}$$

$$a_{e,P}^0 = \frac{C_{e,P}(\Delta x)_P}{\Delta t} \tag{38}$$

$$b_e = a_{e,P}^0 T_{e,P}^0 + (G_P T_{l,P} + S_P)(\Delta x)_P \tag{39}$$

where $k_{e,w}$ and $k_{e,e}$ are electron conductivities at the faces of control volume *w* and *e*, and they are obtained by harmonically averaging the thermal conductivities at the two control volume; $T_{e,P}^0$ is the electron temperature at grid *P* for the previous time step; $T_{l,P}$ is the lattice temperature at grid *P* for the current time step; and S_P is the laser density at grid *P*.

For a control volume that contains one phase only, the lattice temperature can be obtained by integrating Eq. (2) in the control volume *P*, i.e.,

$$a_{l,P} T_{l,P} = a_{l,W} T_{l,W} + a_{l,E} T_{l,E} + b_l \tag{40}$$

where $T_{l,P}, T_{l,W}, T_{l,E}$ are lattice temperatures at grid *P*, *W*, *E* at the current time step, respectively. The coefficients in Eq. (40) are as follows:

$$a_{l,W} = \frac{k_{l,w}}{(\delta x)_w} \tag{41}$$

$$a_{l,E} = \frac{k_{l,e}}{(\delta x)_e} \tag{42}$$

$$a_{l,P} = a_{l,P}^0 + a_{l,W} + a_{l,P} + G_p(\Delta x)_P \tag{43}$$

$$a_{l,P}^0 = \frac{C_{l,P}(\Delta x)_P}{\Delta t} \tag{44}$$

$$b_l = a_{l,P}^0 T_{l,P}^0 + G_P T_{e,P}(\Delta x)_P \tag{45}$$

where the lattice conductivities at the faces of the control volume are obtained by harmonically averaging the thermal conductivities at two control volumes, and $T_{l,P}^{0}$ is the lattice temperature at grid point *P* from the previous time step.

For the control volume that contains an S-L interface, the lattice temperature $T_{l,P}$ is numerically set as interfacial temperature $T_{l,I}$ by letting the values of $a_{l,P}$ and b_l in Eq. (40) to be

$$a_{l,P} = 10^{20} \quad \text{and} \quad b_l = T_{l,I} \times 10^{20} \tag{46}$$

This treatment will yield an accurate result when the S-L interface is exactly at grid point *P*. When the interfacial location is not at grid point *P*, a modified thermal conductivity, $\hat{k}_{l,w}$, at the face of the control volume *w* is introduced by equating the actual heat flux across the face of the control volume *w*, based on the position and temperature of the S-L interface, to the heat flux at face *w* based on the position and temperature of the main grid point *P* , i.e.,

$$\frac{k_{l,w}(T_{l,W} - T_{l,I})}{(\delta x)_w - (0.5 - f_P)(\Delta x)_P} = \frac{\hat{k}_{l,w}(T_{l,W} - T_{l,P})}{(\delta x)_w} \tag{47}$$

By considering $T_{l,P} = T_{l,I}$, Eq.(47) becomes

$$\hat{k}_{l,w} = \frac{(\delta x)_w}{(\delta x)_w - (0.5 - f_P)(\Delta x)_P} k_{l,w} \tag{48}$$

Similarly, a modified thermal conductivity at face *e* of the control volume can be obtained as:

$$\hat{k}_{e,w} = \frac{(\delta x)_e}{(\delta x)_e + (0.5 - f_P)(\Delta x)_P} k_{l,e} \tag{49}$$

The modified thermal conductivities defined by Eqs. (48) and (49) are used to obtain the coefficients for grid points *W* and *E*, which allows the temperature at the main grid point *P* to be used in the computation, regardless of the location of the interface within the control volume. To determine the interfacial location and the interfacial temperature, the energy balance at the interface, Eq. (23), and the nucleation dynamics, Eq. (24), are employed. The lattice energy equation for the control volume that contains the S-L interface can be written in the enthalpy form

$$\frac{\partial H_l}{\partial t} = \frac{\partial}{\partial x}(k_l \frac{\partial T_l}{\partial x}) + G(T_e - T_l) \tag{50}$$

The volumetric enthalpy can be expressed as

$$H_l = \int_0^{T_{l,I}} C_{l,s}(T_l) dT_l + f\rho_\ell h_m \tag{51}$$

where the first term is the enthalpy of the solid phase at the interfacial temperature, and the second term is the latent heat due to partial melting. Substituting Eq. (51) into Eq. (50), one obtains

$$C_{l,s}(T_{l,I}) \frac{\partial T_{l,I}}{\partial t} + \rho_\ell h_m \frac{\partial f}{\partial t} = \frac{\partial}{\partial x}(k_l \frac{\partial T_l}{\partial x}) + G(T_e - T_l) \tag{52}$$

which is applicable in the control volume that contains the S-L interface. The liquid fraction *f* is related to the location of the S-L interface by

$$\frac{\partial f}{\partial t} = \frac{1}{(\Delta x)_P} \frac{ds}{dt} = \frac{u_s}{(\Delta x)_P} \tag{53}$$

Substituting Eq. (53) into Eq. (52) and integrating the resulting equation in the control volume that contains the S-L interface, the interfacial velocity can be obtained as

$$u_s = \frac{1}{\rho_\ell h_m}\left[\frac{k_{l,w}(T_{l,W} - T_{l,I})}{(\delta x)_w - (0.5 - f_P)(\Delta x)_P} - \frac{k_{l,e}(T_{l,I} - T_{l,E})}{(\delta x)_e + (0.5 - f_P)(\Delta x)_P}\right.$$
$$\left. + G_P(T_{e,P} - T_{l,P})(\Delta x)_P - C_{l,s}(T_{l,I})(T_{l,I} - T_{l,I}^0)\frac{(\Delta x)_P}{\Delta t}\right] \tag{54}$$

where $T_{l,I}^0$ is the S-L interfacial temperature at the previous time step. The third and fourth terms in the bracket at the right side of Eq. (54) represent the effects of the electron-lattice interaction and the change of the interfacial temperature due to S-L phase change. Eq. (54) can be rewritten in a more compact form by adopting Eqs. (48) and (49), i.e.,

$$u_s = \frac{1}{\rho_\ell h_m}\left[\frac{\hat{k}_{l,w}(T_{l,W} - T_{l,P})}{(\delta x)_w - (0.5 - f_P)(\Delta x)_P} - \frac{\hat{k}_{l,e}(T_{l,P} - T_{l,E})}{(\delta x)_e + (0.5 - f_P)(\Delta x)_P}\right.$$
$$\left. + G_P(T_{e,P} - T_{l,P})(\Delta x)_P - C_{l,s}(T_{l,I})(T_{l,I} - T_{l,I}^0)\frac{(\Delta x)_P}{\Delta t}\right] \tag{55}$$

which will be used together with Eq. (14) to determine the S-L phase interfacial velocity and temperature. The interfacial location is then determined using

$$s = s^0 + u_s \Delta t \tag{56}$$

and the liquid fraction in the control volume that contain the interface is

$$f = \frac{s - x_P - (\Delta x)_P / 2}{(\Delta x)_P} \tag{57}$$

3.2 Liquid-Vapor Interface Tracking Method

If vaporization occurs, the following iterative procedure will be employed to track the L-V interface:

(1) Assume an interface velocity, $u_{\ell v}^*$, using the velocity of the previous time step, $u_{\ell v}^0$, as initial value.

(2) Determine the new interface location $s^*_{\ell v}$ according to $s^*_{\ell v} = s^0 + u^*_{\ell v}\Delta t$.

(3) Use Newton's method to solve the energy balance equation at the L-V interface, Eq. (25), to obtain the interface temperature $T_{\ell v}$.

(4) Obtain the new interface velocity $u^{**}_{\ell v}$ from Eq. (26). Under-relaxation was used in this step to avoid divergence in the iterative solution of the L-V interface temperature and location:

$$u^{***}_{\ell v} = u^*_{\ell v} + \alpha_{\ell v}(u^{**}_{\ell v} - u^*_{\ell v}) \tag{58}$$

(5) Go to step 2 and use $u^{***}_{\ell v}$ as the new interface velocity.

Steps 2-5 are repeated, which is called inner iteration, until the difference between the interfacial velocities obtained from two successive iterations is less than 10^{-5} m/s. After that, the properties in the electron and lattice energy equations will be re-evaluated and Eqs. (1) and (2) (for classical TTM) or Eqs. (3), (4) and (5) (for semi-classical TTM) will be solved again. The above procedures will be repeated, which is called outer iteration, until the maximum difference between the lattice temperatures obtained from two successive iterative steps is less than 10^{-5} K.

CHAPTER 4: TEMPERATURE-DEPENDENT OPTICAL PROPERTIES

4.1 Problem Statement

To study the impact of dynamic reflectivity and absorption coefficient on prediction of thermal response of metal films caused by ultrafast laser heating, a free standing copper film with thickness of 1-μm is assume to be irradiated on the front surface by a Gaussian laser pulse of t_p = 150 fs, λ = 800 nm (wavelength) (see Fig. 2.1), and J_o = 1.5 J/cm^2. The initial temperature of copper film is set to be 300 K. The thermophysical and optical properties of copper is given in Table 1. The parameters for the critical point model are given in Table 2. A total of 2,500 control volumes are employed in the numerical simulation. In this part of study, only the classical TTM is considered.

4.2 Results and Discussion

Figures 4.1 and 4.2 compare R and α at RT described by different models with experimental data [78] for the range of λ = 200 – 1000 nm. It can be seen from Figs. 4.1 and 4.2 that the proposed critical point model with three Lorentzian terms computes much more satisfying results, compared to the Drude model [64] and Rakic et al. [60].

Figures 4.3 shows the calculated reflectivity R as a function of temperature ($T = T_l = T_e$) for copper. The reflectivity R decreases with temperature, especially for longer wavelengths. The monotonic trend is not always found for α as shown in Fig. 4.4. During the ultrafast laser irradiation, the values of R and α are determined by electron and

Table 1 Thermophysical properties of copper [56]

Properties	Solid (*s*)	Liquid (*l*)
Specific heat, c_p (J/kg·K)	$313.75+0.324\times T_l-2.687\times10^{-4}\times T_l^2+1.2568\times10^{-7}\times T_l^3$	510.082
Bulk conductivity, k_{eq} (W/m·K)	$407.88-0.0272\times T_l-2.658\times10^{-5}\times T_l^2-3.0\times10^{-9}\times T_l^3$	$62.47+0.123\times T_l-4.02\times10^{-5}\times T_l^2+4.855\times10^{-9}\times T_l^3$
Latent heat of fusion, h_m (kJ/kg)	206.8	
Molar weight, M (kg/kmol)	63.546	
Boiling temperature, T_b (K)	2835	
Melting temperature, T_m (K)	1357	
R at RT for 800 nm	0.958	
α at RT for 800 nm (μm^{-1})	78.80	
Density, ρ (kg/m^3)	8.94×10^3	8.02×10^3

Table 2 Parameters for the critical point model fitted for copper

ε_∞	ω_D (rad s^{-1})	B_1	Φ_1	Ω_1 (rad s^{-1})	Γ_1 (rad s^{-1})	B_2
2.494	1.33E16	0.849	-8.052	3.23E15	5.20E14	23.29
Φ_2	Ω_2 (rad s^{-1})	Γ_2 (rad s^{-1})	B_3	Φ_3	Ω_3 (rad s^{-1})	Γ_3 (rad s^{-1})
-7.75	2.49E14	1.27E15	0.854	-5.618	8.18E15	2.19E15

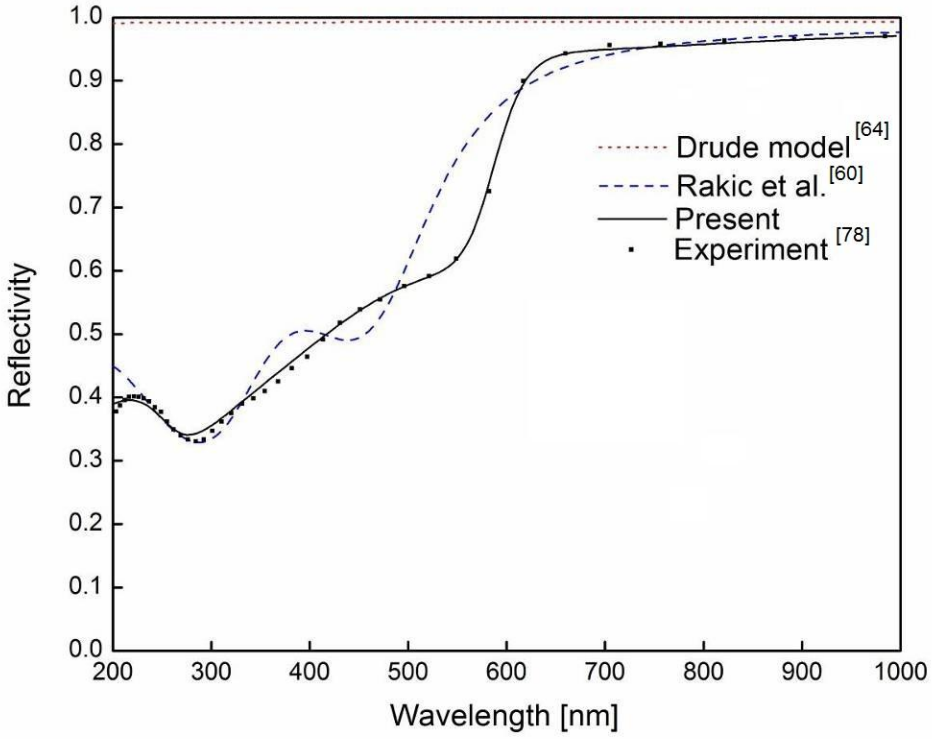

Figure 4.1 Reflectivity versus wavelength at RT calculated by different models

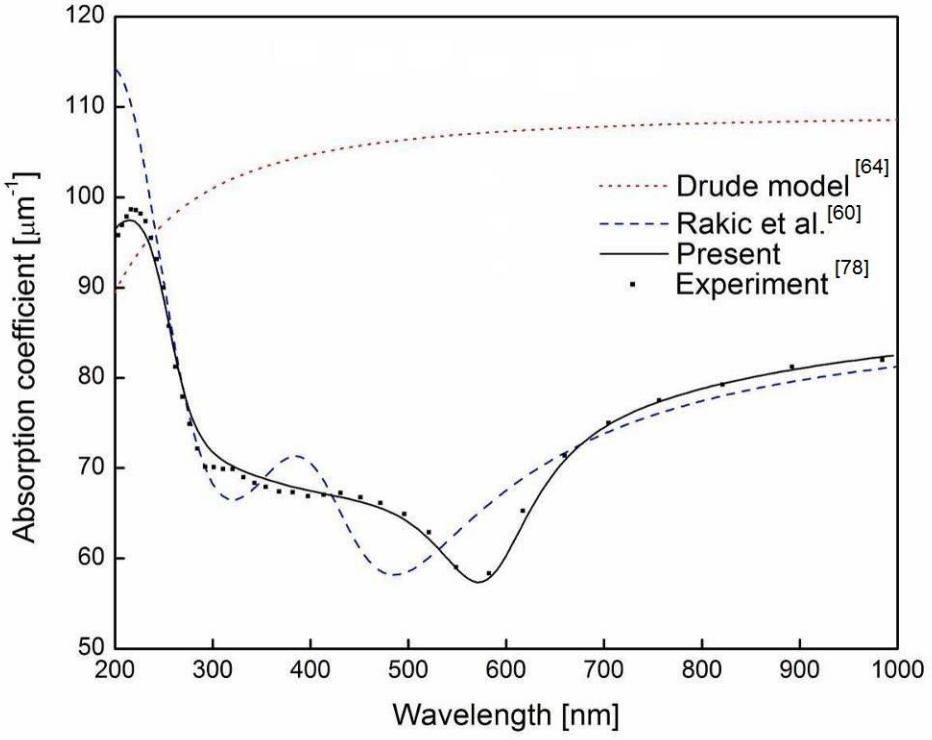

Figure 4.2 Absorption coefficient versus wavelength at RT calculated by different models

lattice temperatures. A considerable change in surface reflectivity and in the absorption coefficient could drastically alter transient electron and lattice temperatures, both in magnitude and spatial distribution. This suggests that the constant reflectivity and absorption coefficient at RT that have been widely employed in classical TTM are only adequate for very low laser fluencies. For a solid target undergoing S-L and/or L-V phase changes, temperature-dependent reflectivity and absorption coefficient should be employed in the modeling.

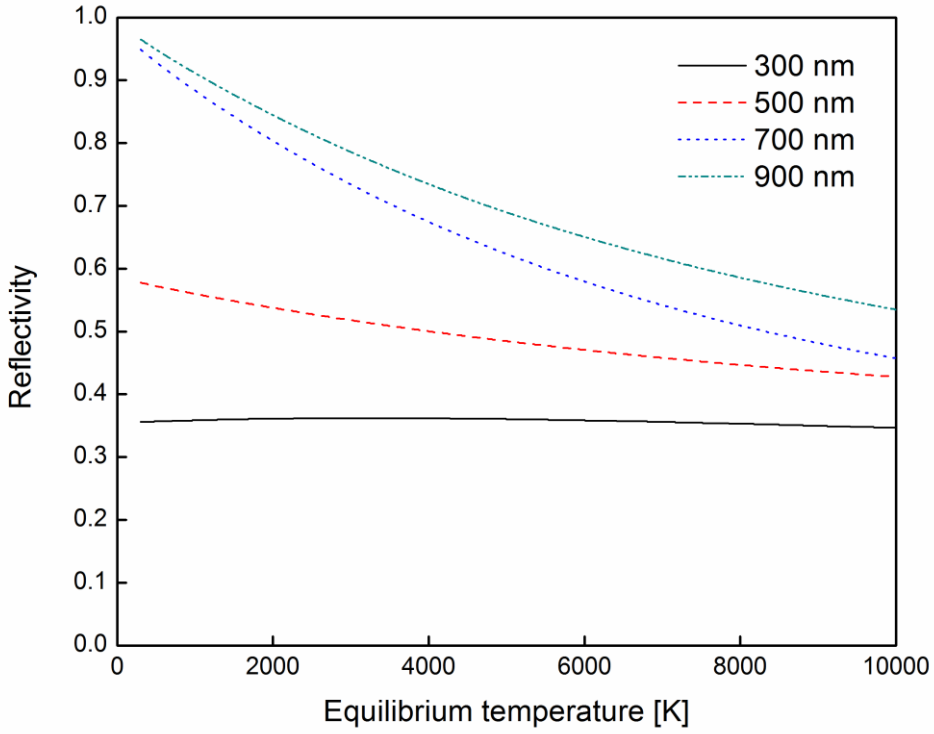

Figure 4.3 Reflectivity as a function of equilibrium temperature for different wavelengths

A value of 0.12×10^{6} $K^{-2}s^{-1}$ is chosen for A_e to fit the experimental data for the 50-fs pulses [36], and then is used for all the simulations. Figure 4.5 shows the average absorption for four laser pulse lengths, 50 fs, 150 fs, 500 fs and 1 ps, where the average

absorption of the target is calculated by [35]

$$A = \frac{\int_{-2t_p}^{2t_p} dt \int_0^L S(x,t)dx}{\int_{-2_p}^{2t_p} I(t)dt} \tag{59}$$

with $I(t)$ being the laser intensity right before the laser beam reaches the target

$$I(t) = 0.94 \frac{J_o}{t_p} \exp\left[-2.77 \left(\frac{t}{t_p} \right)^2 \right] \tag{60}$$

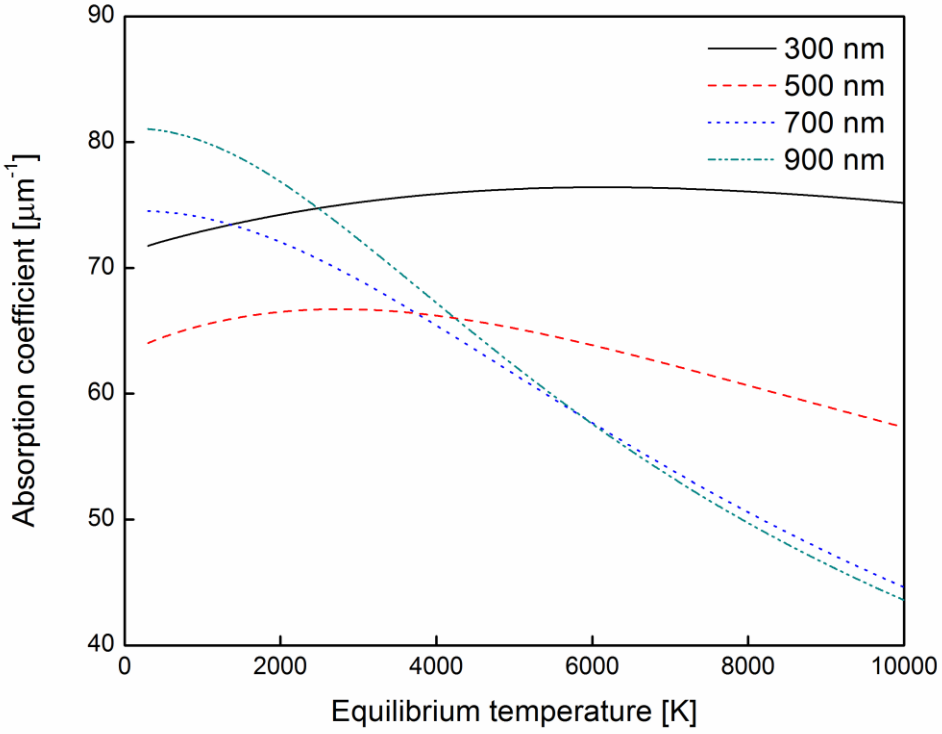

Figure 4.4 Absorption coefficient as a function of equilibrium temperature for different wavelengths

As shown in Fig. 4.5, the present approach correlates well the average absorption with the experimental data [36], compared to the other theoretical result [36]. It is also seen that the longer the laser pulse, the higher the surface absorption. This is attributed to the fact that for the same peak laser intensity I_o, a longer pulse contains more energy.

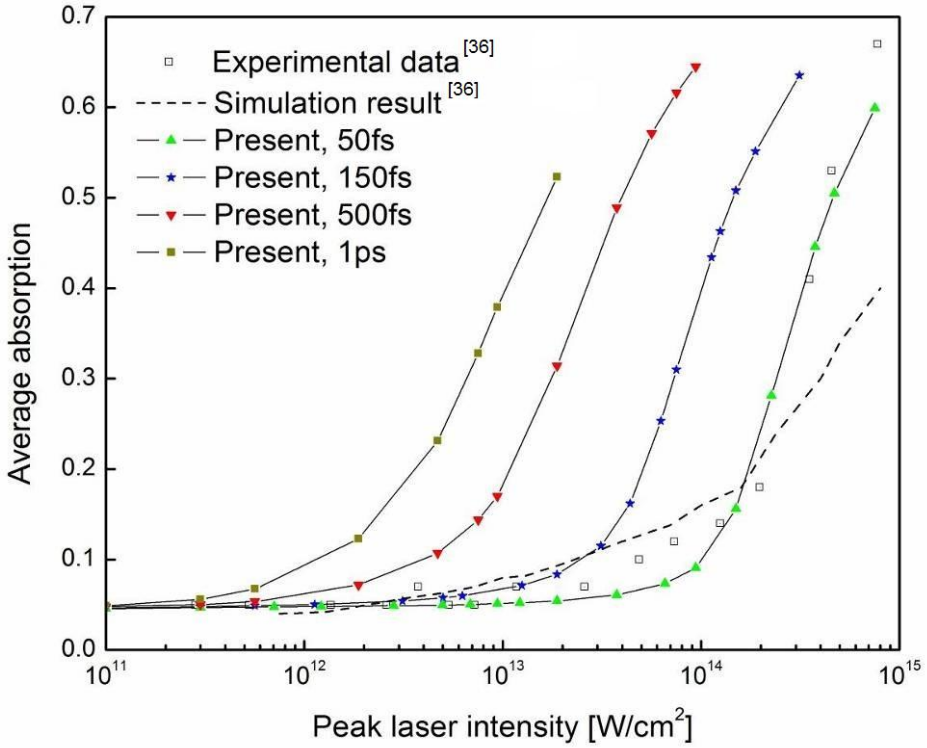

Figure 4.5 Experimental and simulation results of average absorption for different laser pulses with λ = 800 nm

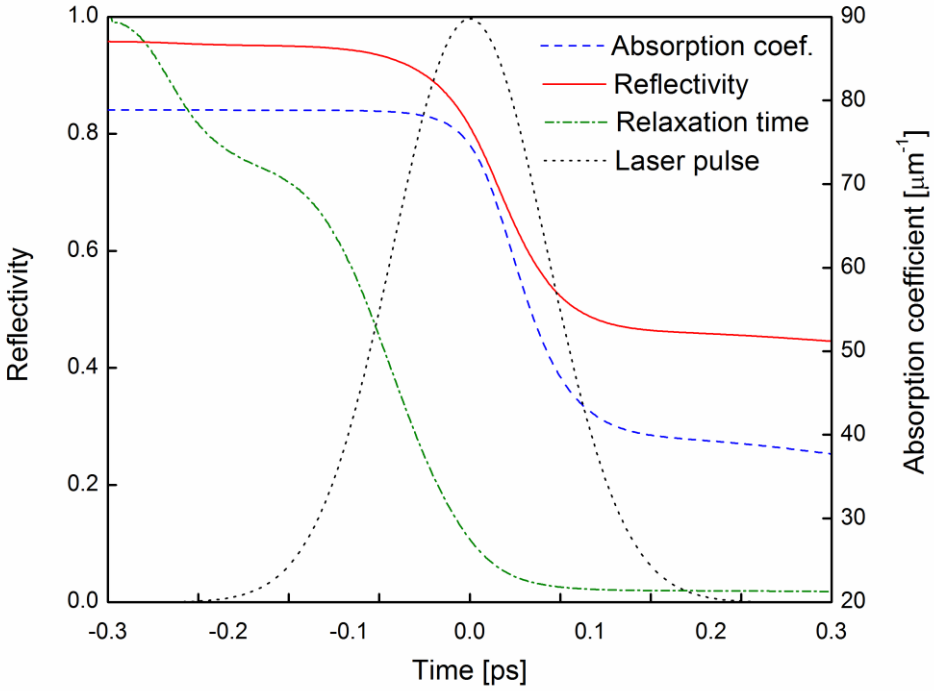

Figure 4.6 Variations of reflectivity and absorption coefficient during laser irradiation

Apparently, the difference of the absorption among the four laser pulses is not so pronounced for low laser intensities, i.e., $<10^{12}$ W/cm^2. The reason is that for those intensities the induced electron and lattice temperature would not be high enough to significantly change R and α. For example, the smallest electron relaxation time is 5.8 fs (at T_e = 4,644 K and T_l = 400 K) for the 150-fs pulse at $I_o = 1.0\times10^{12}$ W/cm^2 (see Figs. 4.3 and 4.4).

Figure 4.6 shows the transient variations of surface reflectivity $R(0,t)$ and absorption coefficient $\alpha(0,t)$ during the laser irradiation. For convenience, the normalized temporal Gaussian profile of the laser pulse and the normalized electron relaxation time are also presented. In this simulation, the pulse length is 150 fs and the peak laser intensity (I_o) is 6.0×10^{13} W/cm^2. As expected, the electron relaxation time decreases due to the rises of electron and lattice temperature. As a result, both R and α decrease. The decrease in R makes the target absorb more laser energy while the decrease in α alters the distribution of laser heat density inside the target.

Figure 4.7 plots the spatial profiles of the laser heat density $S(x,t)$ at t = 0.1 ps for four different laser intensities I_o. For low laser intensity the laser heat density basically follows exponential decay characterized by Beer's law since α remains almost the same. Nonetheless, the exponential decay no longer exists for higher laser intensities, except in the deeper part where α is not significantly altered. For example, for the case of 8.0×10^{13} W/cm^2 shown in Fig. 4.7, the laser heat density decays much slower with a plateau present in the region 10 nm < x < 25 nm.

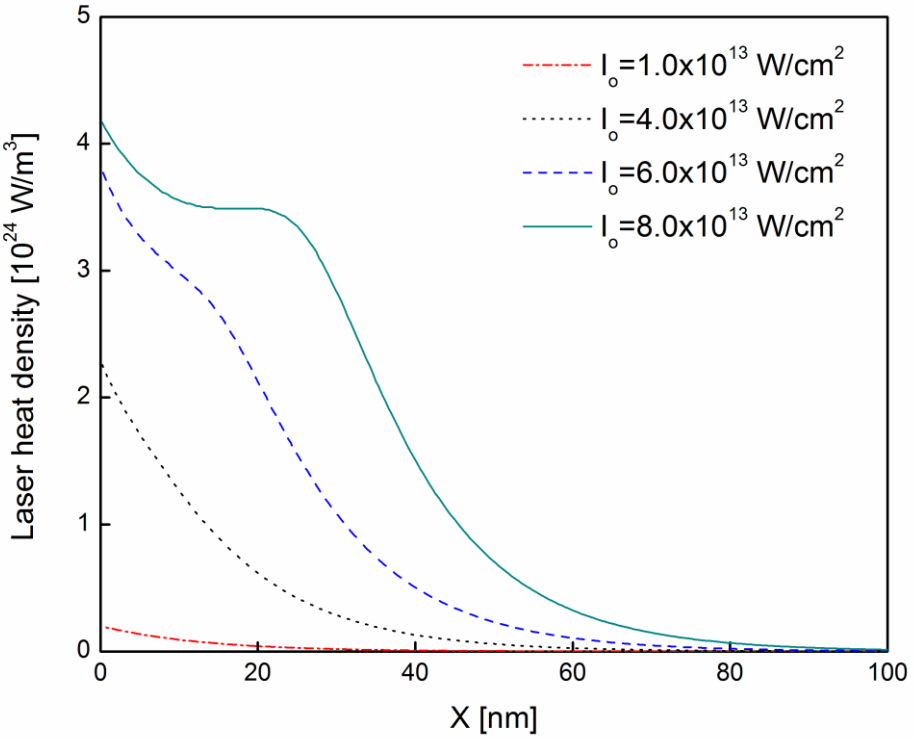

Figure 4.7 Distributions of volumetric laser heat along film thickness at different times

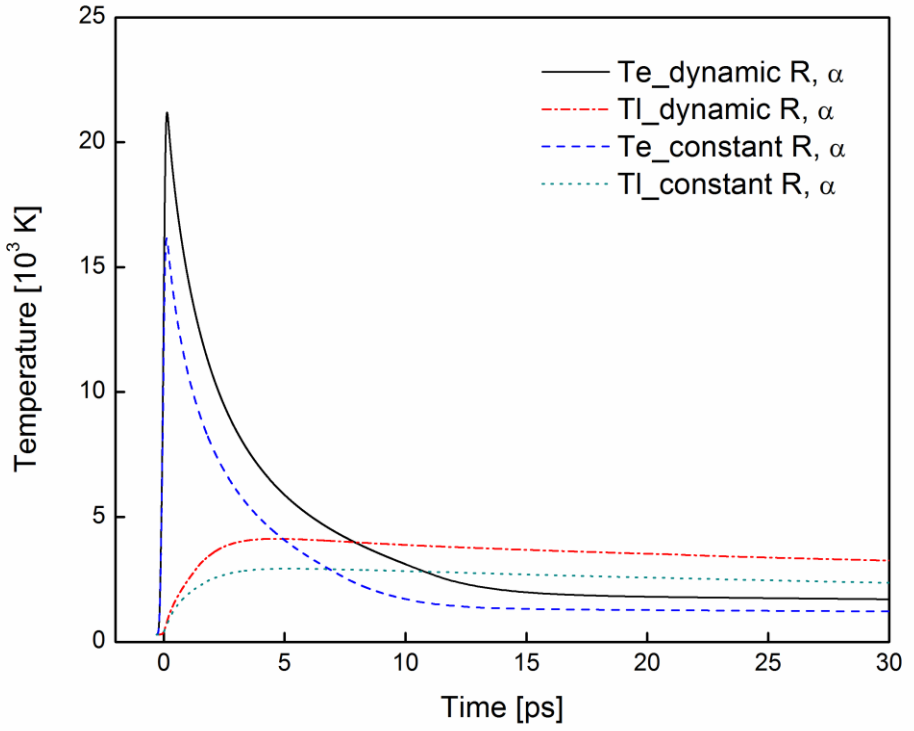

Figure 4.8 Time histories of electron and lattice temperature at the irradiated surface

Figure 4.8 shows the time evolutions of electron and lattice temperature at the front surface of the copper film heated by the 150-fs laser pulse with J_o = 1.5 J/cm^2. Both T_e and T_l predicted with dynamic R and α are higher than those predicted with constant R and α at RT. The simulated peak T_e and T_l are 21,187 K and 4,132 K versus 16,158 K and 2,936 K, respectively. It can be seen in Fig. 4.8 that T_e becomes equal to T_l at about t = 7.9 ps. After that, T_e is even lower than T_l. The difference keeps increasing until t = 17.4 ps and then decreasing until the thermal equilibrium established, at about t = 3 ns. The non-equilibrium between T_e and T_l during this stage is governed by two competing mechanisms: diffusion of electron thermal energy into the deeper part of electrons and energy transfer from the lattice. Obviously, the former is predominating in this process. The distinction between T_e and T_l should depend on laser fluence. The high the fluence is, the larger the difference is. Also, the difference between the two temperatures would be smaller inside the material. The farther the distance from the irradiated surface, the smaller the difference.

4.3 Conclusion

It was demonstrated here that the critical point model with three Lorentzian terms for interband transition can accurately describe optical reflectivity and absorption coefficient for copper in the range of wavelength 200 – 1000 nm at room temperature. After validated with the existing experimental data at RT, it was incorporated into a classical two-temperature model to study ultrafast laser-material interaction. The dynamic changes of optical properties R and α during laser irradiation, distributions of laser heat density,

and electron and lattice temperature of a copper film irradiated by ultrashort-pulsed lasers were investigated. It was shown that this optical model can provide satisfactory results of average absorption compared to experimental results. It was also found that for the same peak laser intensity the longer the laser pulse, the higher the energy absorption. At high laser fluences both the optical properties R and α could drastically decrease during laser irradiation, leading to different laser energy deposition, both in magnitude and spatial distribution, in the heated material. Further investigation of the impact of dynamic optical properties on phase changes and laser material ablation will be discussed later.

CHAPTER 5: ENERGY TRANSPORT AND PHASE CHANGES IN METAL FILMS

5.1 Problem Statement

In this chapter, the energy transport and phase changes are investigated using the classical and semi-classical TTM with temperature-dependent optical and thermophysical properties described above. The initial temperature T_i is still set to be 300 K. In this study, a gold film with thickness of 1-μm is adopted to be the target medium (refer to Fig. 2.1). Single laser pulses with durations of 100 fs –10 ps and laser fluences of 0.15 – 0.68 J/cm^2 are considered. The wavelengths of all the laser pulses are 700 nm. The thermophysical properties of gold and the parameter used for calculating surface reflectivity and absorption coefficient are described in Chapter 2. In this chapter, the extended Drude model is employed to characterize the optical properties of gold at different temperatures.

5.2 Results and Discussion

Figure 5.1 plots the volumetric laser heat source distribution at different time instants in the front layer (x = 0 – 100 nm) of a gold film irradiated by a 100-fs laser pulse of J_o = 0.15 J/cm^2, obtained from the semi-classical TTM with dynamic optical properties. The deposited laser energy density at the front surface reaches its peak value 3.187×10^{17} W/cm^3 at t = 12.8 fs, about 9 times the peak value 0.35×10^{17} W/cm^3 that is computed with the constant R and α at RT. It is noted that the minimum reflectivity occurs at about t = 97.6 fs. The different times of the peak laser energy density and of the minimum

reflectivity are because the absorbed laser energy is proportional to [1-$R(0,t)$]$\alpha(0,t)$. It appears in Fig. 5.1 that those spatial distributions of the volumetric laser heat source after t = 0 differ significantly from exponential decay characterized by Beer's law with constant R and α.

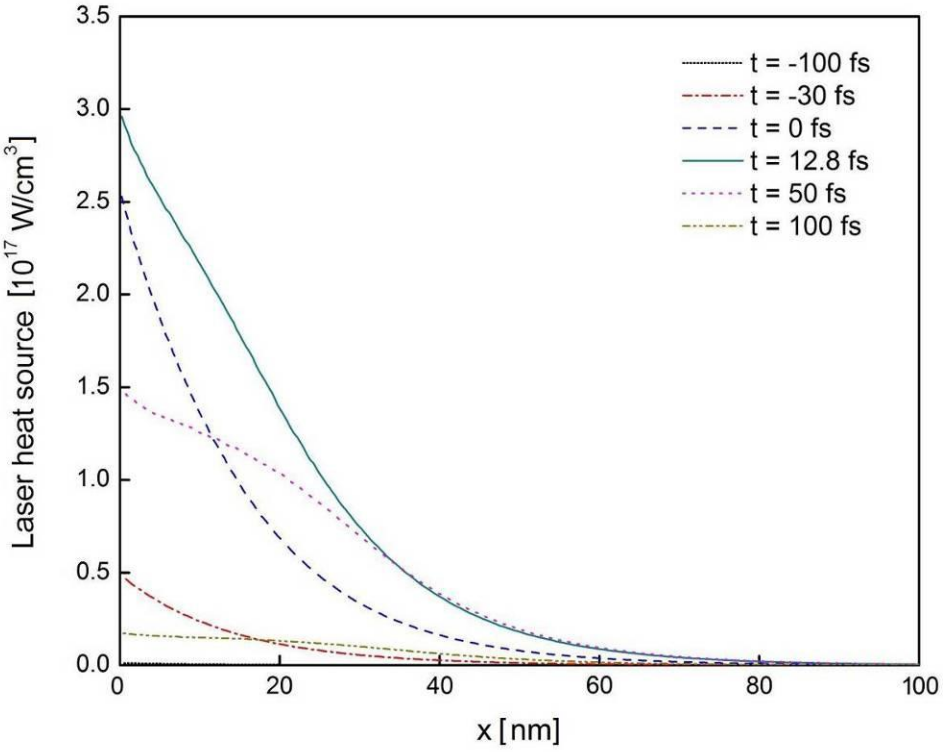

Figure 5.1 Distributions of volumetric laser heat source in the depth 0-100 nm of the gold film at different times (t_p = 100 fs, J_o = 0.15 J/cm^2)

The electron and lattice temperature at the front surface are presented in Fig. 5.2 against time. For comparison, the results simulated by the classical TTM with dynamic optical properties and the semi-classical TTM with constant R and α at RT are also shown in the figure. It can be seen from Fig. 5.2 that the semi-classical TTM results in lower electron and lattice temperature than the classical TTM. Although the peak electron

temperatures computed by the two models are close, the peak lattice temperatures are different by 162 K. The lower electron temperature particularly after the peak electron temperature simulated by the semi-classical TTM is attributed to part of energy converted to kinetic energy for electron drifting. As shown in Fig. 5.2, a TTM with constant R and α at RT considerably underestimates the electron and lattice temperature, compared to those with dynamic R and α.

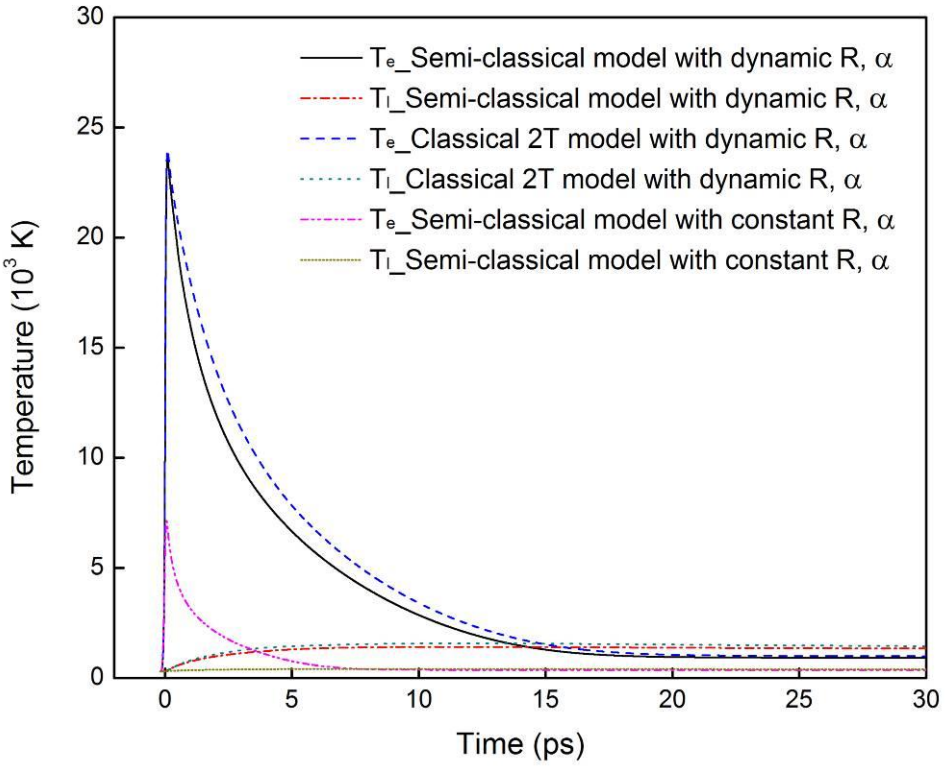

Figure 5.2 Time evolution of electron and lattice temperature at the front surface predicted by different models (t_p = 100 fs, J_o = 0.15 J/cm^2)

The distributions of lattice temperature in the thickness direction are plotted in Fig. 5.3 for different time instants, simulated with the semi-classical TTM. Particular attention is paid to the small regions near the front surface for the time instants t = 10 ps and 25 ps.

The peak temperatures are greater than the normal melting point T_m (1,336 K) and occur somewhere inside the film. Both the humps with $T_l > T_m$ are the superheated solid region. At t = 50 ps, the film is experiencing undercooling from the solidification process, indicated by the localized minimum temperature in a small valley near the front surface and by the negative interfacial velocity (moving back to the irradiated surface) shown in Fig. 5.4. After the phase change is complete at about t = 75 ps, only pure heat conduction takes place as shown by the temperature distributions at t = 100 ps and 250 ps.

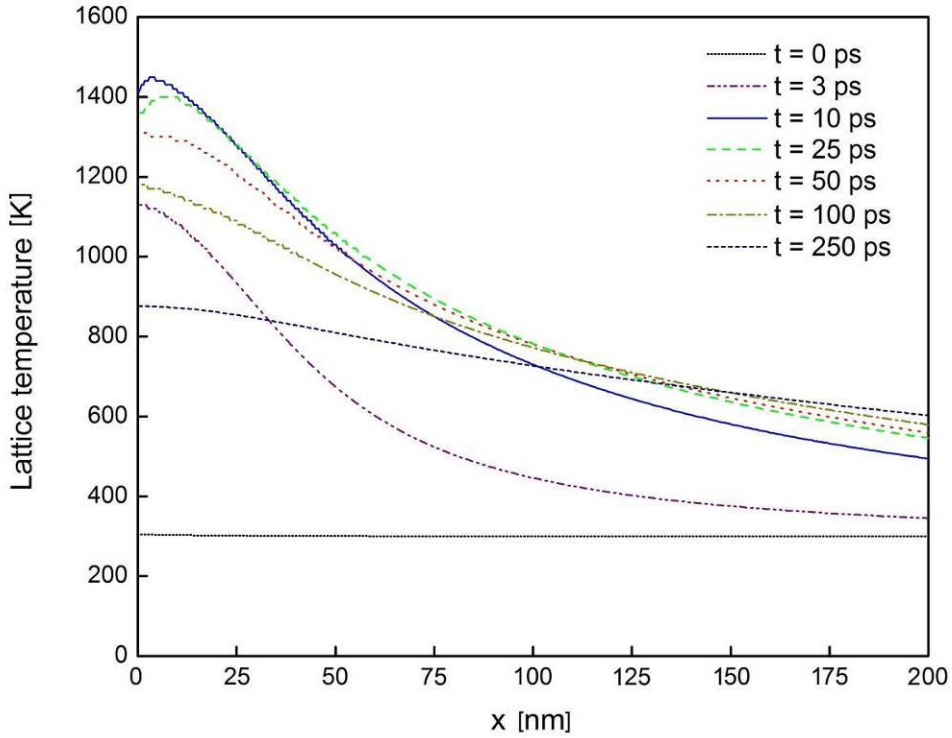

Figure 5.3 Distribution of lattice temperature in the depth 0-200 nm of the gold film at different times (t_p = 100 fs, J_o = 0.15 J/cm^2)

The difference of the S-L interfacial velocity and location obtained from the classical and semi-classical TTM can be seen in Fig. 5.4. In either model, melting takes place from

the surface exposed to the laser and continues until the maximum melting depth is reached. After that, solidification (negative interfacial velocity) starts and the S-L interface then moves back to the laser exposure side. The peak interfacial velocity simulated by the two models are 192.3 m/s versus 76.7 m/s, the total time of phase change 153.6 ps versus 75.0 ps, and the maximum melting depth 5.06 nm versus 1.13 nm. No vaporization is simulated by both models in this case.

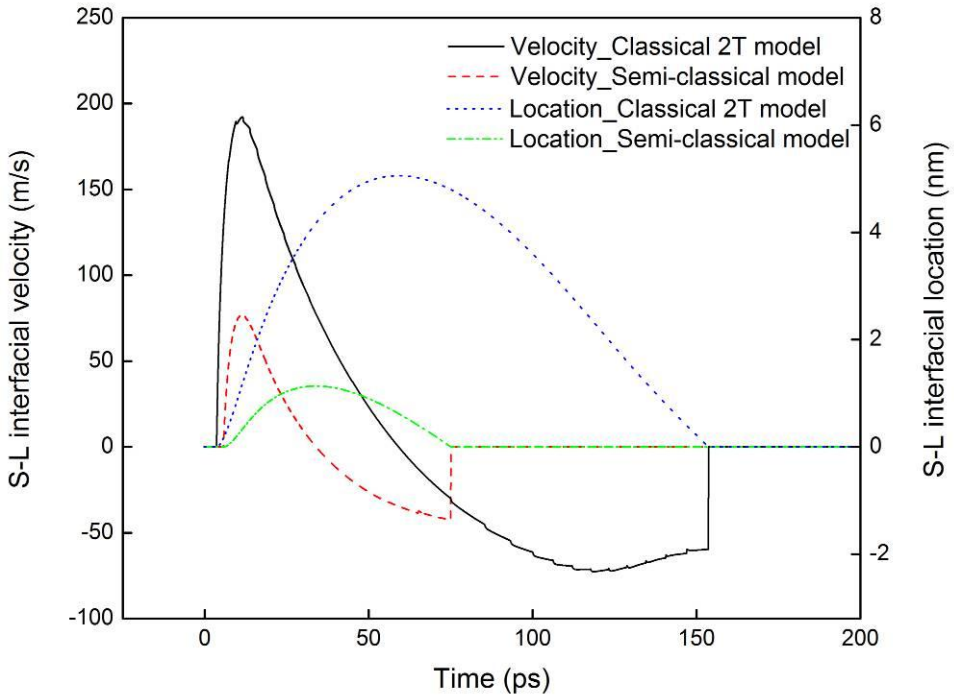

Figure 5.4 Solid-liquid interfacial velocity and location predicted by the semi-classical and classical TTM (t_p = 100 fs, J_o = 0.15 J/cm^2)

Figure 5.5 plots the volumetric laser heat source distribution at different times in the front part (0 – 100 nm) of the film irradiated by the 100-fs laser pulse at J_o = 0.3 J/cm^2. At this level of laser power, the laser energy density at the front surface can be as high as 6.169×10^{17} W/cm^3 occurring at t = -16.8 fs, while it is only 0.71×10^{17} W/cm^3 computed

with the constant R and α at RT. Comparing to the previous case of 0.15 J/cm^2, the peak laser energy density here becomes 1.94 times and occurs at an earlier time (-16.8 fs versus 12.8 fs). As shown in Fig. 5.5, the non-exponential spatial distributions are more manifest in this higher fluence case. At t = 30 fs and 50 fs, another maximum laser energy density is present around x = 40 nm, in addition to the one at the front surface.

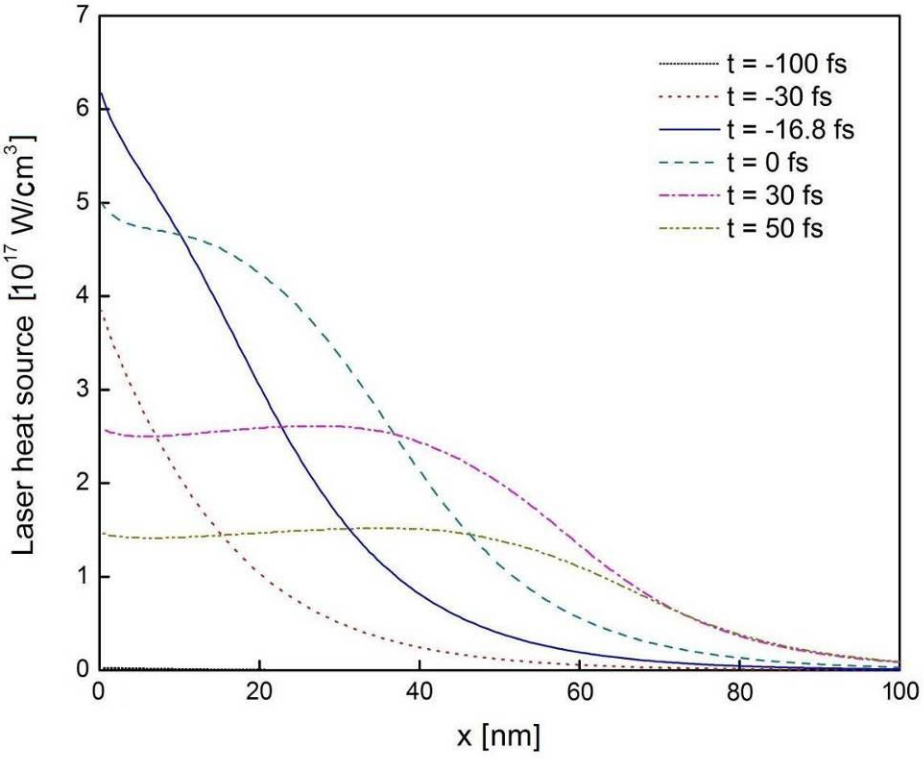

Figure 5.5 Distributions of volumetric laser heat source in the depth 0-100 nm of the gold film at different times (t_p = 100 fs, J_o = 0.3 J/cm^2)

The evolutions of electron and lattice temperature at the irradiated surface are shown in Fig. 5.6. As the laser fluence is doubled from 0.15 J/cm^2, higher electric temperatures are expected as shown in Figs. 5.2 and 5.6. As a result, the difference of the peak lattice temperatures is quite remarkable, 586 K in Fig. 5.6 compared to 162 K in Fig. 5.2.

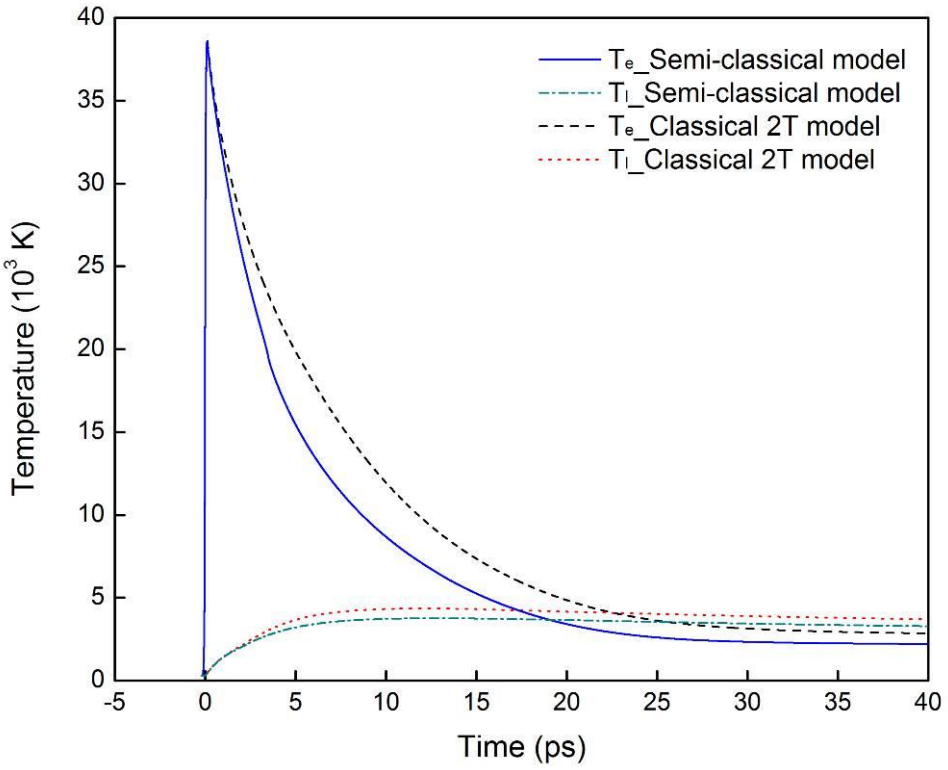

Figure 5.6 Time evolution of electron and lattice temperature at the front surface predicted by the semi-classical and classical TTM (t_p = 100 fs, J_o = 0.3 J/cm^2)

Figure 5.7 shows the distributions of lattice temperature in the front part (0 – 200 nm) of the film at different time instants. The peak lattice temperature occurs inside the film at t = 3 ps, indicating that the superheating process of melting already occurs. The double humps of the lattice temperature at t = 10 ps, 20 ps and 50 ps reveal that the material is under rapid melting and also vaporization. The bottom of the valley that is moving towards to the deeper part of the film is the S-L interface, while the lower temperature of the front surface than its adjacent material means that evaporation is also occurring there. At t = 20 ps, the liquid part of the gold film is superheated up to 3,880 K (the normal boiling point is 3,127 K) and the solid part 3,840 K (the normal melting point is 1,336 K). As more heat diffusing away as time prolongs, at t = 100 ps for example, evaporation no

longer takes place but only melting keeps on. The maximum temperature of the superheated solid is 2,280 K at this moment. At t = 1,000 ps, the melted solid is in the re-solidification process and the S-L interface is moving back to the front surface. The undercooling phenomenon is clearly exhibited by the peak lattice temperature.

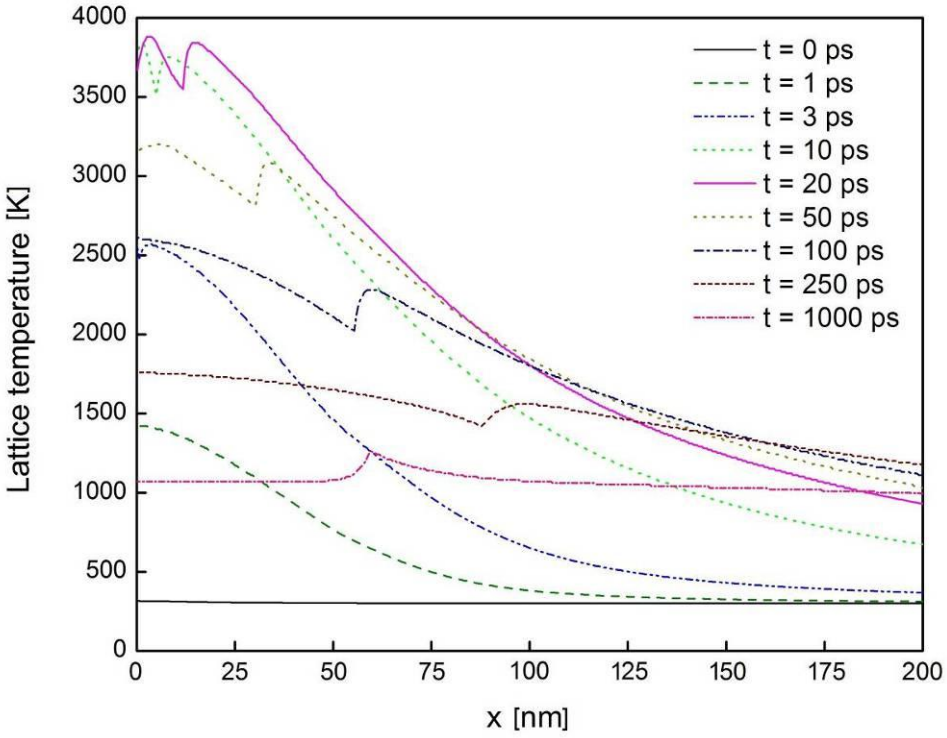

Figure 5.7 Distribution of lattice temperature in the depth 0-200 nm of the gold film at different times (t_p = 100 fs, J_o = 0.3 J/cm^2)

Figure 5.8 depicts the S-L interfacial velocity and location simulated by the two models, respectively. The peak melting velocity, total time of phase change, and maximum melt depth are 662 m/s, 1,639 ps, and 93 nm predicted by the semi-classical TTM, compared to 717 m/s, 1,936 ps, and 107 nm predicted by the classical model. At this level of laser fluence 0.30 J/cm^2, the S-L phase change is very radical in comparison

to that caused by the 0.15 J/cm^2 laser pulse.

The evaporation velocity and depth are shown in Fig. 5.9. Similar to the S-L phase change, the classical TTM results in a higher evaporation velocity and larger ablation depth. The predicted peak velocity and depth are 21.8 m/s and 0.65 nm, versus 8.2 m/s and 0.18 nm obtained from the semi-classical TTM.

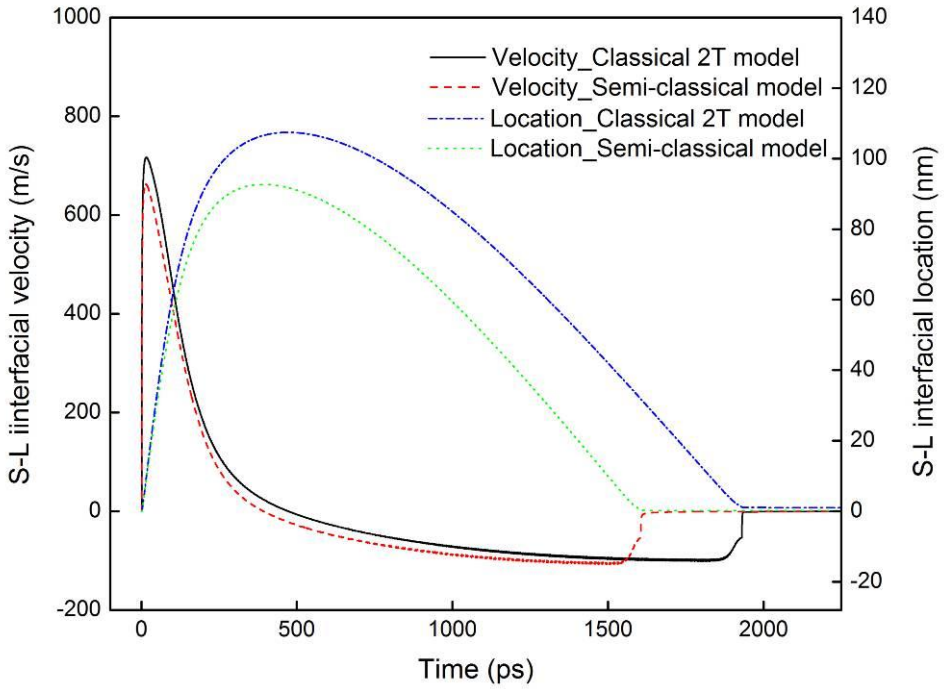

Figure 5.8 Solid-liquid interfacial velocity and location predicted by the semi-classical and classical TTM (t_p = 100 fs, J_o = 0.3 J/cm^2)

Figure 5.10 plots the volumetric laser heat source distribution at different time instants in the front part (0 – 100 nm) of the gold film heated by a 10-ps laser pulse of J_o = 0.68 J/cm^2. The deposited laser energy density at the front surface reaches its peak value 1.47×10^{16} W/cm^3 at t = 1.145 ps, while it is only 0.16×10^{16} W/cm^3 computed with the constant R and α at RT. Again, the volumetric laser heat source distributions

with different peak values and different slopes showed in Fig. 5.10 reveals the importance of use of dynamic R and α in the ultrafast laser heating modeling, even for the 10-ps laser pulse.

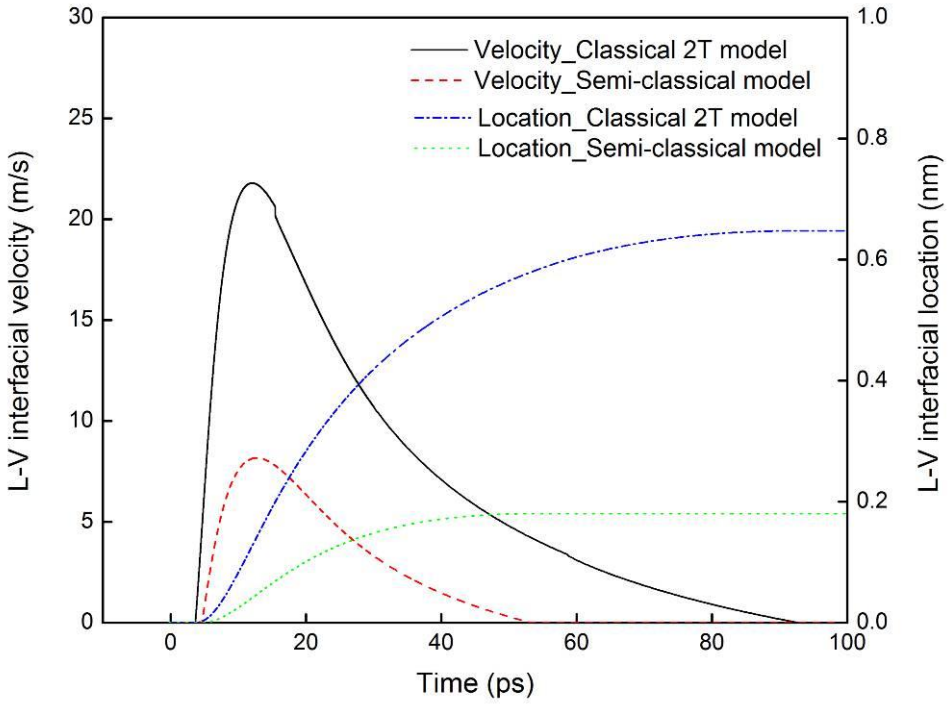

Figure 5.9 Liquid-vapor interfacial velocity and location predicted by the semi-classical and classical TTM (t_p = 100 fs, J_o = 0.30 J/cm^2)

The time histories of electron and lattice temperature at the front surface of the film are presented in Fig. 5.11. Unlike the 100-fs laser case, the difference of electron temperature calculated by the semi-classical and classical TTM is more distinct in this 10-ps laser pulse case. The peak electron temperatures obtained from the two models are quite different, 22,071 K versus 27,088 K. This is because the electrons have more time to convert the absorbed laser energy into kinetic energy for electron drifting during the laser irradiation. The difference between the lattice temperatures is also pronounced; the

peak value is 4,209 K versus 5,221 K.

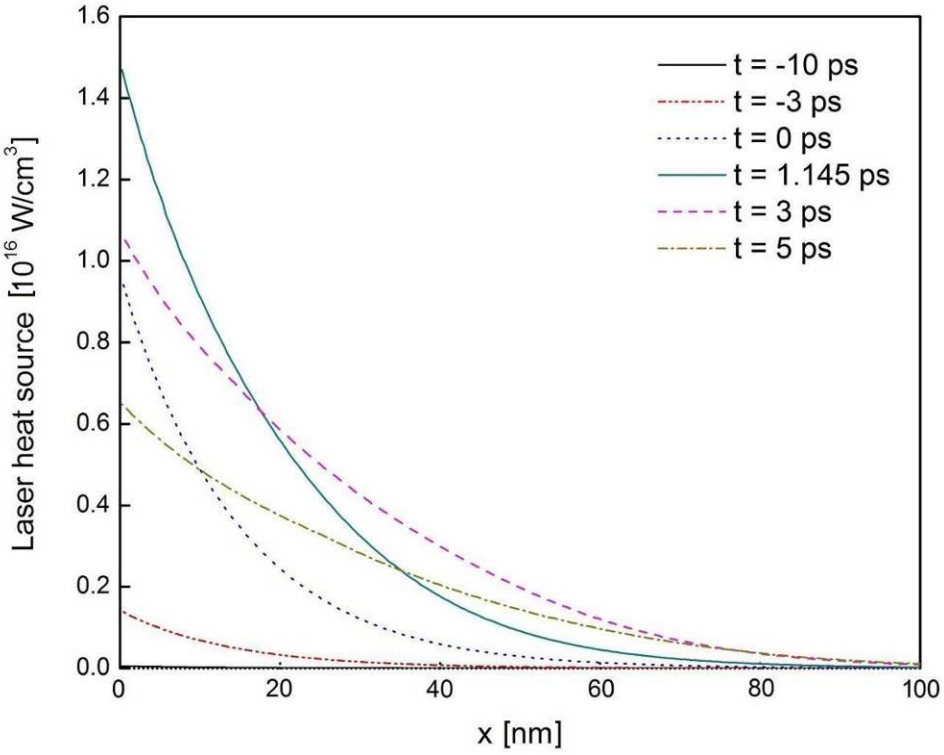

Figure 5.10 Distributions of volumetric laser heat source in the depth 0-100 nm of the gold film at different times (t_p = 10 ps, J_o = 0.68 J/cm^2)

Figure 5.12 shows the S-L interfacial velocity and location. The peak melting velocity, total time of the phase change, and maximum melting depth predicted by the semi-classical TTM are 689 m/s, 2,400 ps, and 126 nm, compared to 769 m/s, 3,976 ps, and 181 nm predicted by the classical TTM. Again, the latter over-describes the response of the S-L phase change. A similar conclusion can be made for the L-V phase change. As shown in Fig. 5.13, the peak evaporation velocity, total time of the L-V phase change, and maximum evaporation depth predicted by the semi-classical TTM are 17.9 m/s, 78 ps, and 0.44 nm, compared to 56.2 m/s, 178 ps, and 2.26 nm predicted by the classical TTM.

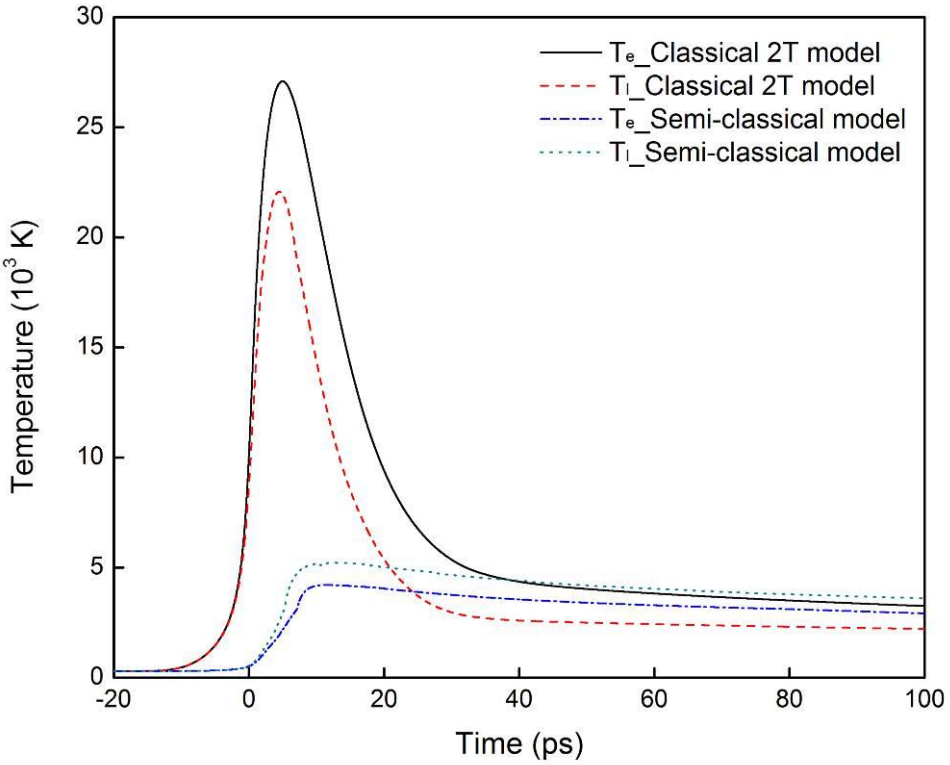

Figure 5.11 Time evolution of electron and lattice temperature at the front surface predicted by the semi-classical and classical TTM (t_p = 10 ps, J_o = 0.68 J/cm^2)

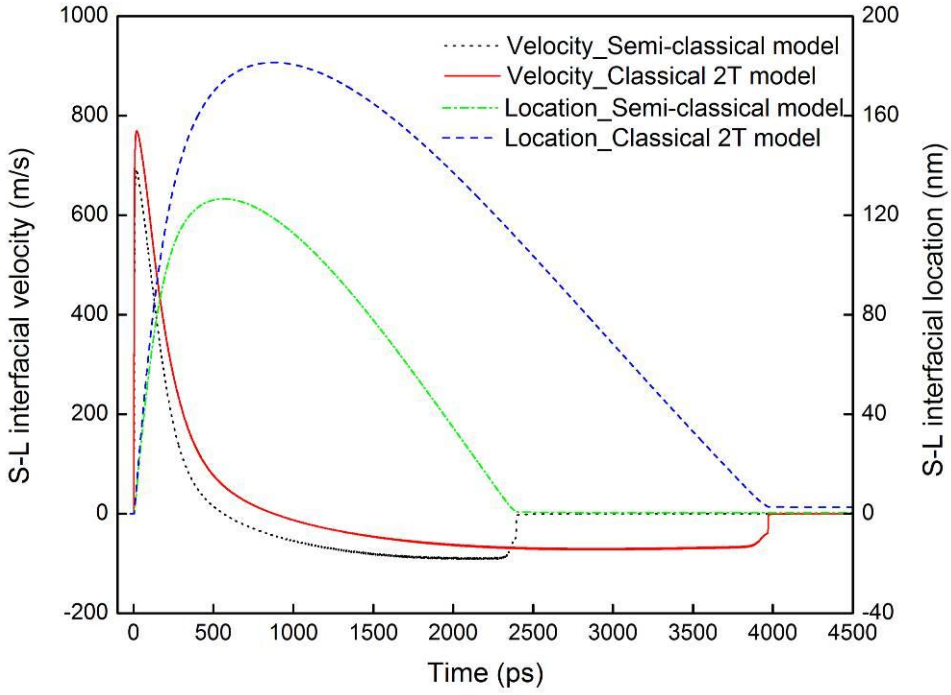

Figure 5.12 Solid-liquid interfacial velocity and location predicted by the semi-classical and classical TTM (t_p = 10 ps, J_o = 0.68 J/cm^2)

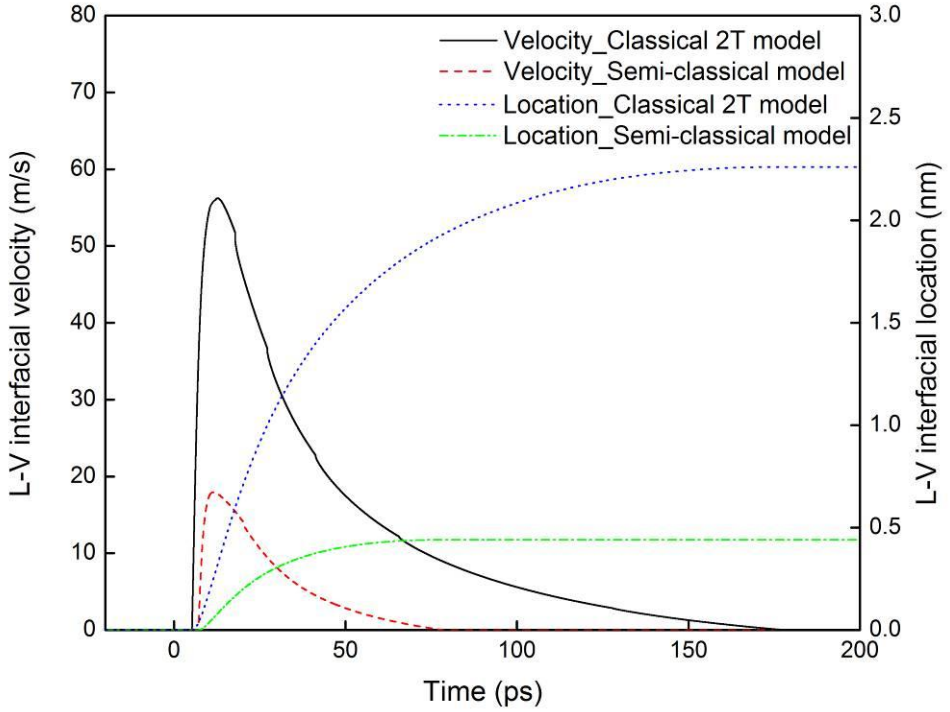

Figure 5.13 Liquid-vapor interfacial velocity and location predicted by the semi-classical and classical TTM (t_p = 10 ps, J_o = 0.68 J/cm^2)

5.3 Conclusion

A semi-classical TTM, together with the extended Drude model for temperature-dependent optical properties, was proposed to describe ultrafast thermal transport and ultrafast phase changes in gold films irradiated by ultrashort-pulsed lasers. The numerical analyses were performed for a 1-μm gold film irradiated by two 700-nm laser pulses of 100 fs and 10 ps. It was found that the significant changes in R and α due to rapid temperature rise could drastically alter laser energy deposition and in turn, the thermal response in a metal film. It was also found that the classical TTM predicts higher electron and lattice temperature and the response of solid-liquid and liquid-vapor phase change as well. For the gold film heated by a 100-fs laser pulse at fluence 0.3 J/cm^2, the differences

of the peak lattice temperature at the irradiated surface, peak melting velocity, total time of solid-liquid phase change, and the maximum melting depth simulated by the two models are 16%, 11%, 18%, and 15%, respectively. The differences become 24%, 12%, 66%, and 44% when the film is heated by a 10-ps laser pulse at fluence 0.68 J/cm^2. The peak electron temperatures at the irradiated surface of the gold film heated by a 100-fs laser pulse calculate from the classical and semi-classical TTMs are close, but they could be quite different for the same film heated by a 10-ps pulse.

CHAPTER 6: ENERGY TRANSPORT IN METAL FILMS IRRADIATED BY LASER BURSTS

6.1 Introduction

Ultrashort laser pulses can be generated by a mode-locked laser in the form of pulse train. With the rapid development of modern laser technology to date, it has been possible to generate almost any arbitrary pulse shapes. A pulse train generally consists of many bursts (see Fig. 6.1) with a repetition rate of KHz to MHz, in which each burst may contain several pulses with a separation time of several femtoseconds to hundreds of picoseconds [79]. Figure 6.1 shows the structure of a laser pulse train. f_{rep} and t_{sep} are the repetition rate and separation time, respectively.

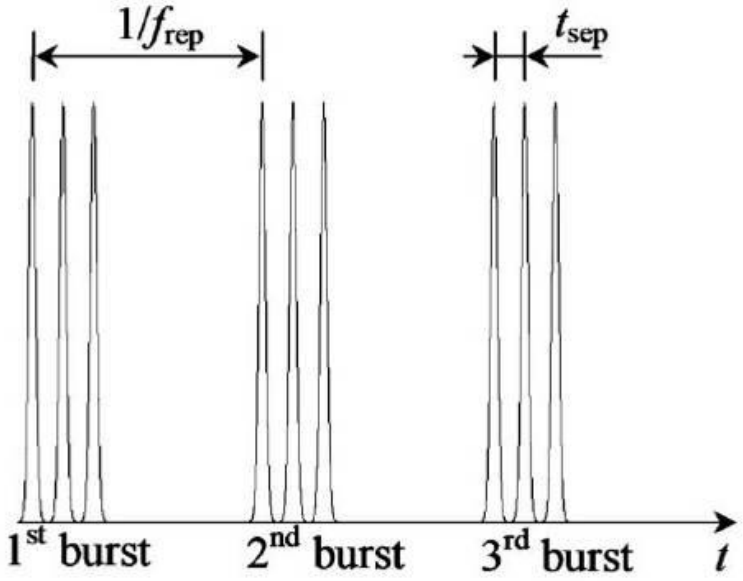

Figure 6.1 Laser pulse train

6.2 Problem Statement

In this chapter, the numerical analyses are performed for a copper film of 1-μm thickness at an initial temperature of 300 K (see Fig. 6.2). The effects of number and separation time of laser pulses are first studied for the film heated by a laser burst. Two different femtosecond laser burst are considered: one consists of three pulses and the other six pulses. All the bursts have the same total fluence 1.0 J/cm^2, and the laser wavelengths and pulse durations of all the pulses in each burst are 800 nm and 100 fs, respectively. Three separation times between pulses are 1, 10 and 100 ps. The effects of a combined nanosecond laser pulse and fs-pulse burst are also investigated. The parameters of the nanosecond laser pulse are: λ = 800 nm, t_p = 1 ns, and J_o = 0.5 J/cm^2.

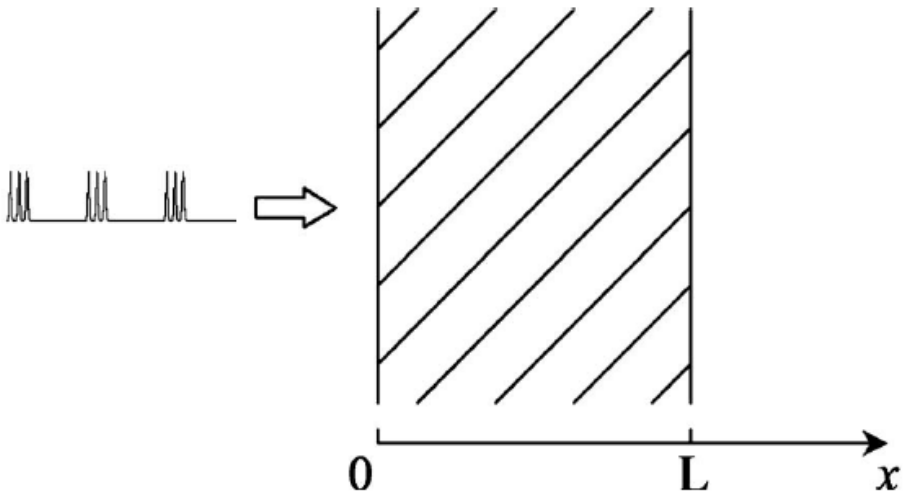

Figure 6.2 Laser pulse irradiation on a thin film

In this study, the laser heat source can be expressed as follows:

$$S = \sum_{i=1}^{K}\sum_{j=1}^{N} \frac{0.94(1-R(0,t))}{t_{pf}} \alpha(x,t) \exp\left[-\int_0^x \alpha(x,t)dx - 2.77\left(\frac{t - \frac{i-1}{f_{rep}} - (j-1)t_{sep}}{t_{pf}} \right)^2 \right] \quad (61)$$
$$+ \frac{0.94(1-R(0,t))}{t_{pn}} \alpha(x,t) \exp\left[-\int_0^x \alpha(x,t)dx - 2.77(\frac{t}{t_{pn}})^2 \right]$$

The first line is for femtosecond laser pulses with pulse duration t_{pf} and the second line is for nanosecond pulse with pulse duration t_{pn} if exists.

6.3 Results and Discussion

Figure 6.3 shows the time evolutions of electron and lattice temperature at the surface irradiated by the two femtosecond laser bursts, respectively. The pulse separation time considered here is 100 ps. For comparison, the results of the same film irradiated by a single femtosecond pulse of fluence 1.0 J/cm^2, same as the total fluence of each burst, are also presented in Fig. 6.3(a). It can be seen in Figs. 6.3(b) and 6.3(c) that in each case the peak electron temperatures produced by the pulses are gradually increasing. However, the highest electron temperature decreases with increase of pulse number. Besides heat conduction loss, this is mainly because of the smaller change of surface reflectivity due to the lower laser energy carried by each pulse in the bursts as shown in Fig. 6.4. The maximum surface reflectivity is changed from 0.958 at RT to 0.841 for the single pulse, 0.867 for the three pulses burst, and 0.891 for the six pulses burst. The smaller change in surface reflectivity results in less laser energy deposition into the film, and thereby generating lower electron temperature. The highest lattice temperatures for the three

cases are 1,814 K, 1,438 K and 1,118 K, respectively. The small bump in the lattice temperature at about t = 260 ps in Fig. 6.3(b) is due to re-solidification. In addition to the above reasons, the lower lattice temperature produced by a burst with more pulses results from slower thermal energy transferred from electrons to the lattice due to the smaller electron-phonon coupling. This suggests that for a relatively long pulse separation time, for example 100 ps, a burst with fewer pulses could generate higher lattice temperature should the total laser fluences in each train be identical. It is also found that the changes in absorption coefficient simulated are much less significant, as compared to those in surface reflectivity.

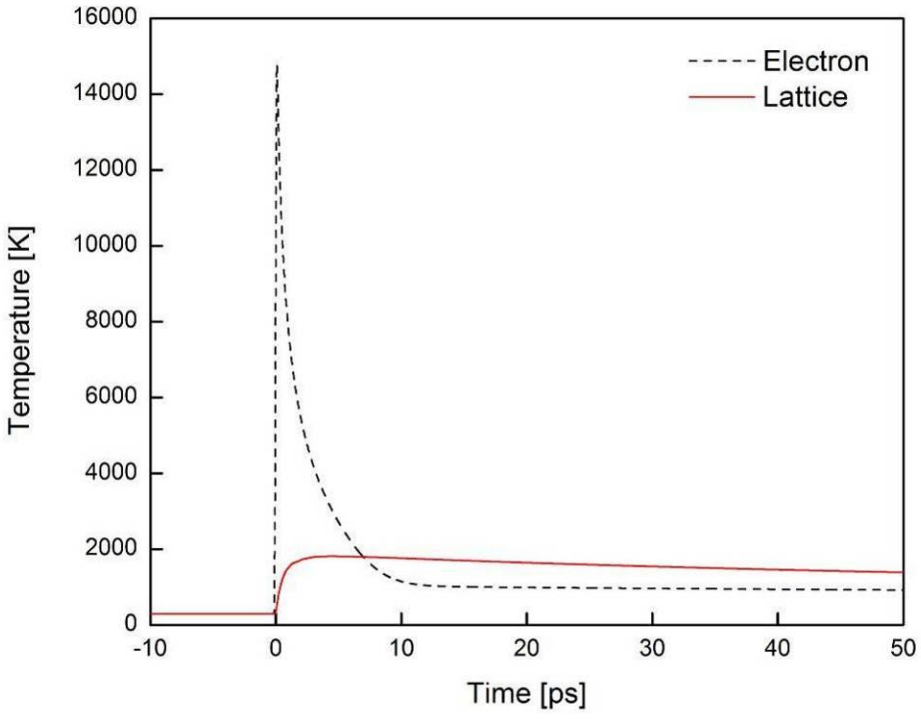

(a) single pulse

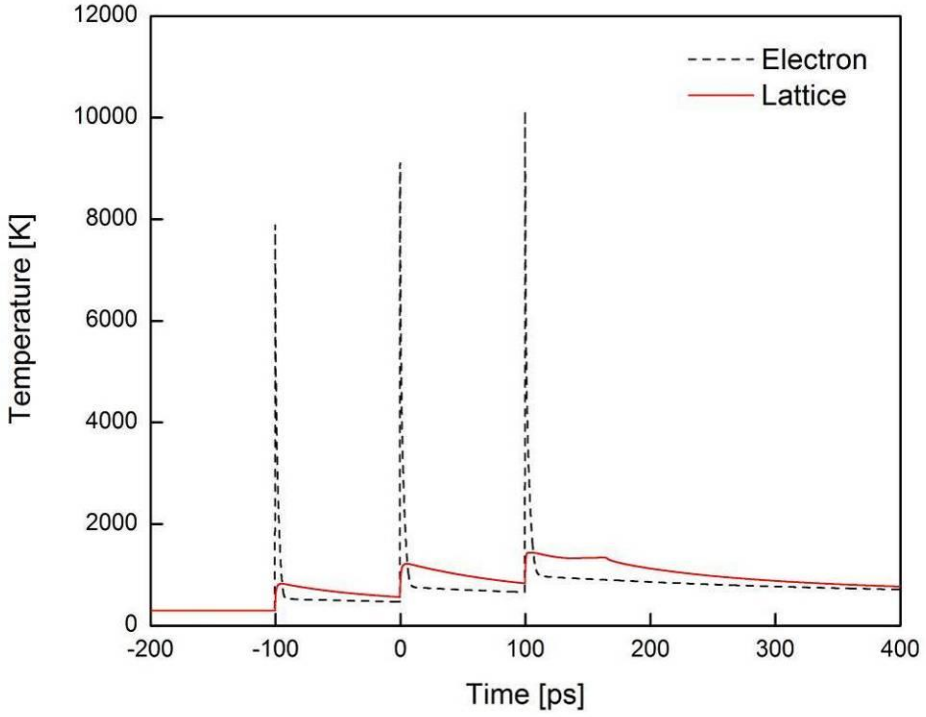

(b) three pulses

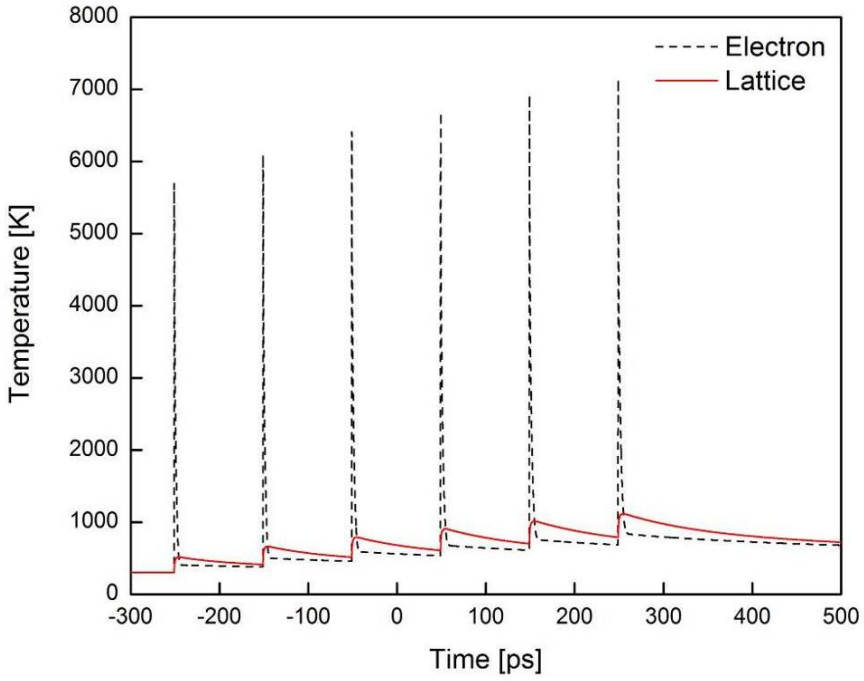

(c) six pulses

Figure 6.3 Evolutions of electron and lattice temperature at the irradiated surface by femtosecond laser pulse bursts with total fluence J = 1.0 J/cm^2 and t_{sep} = 100 ps: (a) single pulse, (b) three pulses, (c) six pulses

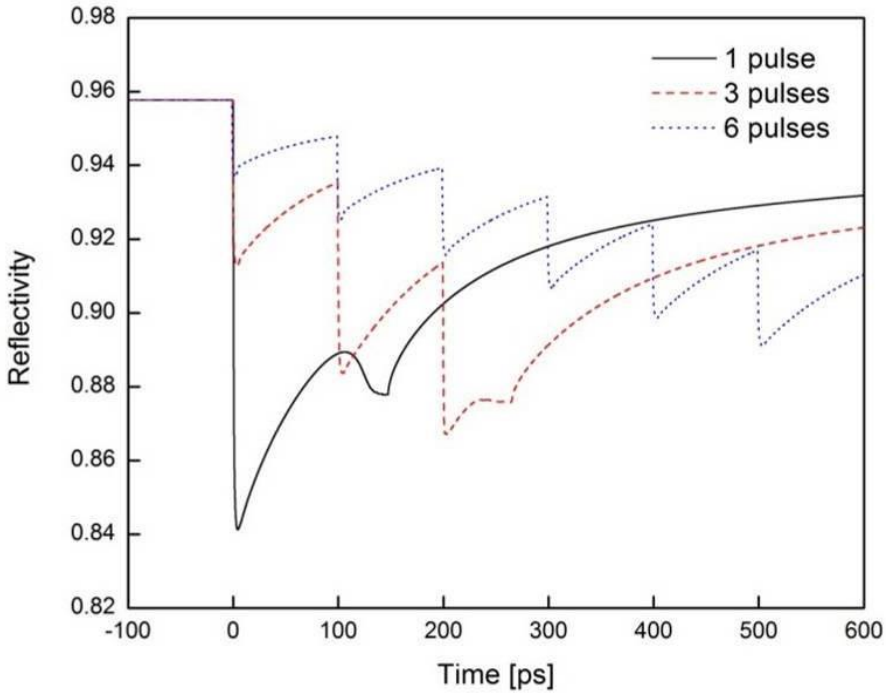

Figure 6.4 Changes of surface reflectivity by different pulse bursts with t_{sep} = 100 ps

Figure 6.5 demonstrates the influence of pulse separation time on the electron and lattice temperature for t_{sep} = 1 ps and 10 ps. Comparing the results in Figs. 6.3 and 6.5 shows that the highest electron temperature increases with decrease of separation time, and so does the lattice temperature. It, however, is interesting to note the maximum lattice temperatures: 2,441 K for the three pulses and 2,532 K for the six pulses in the 1-ps separation time case and 2,282 K and 1,961 K in the 10-ps separation time case. The above results along with those in the 100-ps separation time case imply that heat conduction in electrons and lattice is another important factor that affects temperature and optical response. For a shorter pulse separation time, the electrons and lattice may not have enough time to transfer thermal energy to deeper parts of material before the next pulse arriving. Thus, the incubation effect could be more significant for a laser burst with

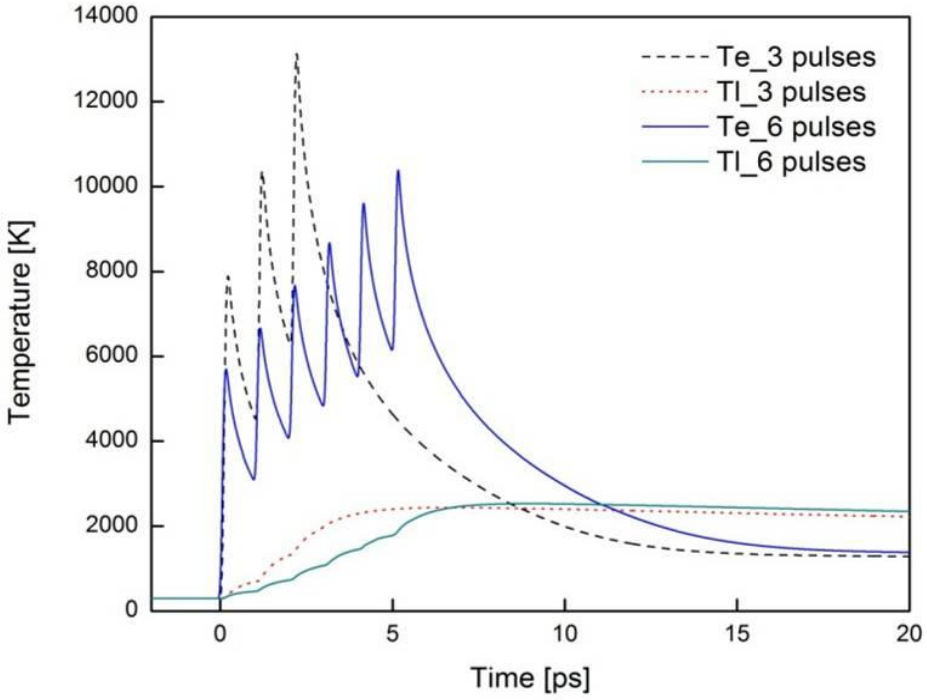

(a) t_{sep} = 1 ps

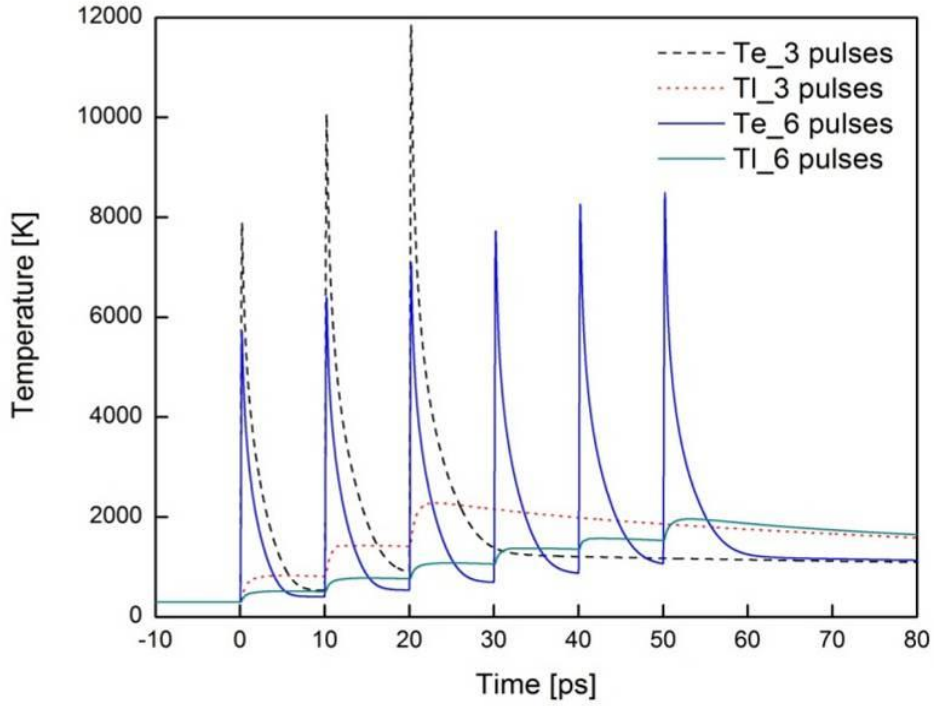

(b) t_{sep} = 10 ps

Figure 6.5 Time histories of electron and lattice temperature at the irradiated surface by femtosecond laser bursts with total fluence J = 1.0 J/cm^2: (a) t_{sep} = 1 ps, (b) t_{sep} = 10 ps

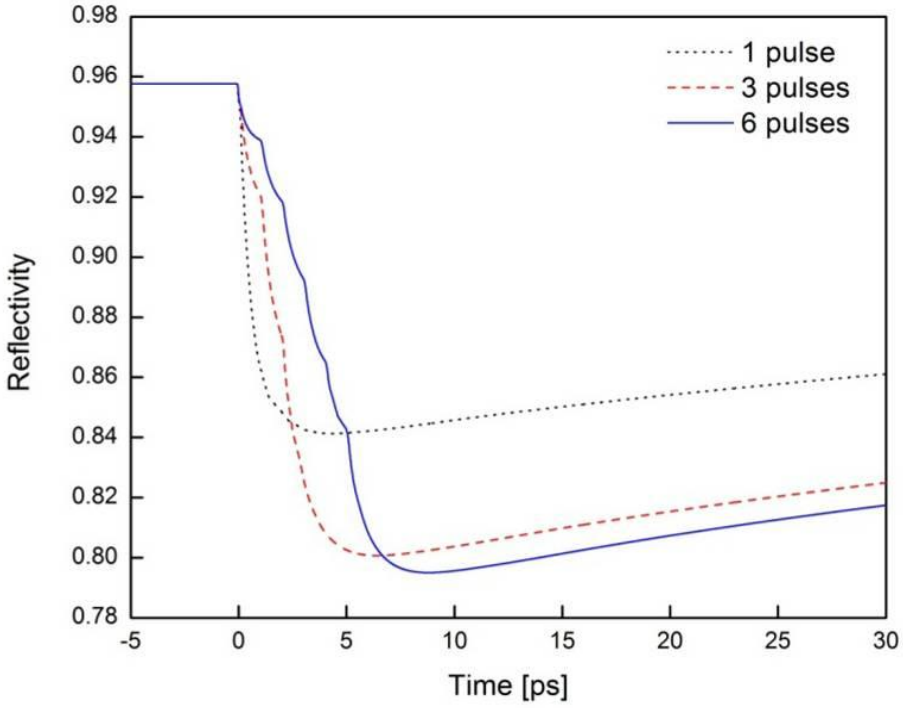

(a) t_{sep} = 1 ps

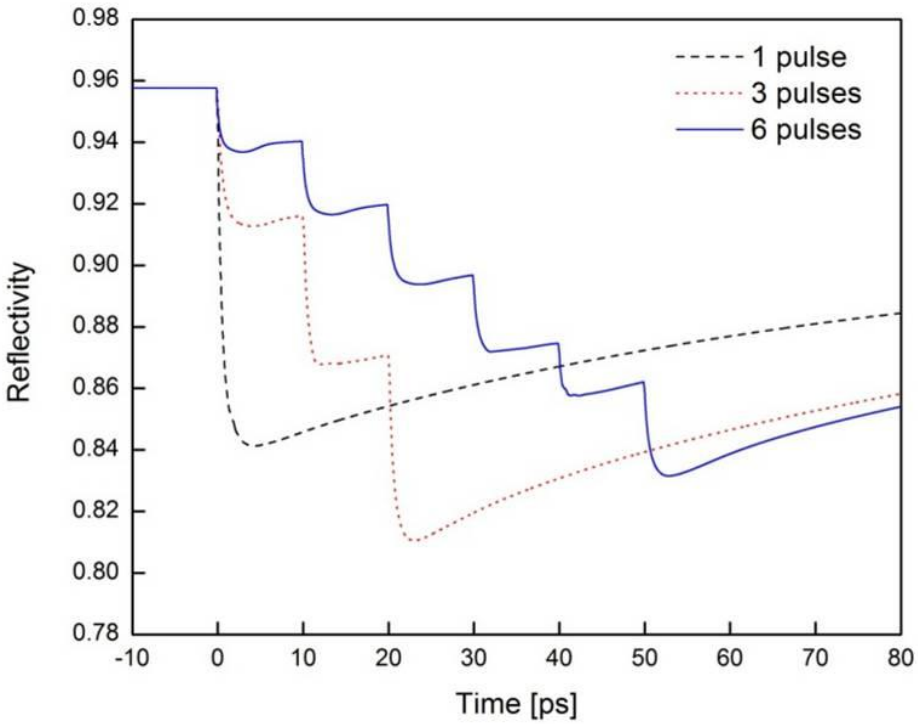

(b) t_{sep} = 10 ps

Figure 6.6 Change of surface reflectivity by femtosecond laser bursts with total fluence J = 1.0 J/cm^2: (a) t_{sep} = 1 ps, (b) t_{sep} = 10 ps

more pulses. Figure 6.6 depicts the transient change of surface reflectivity. The orders of the maximum change in the surface reflectivity are: 6, 3 and 1 pulse for the 1-ps separation time (Fig. 6.6(a)), 3, 6 and 1 pulse for the 10-ps separation time (Fig. 6.6(b)), and 1, 3 and 6 pulses for the 100-ps separation time (Fig. 6.4). These results of surface reflectivity give further explanation for the thermal responses shown in Figs. 6.3 and 6.5. To obtain higher lattice temperature, more pulses should be used in a burst for shorter separation time, such as 1 ps and fewer pulses should be used for longer pulse separation time such as 100 ps.

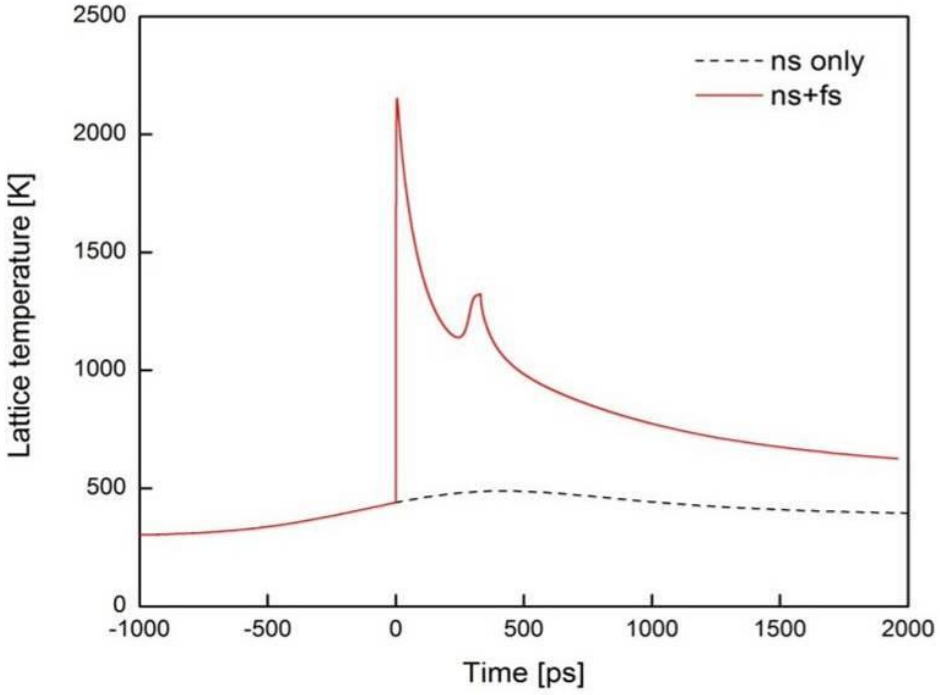

Figure 6.7 Lattice temperature at the irradiated surface induced by a dual ns-fs laser beam and by the nanosecond pulse alone

Figure 6.7 compares the lattice temperatures at the irradiated surface by a combined nanosecond and fs-laser pulse and by the nanosecond pulse alone. Recall that the fluences

are 0.5 J/cm^2 in the nanosecond laser pulses and 1.0 J/cm^2 in femtosecond pulse. It is found that the two maximum lattice temperatures are 2,153 K and 489 K. The rise of the peak lattice temperature by the nanosecond laser pulse alone is only 189 K, while that by the femtosecond pulse alone is 1,514 K (Fig. 6.3). It thus appears that an integrated fs-ns dual beam can enhance thermal response through optical property changes by adding a nanosecond pulse. The bump shown in Fig. 6.7 is due to material solidification.

The lattice temperatures at the irradiated surface by the dual beams of a nanosecond pulse with a three fs-pulses burst are shown in Fig. 6.8 for three pulse separation times 1 ps, 10 ps and 100 ps. As expected, the lattice temperature decreases as the pulse separation time increases. The highest temperatures are 2,793 K, 2,656 K, and 1,741 K, respectively. The change of the rise of the lattice temperature is increased by 16% for the 1-ps separation time, 19% for the 10-ps separation time, and 27% for the 100-ps separation time, respectively, compared to those cases of the three-femtosecond pulse bursts in Figs. 6.3(c) and 6.5. Recall that the peak lattice temperature is 2,153 K for the combined nanosecond and femtosecond pulse (Fig. 6.7) and 1,814 K for the femtosecond pulse alone (Fig. 6.3). These results indicates that for a dual beam with a 3 fs-pulses burst, the shorter the separation time is, the more the lattice temperature increases.

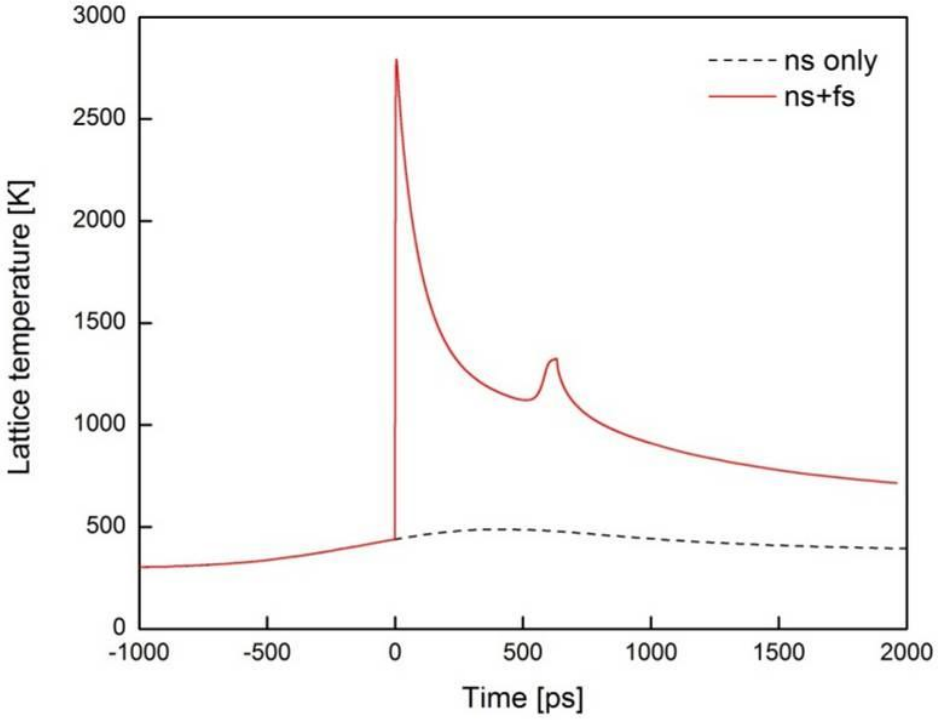

(a) t_{sep} = 1 ps

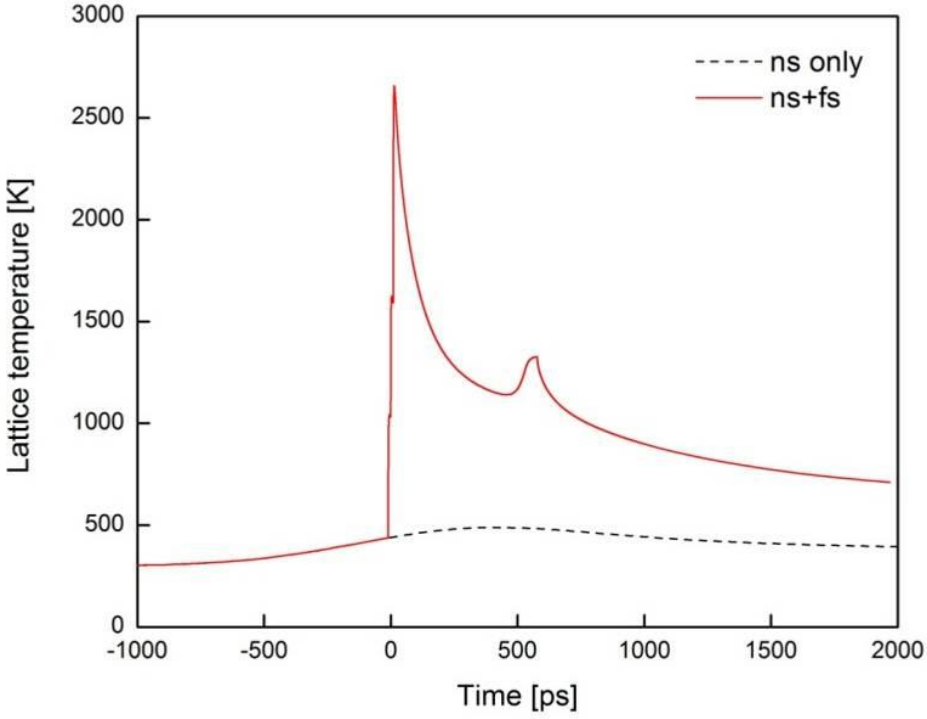

(b) t_{sep} = 10 ps

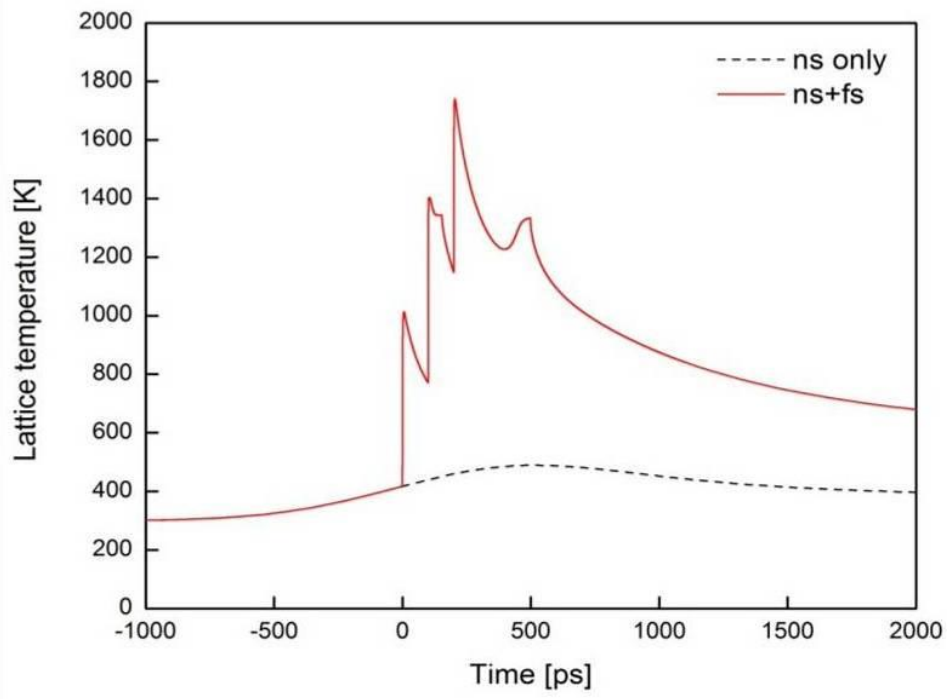

(c) t_{sep} = 100 ps

Figure 6.8 Lattice temperatures at the irradiated surface induced by the dual laser beam of a nanosecond pulse and a three fs-pulses burst: (a) t_{sep} = 1 ps, (b) t_{sep} = 10 ps, (c) t_{sep} = 100 ps

Figure 6.9 shows the lattice temperatures at the irradiated surface by a dual beam of the nanosecond pulse and a 6 fs-pulses burst with separation time of 10 ps. In this case, the highest lattice temperature is 2,306 K, which is lower than 2,656 K produced by the dual beam with the 3-pulse train and the same separation time. Further simulations for the dual beam with a 6-pulse train give the maximum lattice temperature 2,928 K for the 1-ps separation time and 1,402 K for the 100-ps separation time, compared to 2,793 K and 1,741 K for the dual beam with a 3-pulse train, respectively.

From the above results for the dual laser beams, it can be concluded that with the recent laser pulse train technology, the lattice temperature response can be enhanced by setting the pulse separation time as short as possible, for example 1 ps.

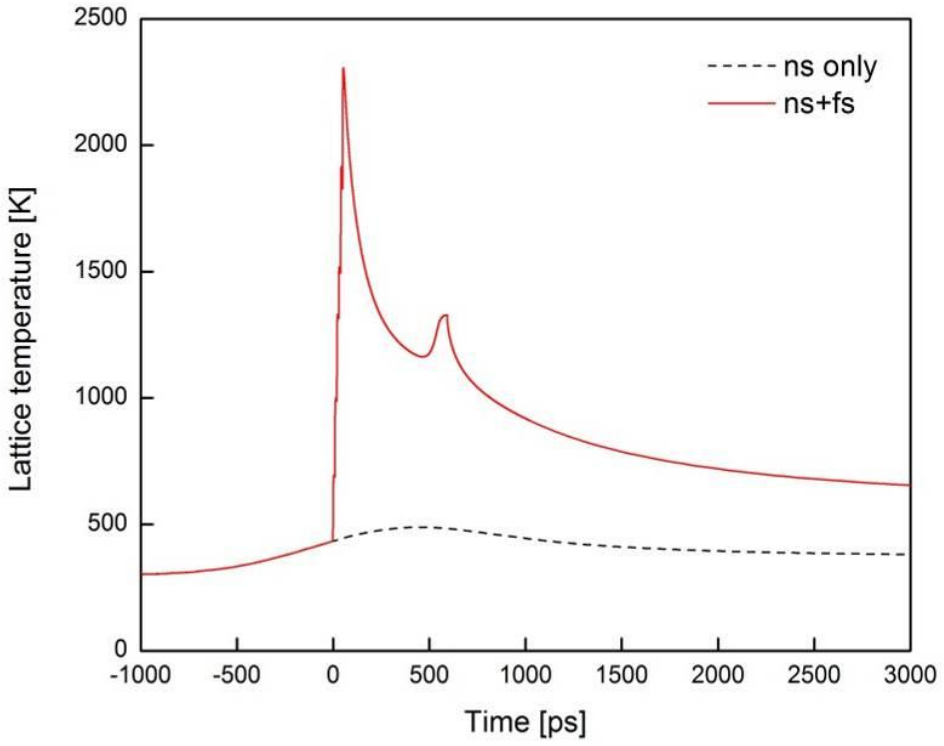

Figure 6.9 Lattice temperatures at the irradiated surface induced by the dual laser beam of a nanosecond pulse and a six fs-pulses burst with t_{sep} = 10 ps

6.4 Conclusion

The semi-classical TTM with temperature-dependent optical and thermophysical properties were proposed to study thermal response for a copper film irradiated by a femtosecond laser burst and by an integrated dual laser beam of a nanosecond pulse with a femtosecond laser burst. To study the effects of pulse number and separation time on the thermal response, two laser bursts, composing of three and six pulses each, and three separation times between pulses, 1 ps, 10 ps and 100 ps, were examined. In the numerical analysis, the total fluences were the same for all the bursts, 1.0 J/cm^2. All the pulses in each burst had the same fluence, wavelength 800 nm, and duration 100 fs. The parameters of the nanosecond laser pulse were: λ = 800 nm, t_p = 1 ns, and fluence 0.5

J/cm^2. For comparison, the results of the copper film irradiated by a single femtosecond pulse of fluence 1.0 J/cm^2 were also presented. The following conclusions were drawn:

(1) The change of optical properties at high temperatures is the main factor that alters the thermal response of a metal film induced by ultrafast laser heating.

(2) Pulse separation time controls the incubation effect. The shorter the separation time is, the less the heat is conducted. Thus, lattice temperature can be enhanced by a laser burst with a shorter pulse separation time, especially for separation time less than 10 ps.

(3) To obtain higher lattice temperature, more pulses should be used in a laser burst with shorter pulse separation time such as 1 ps and fewer pulses in a burst with longer pulse separation time such as 100 ps.

(4) Although the peak power of a nanosecond laser pulse is very small compared to that of a femtosecond laser pulse at similar level of fluence, combining a femtosecond laser burst to a nanosecond laser pulse can enhance the thermal response, especially for shorter pulse separation time.

(5) The lattice temperature produced by a dual laser beam of a nanosecond pulse and a femtosecond laser burst can be increased by setting the pulse separation time as short as possible, for example 1 ps.

CHAPTER 7: THERMAL ABLATION BY ULTRASHORT PULSED LASERS

7.1 Problem Statement

The numerical simulations of laser material ablation are carried out for laser pulses of 120 fs and 800 nm at different fluences. A number of 2,500 finite volumes per micron are modeled in the copper films of different thicknesses varying from 1 μm to 5 μm, depending on laser fluence. When the calculated temperature in a finite volume (liquid lattice) reaches $0.9T_c$ (T_c = 7,696 K for copper [80]), phase explosion is assumed to take place and that finite volume is removed from the model.

Due to the surface receding from laser ablation, the incoming laser pulses will impinge onto the new front surface of a film. The volumetric laser heat source given by Eq. (61) is still applicable with a dynamical shift of the origin of the x-coordinate to the new front surface.

7.2 Results and Discussion

Figure 7.1 gives the time histories of surface reflectivity and absorption coefficient of the copper films during the laser irradiation at two fluences 1 and 10 J/cm^2. The surface reflectivity and the absorption coefficient at RT are 0.96 and 79 μm^{-1}, respectively. The Gaussian laser pulses are normalized with the peak power. It can be seen that both the reflectivity and absorption coefficient decrease with laser fluence. The reduction in surface reflectivity means more laser energy being absorbed by the material, while the reduction in absorption coefficient implies larger optical penetration depth, leading to a deeper but less steep laser energy density distribution. The change in the laser energy

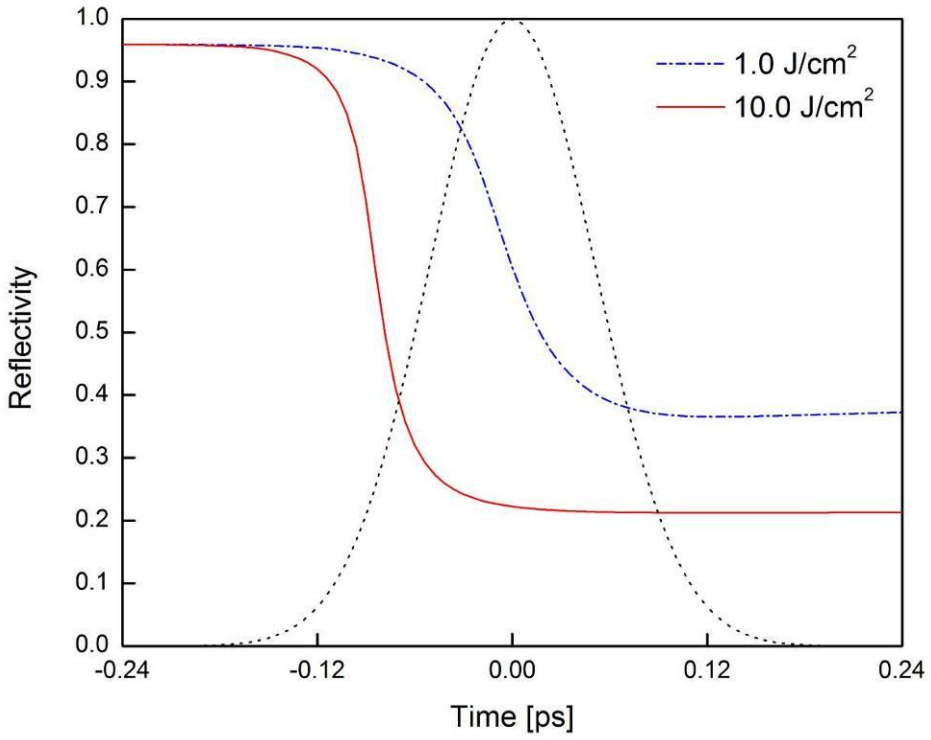

(a) surface reflectivity

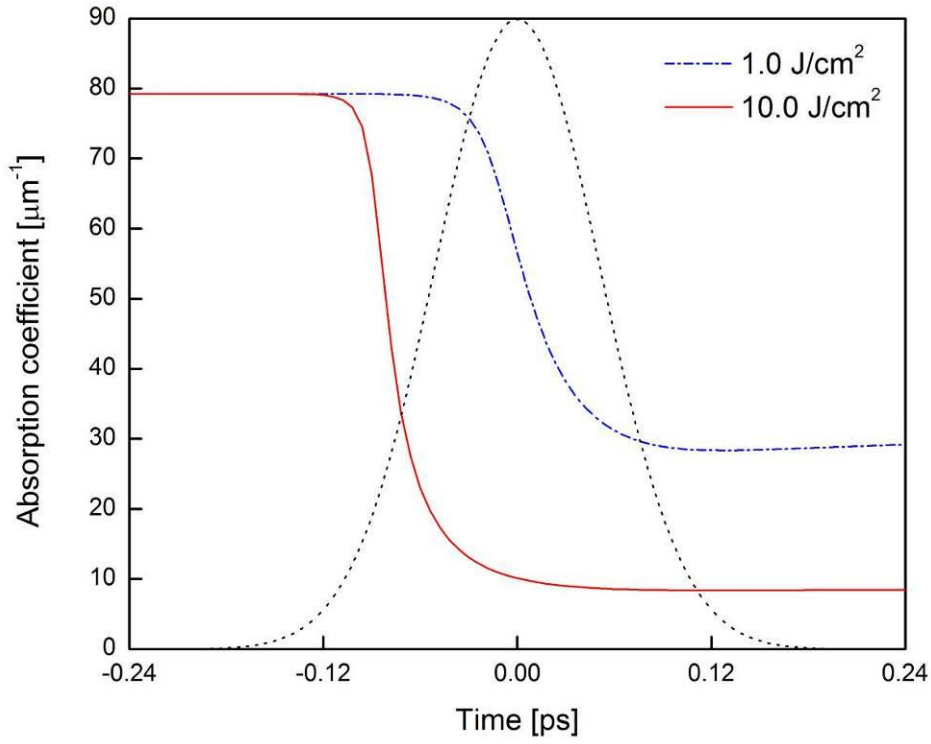

(b) absorption coefficient

Figure 7.1 Variations of surface reflectivity and absorption coefficient at the irradiated surface during lasing at fluences 1 and 10 J/cm^2: (a) surface reflectivity *R* and (b) absorption coefficient *α*

deposition caused by the changes of the two optical properties could alter the resulting thermal response and, in turn, the amount of material ablation, and thus needs to be accurately characterized.

Figure 7.2 demonstrates the superheating behavior by the distributions of lattice temperature in the front part (0 – 100 nm) of the 1-μm copper film irradiated by a laser pulse of 0.6 J/cm^2. It can be clearly observed from the figure that the two local minimum temperatures occur in the region near the front surface as early as t = 2 ps, indicating that the superheating process already occurs over there. The bottom of the valley is the temperature at the solid-liquid interface. On the other hand, the lower temperature at the front surface than in the adjacent region reveals that vaporization also takes place from the front surface. No phase explosion is simulated at this level of laser fluence since the maximum temperature is smaller than the value of $0.9T_c$.

The time histories of laser material ablation are shown in Fig. 7.3 for three different fluences. As seen in the figure, the first (steep) parts of material ablation mainly result from phase explosion, with a small portion of contribution from vaporization occurring in the early time before phase explosion. The second (sloping) parts are caused by vaporization only. It is evident, by comparing the amounts of material removed by vaporization and phase explosion, that phase explosion is the dominating mechanism for the ultrafast thermal ablation. For the case of J_o = 8 J/cm^2, for example, the simulated amounts of the ablated material by vaporization are 0.03 nm and 22.4 nm before and after the phase explosion, while the amount by the phase explosion is 202.4 nm. It is also obvious that the greater the fluence is, the earlier the sputtering starts and the later the sputtering completes, and the more the material is ablated.

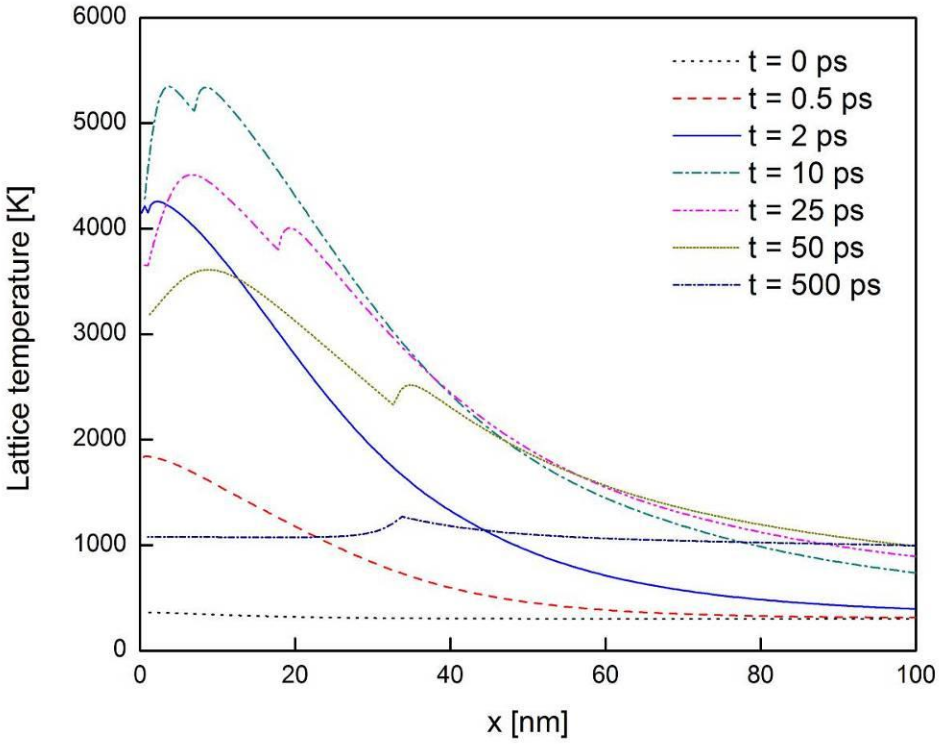

Figure 7.2 Lattice temperature distributions in the first 0-100 nm depth of the 1-μm copper foil irradiated by the laser pulse of 0.6 J/cm^2

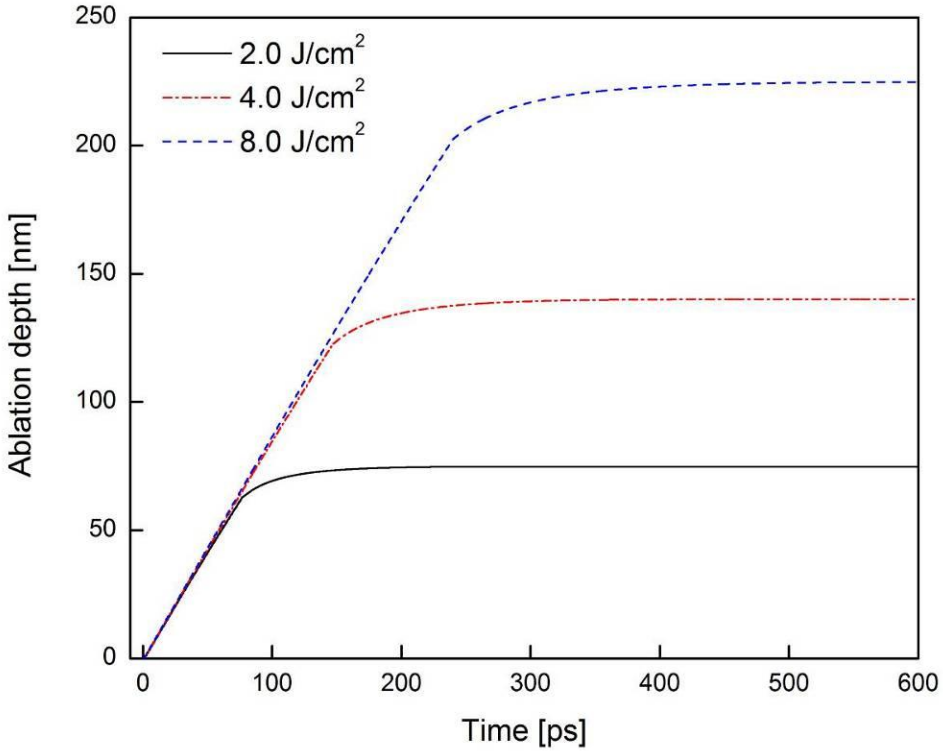

Figure 7.3 Ablation depth against time for three laser fluences 2, 4 and 8 J/cm^2

Figure 7.4 compares the ablation depth between the numerical simulations and experimental measurements. It appears that the present simulation results agree well with the experimental data [81] over a large range of laser fluences up to 30 J/cm^2. For the lower fluences (< 0.6 J/cm^2), the ablation may be controlled essentially by non-thermal ablation mechanisms such as ultrafast thermal stresses, coulomb explosion, and/or hot electron blast, which is beyond the scope of this work.

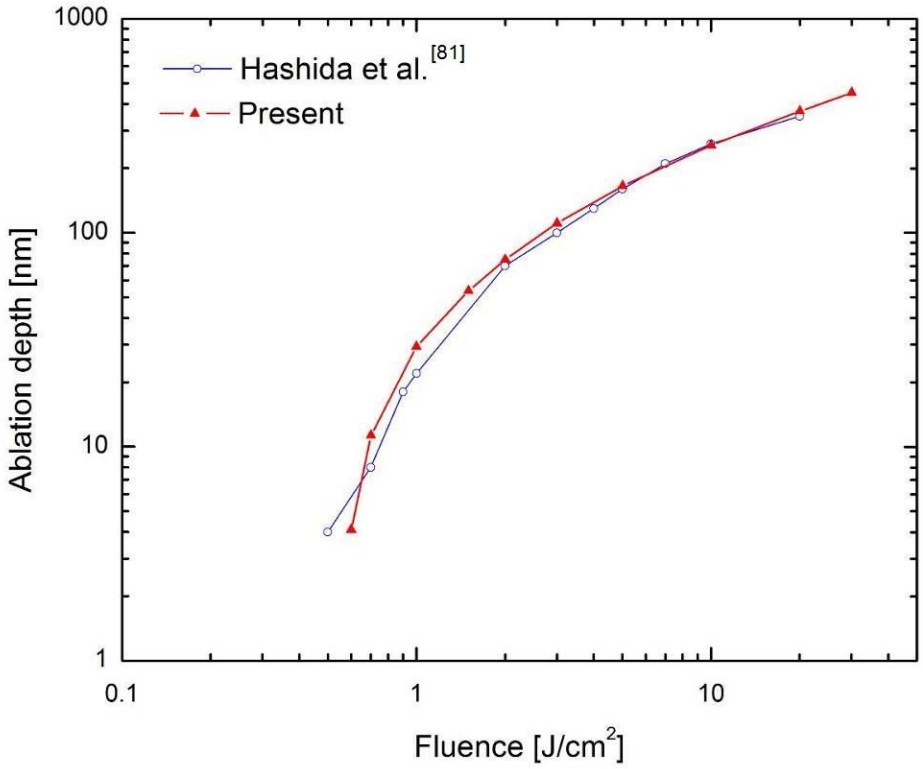

Figure 7.4 Comparison of ablation depths between simulations and experimental data

Figure 7.5 shows the amounts of material ablated by laser bursts. In these simulations, the numbers of pulses in the laser bursts vary from 2 to 10 and the five pulse separation times range from 1 ps to 500 ps. The total laser fluences considered here are the same, 5 J/cm^2, for the single pulse and all the bursts. It can be seen from Fig. 7.5 that for the pulse

separation times of 50 ps and longer, a laser burst can ablate more material than a single pulse. The ablation depth could be even larger as pulse number increases. For the short separation times, e.g., 1 ps and 10 ps, on the other hand, the ablation depths are about the same as that yielded by the single pulse. The reasons for such results may be attributed to four competing factors – absorption of laser energy, heat conduction, electron-lattice thermalization, and material ablation.

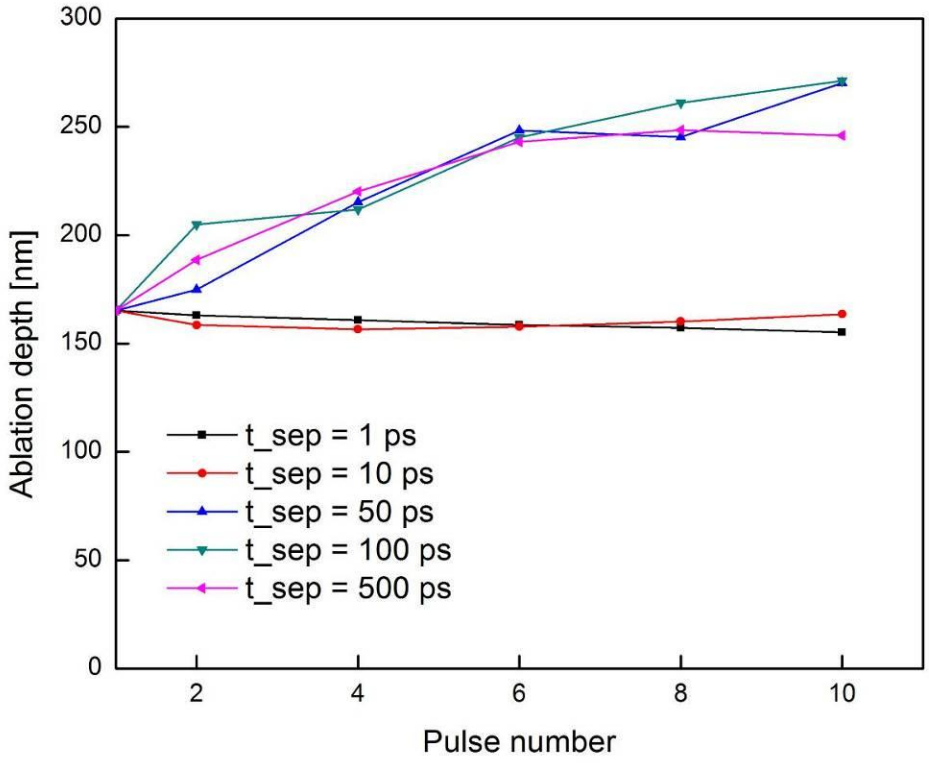

Figure 7.5 Ablation depths induced by single shot and burst mode with total fluence of 5 J/cm^2

For the short pulse separation times of 1 ps and 10 ps, the entire laser material ablation completes at about 300 ps, very close to that by the single pulse. This is can be seen from the time histories of material ablation shown in Fig. 7.6, in which the first (steeper) part of material ablation for about 170 ps mainly results from phase explosion

while the second (flatter) part from vaporization alone. Comparing the amounts of material removal via phase explosion and vaporization reveals that the former is a dominating mechanism for the ultrafast laser ablation at this level of fluence (5 J/cm^2). For the two laser bursts, each pulse only possesses one-eighth the total energy. Accordingly, they could generate lower electron and lattice temperature than the single pulse, leading to a higher surface reflectivity. As a result of less laser energy absorbed, these bursts could only ablate a smaller amount of material. Therefore, a laser burst with very short pulse separation time, such as 1 ps and 10 ps, may not have an advantage for material ablation over a single laser pulse. The conjecture is confirmed by the results shown in Fig. 7.5.

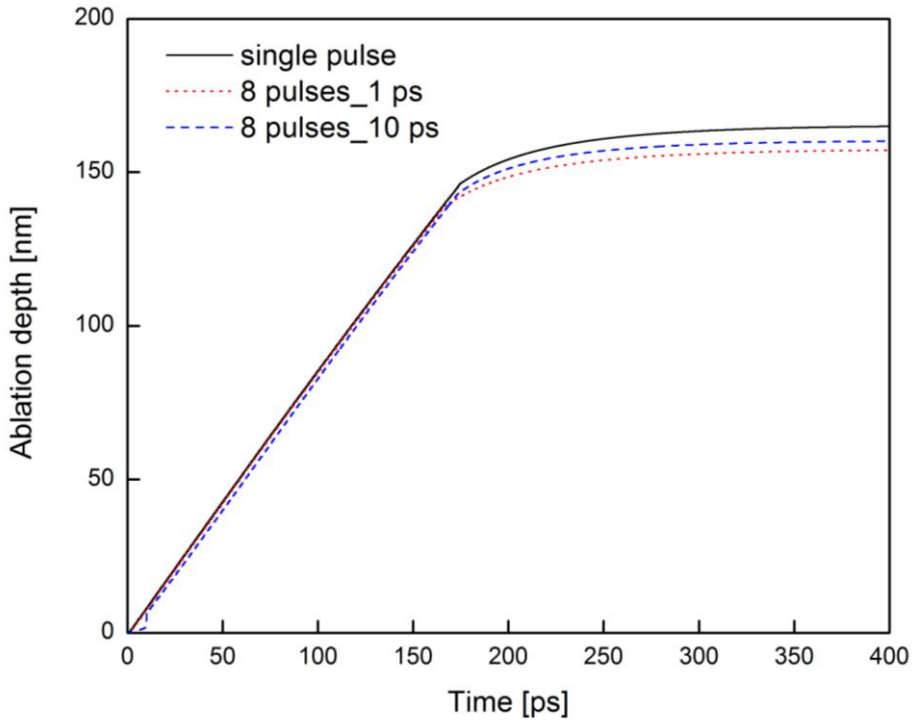

Figure 7.6 Ablation depth against time for single pulse, 8 pulses with 1 ps and 10 ps separation time with total fluence of 5 J/cm^2

Unlike the laser bursts with a very short pulse separation time, a burst consisting of the same pulses with the same total laser energy but longer pulse separation time has a different ablation performance. Before a subsequent pulse is applied, there is more time for the highly concentrated thermal energy to conduct into deeper part of the material. Instead of wasting huge energy that is removed together with the ablated material, the spread energy could heat up more material to the state of phase explosion. Therefore, more material can be ablated. This explains why a larger ablation depth is achieved by a laser burst with pulse separation times of 50 ps or longer as shown in Fig. 7.5.

Figure 7.7 shows the electron and lattice temperature distributions at different times for the laser bursts with pulse separation time 100 ps. It can be seen from Fig. 7.7(a) for the two-pulse burst that a very high lattice temperature is induced in the solid phase due to the limit of nucleation dynamics; thereby no phase explosion does take place in this overheated solid. During this short period of time, the two thermal subsystems are yet equilibrated as evidenced by the huge difference between the electron and lattice temperatures. As time prolongs, the superheated solid lattice melts from its front side by absorbing a great amount of thermal energy from the surrounding hot electrons. The newly transformed liquid becomes metastable very quickly because it keeps on absorbing vast thermal energy from the hot electrons. Upon the temperature reaching $0.9T_c$, the superheated liquid immediately decomposes into metastable liquid droplets and vapor phase and spurts out from the bulk material. This phase transition and explosion process repeats as illustrated by the recession of new front surfaces shown in Fig. 7.7(a).

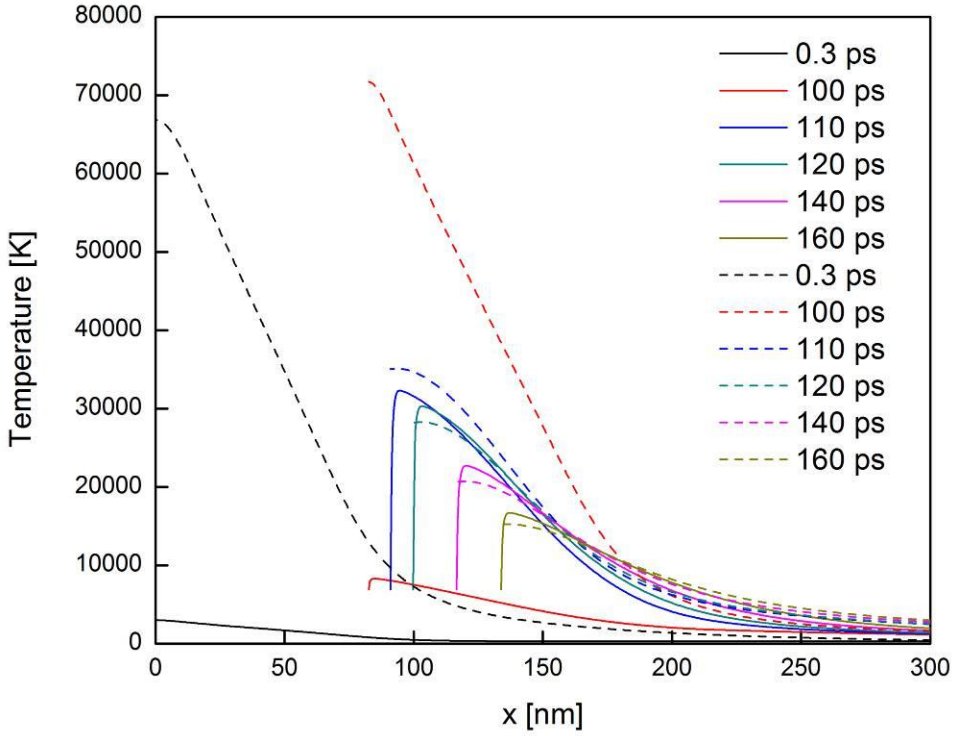

(a) 2-pulse burst

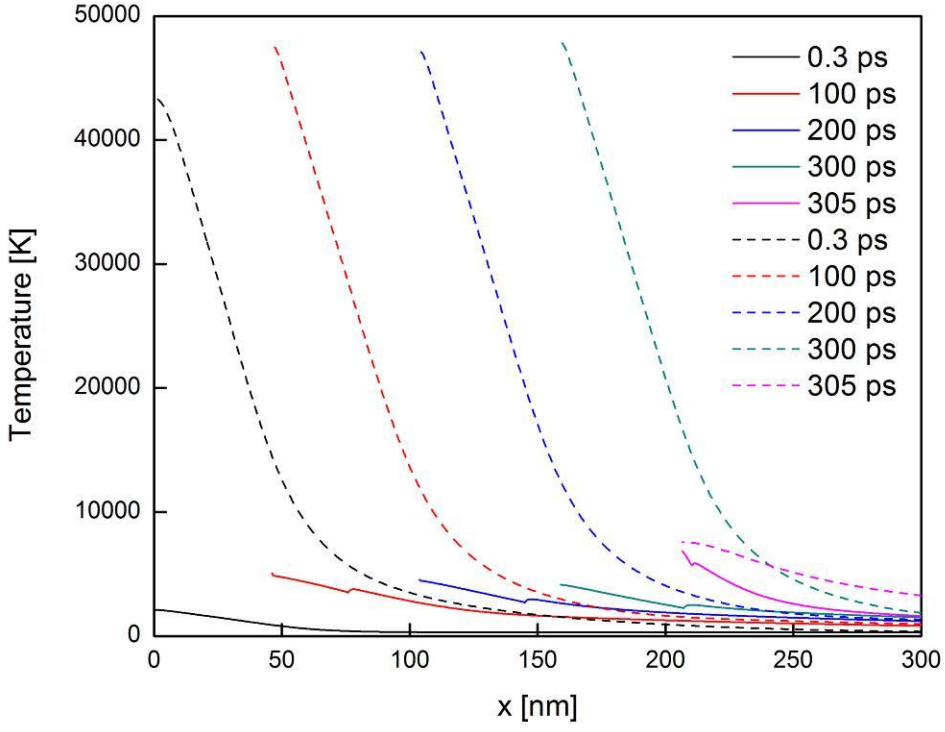

(b) 4-pulse burst

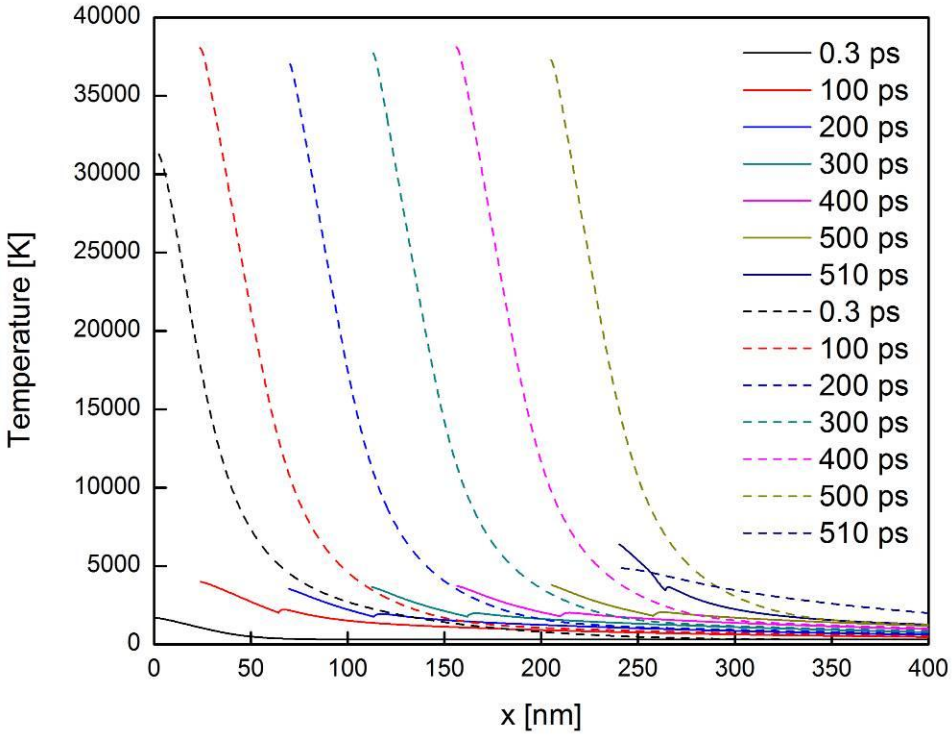

(c) 6-pulse burst

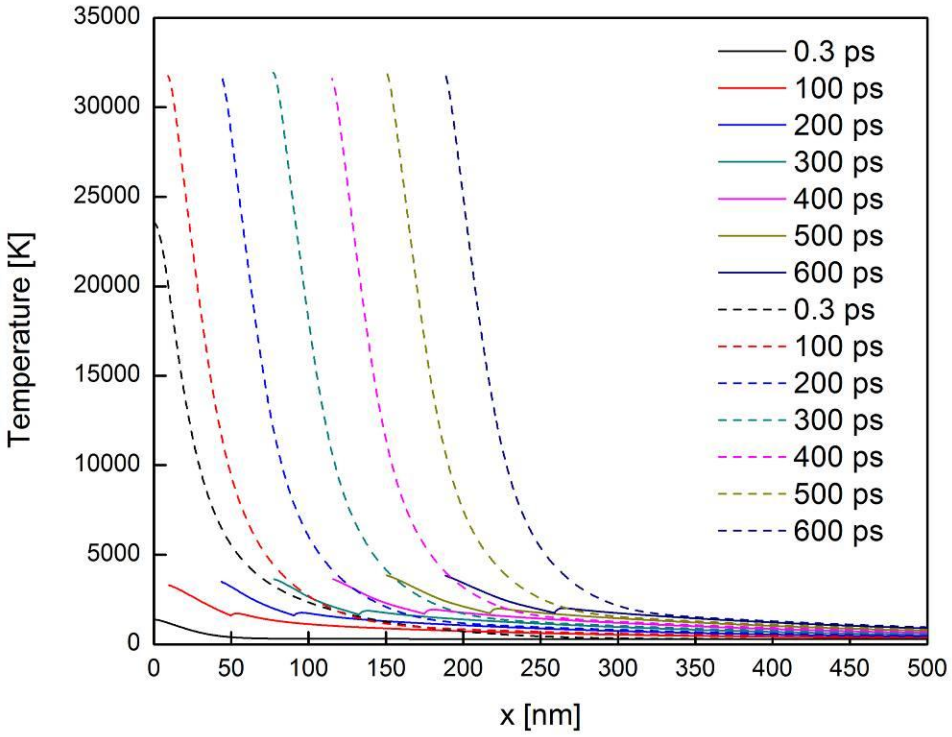

(d) 8-pulse burst

Figure 7.7 Electron and lattice temperature distributions for the bursts with 100-ps pulse separation time: (a) 2-pulse burst, (b) 4-pulse burst, (c) 6-pulse burst, and (d) 8-pulse burst

Nonetheless, the very high temperature in the overheated solid lattice is not found in Figs. 7.7(b) and 7.7(c) for the bursts composing of 4 and 6 pulses. This is due to the fact that with more pulses in a burst, each pulse contains less energy; consequently, both the solid and liquid lattices are heated up relatively slowly by the hot electrons. However, the liquid lattice received much more energy from the electrons than the solid lattice, evidenced by the difference between electron and lattice temperature shown in Fig. 7.7(b) and 7.7(c). Thus, the liquid lattice temperature is greater than the solid lattice temperature. Once the temperature of the superheated liquid lattice reaches to $0.9T_c$, it decomposes into metastable droplets and vapor phase and ejects away from the bulk material. More information about the formation and ablation of the liquid phase are given in Fig. 7.8.

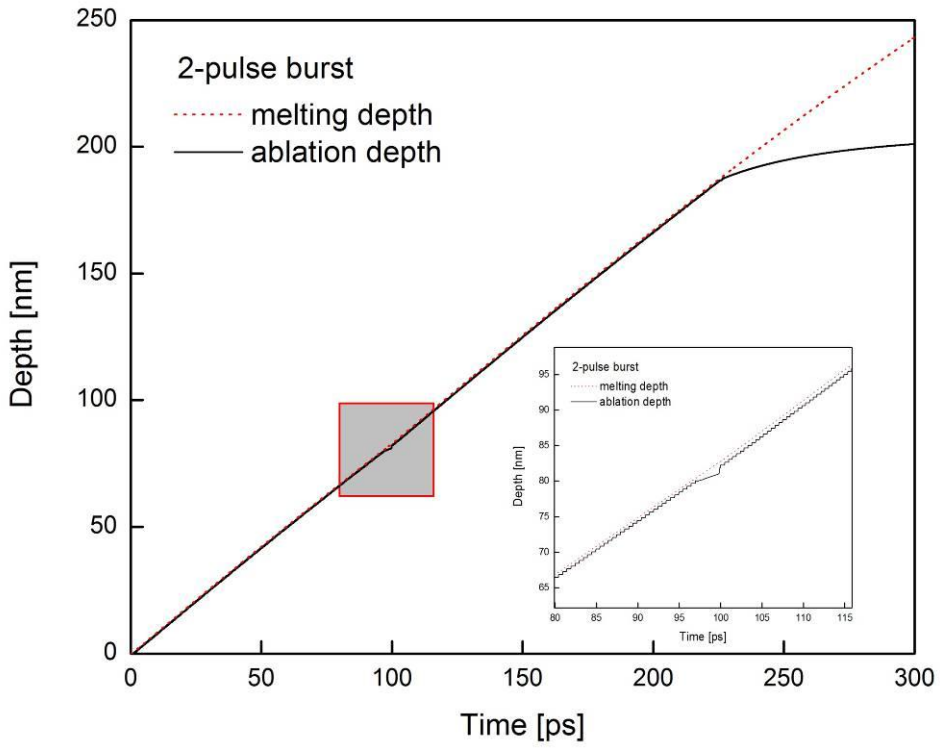

(a) 2-pulse burst

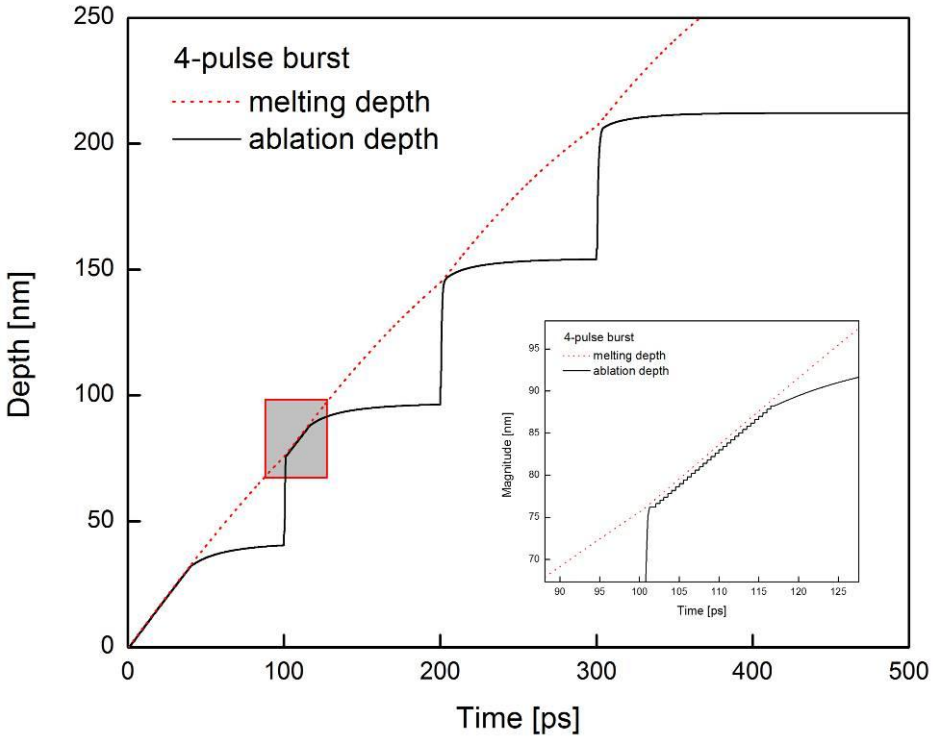

(b) 4-pulse burst

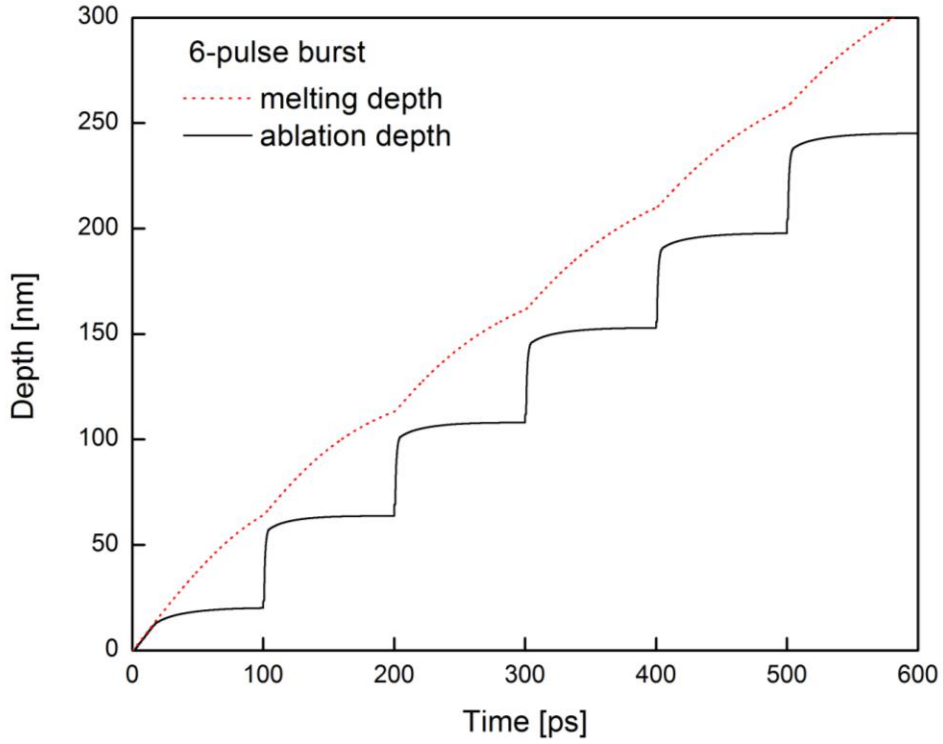

(c) 6-pulse burst

Figure 7.8 Evolution of ablation and melting for with 100 ps separation time: (a) 2-pulse burst, (b) 4-pulse burst, (c) 6-pulse burst

It is worthy noticing the results in Fig. 7.5 again. The increase of ablation depth with pulse number is not always remarkable and monotonic; for example, the bursts composing of 4 pulses with 100-ps separation time, 8 pulses with 50-ps separation time, and 10 pulses with 500-ps separation time. In the first two cases, the ablation depths slightly increase and decrease respectively from the previous one and then increase significantly to the following one. The reasons may be found in Fig. 7.8, where the dashed lines denote melting depth and the solid lines the ablation depth. For the 2-pulse burst case shown in Fig. 7.8(a), the resulting liquid layer is always very thin during the entire phase explosion process. As explained previously, the phase explosion repeatedly takes place almost immediately when the liquid phase is transformed from the superheated solid phase induced by the huge thermal energy that is transferred from the hot electrons. After the phase explosion stops, vaporization takes place at a much slower ablation rate, see Fig. 7.8(a). This ablation process is very similar to that found in the single pulse case (Fig. 7.6), except for a violent (though small) phase explosion caused by the second laser pulse. For the 4-pulse burst case shown in Fig. 7.8(b), a violent phase explosion always occurs right after the impinging of each subsequent laser pulse. It should be noted here that the relatively slow phase explosion is only triggered by the second pulse in this case. During this relatively slow phase explosion, the liquid layer is very thin as those observed in the cases of the single pulse and the 2-pulse burst. However, no relatively slow phase explosion is found in Fig. 7.8(c) for the 6-pulse burst. This gives rise to a possibility for reducing the ablation depth in the 4-pulse burst case

due to less thermal energy for material ablation. The reason is that a part of the concentrated heat conducts into deeper part of the material during the relatively slow phase explosion. Similar ablation phenomena are also found in the cases of laser bursts consisting of 6, 8 and 10 pulses with 50-ps separation time, among which the 8-pulse burst yields the smallest ablation depth. For brevity, those results are not presented here.

For the bursts with a separation time of 500 ps, the phenomena of melting and ablation are basically similar to those observed in the 6-pulse burst case with 100-ps pulse separation time (Fig. 7.8(c)). No relatively slow phase explosion occurs after each violent phase explosion resulting from the subsequent pulses. However, as shown in Figs. 7.9(a) and 7.9(b) for the 6-pulse and 8-pulse bursts respectively, the liquid layers grow much thicker and also experiences a re-solidification revealed by the drop of melting depth in between the first and second pulses. Because the pulse separation time is sufficiently long, there is enough time for a part of the concentrated thermal energy in the hot electrons to diffuse away, leading to less energy to heat up the liquid lattice to the critical temperature for phase explosion. Therefore, the liquid layer becomes thicker and thicker after each pulse irradiation. The reason for the reduction in the amount of material ablated by the 10-pulse burst is different from that for the bursts of 4 pulses with 100-ps separation time and 8 pulses with 50-ps separation time as discussed previously. It may be due to the fact that much less energy contained in the pulses results in a lower electron and lattice temperature, leading to a higher reflectivity and not as much of laser energy absorbed by the material. As a result, less material ablated is expected. Owing to the heat

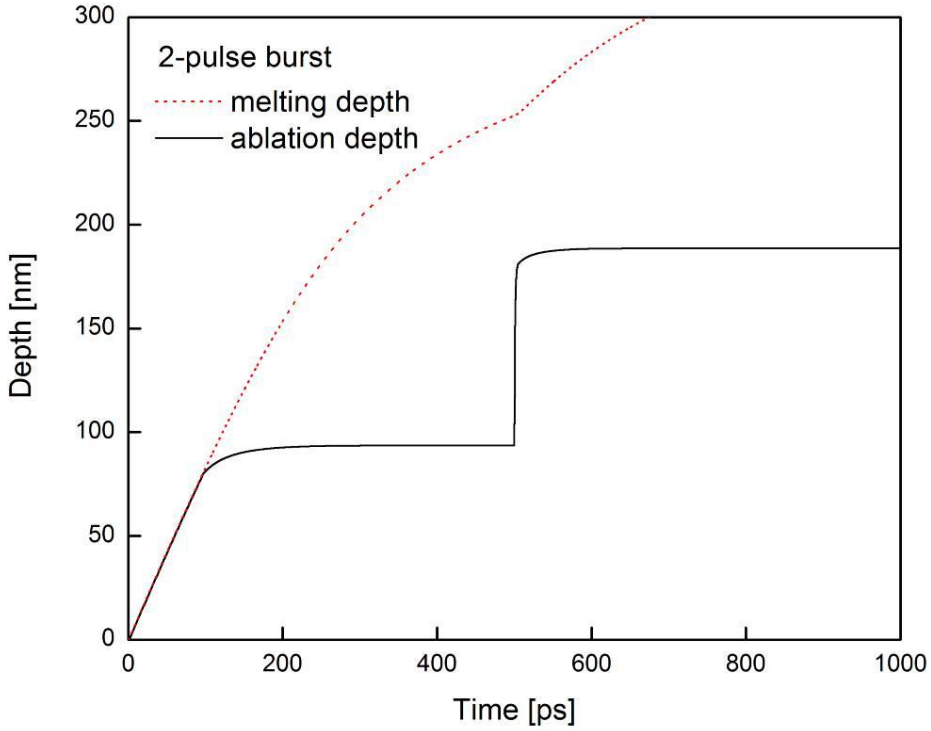

(a) 2-pulse burst

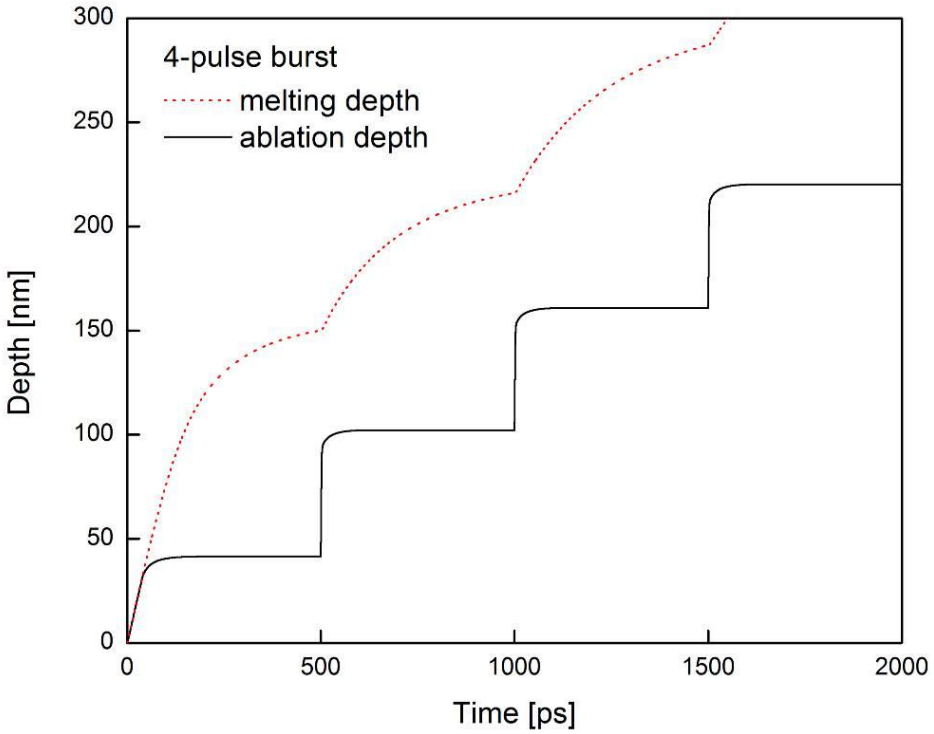

(b) 4-pulse burst

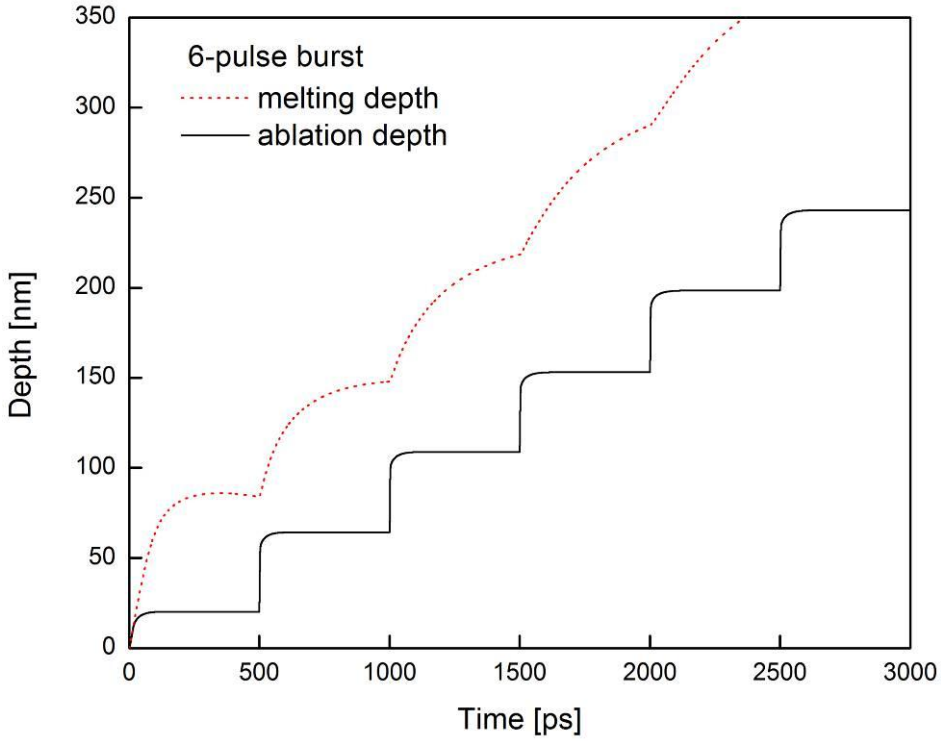

(c) 6-pulse burst

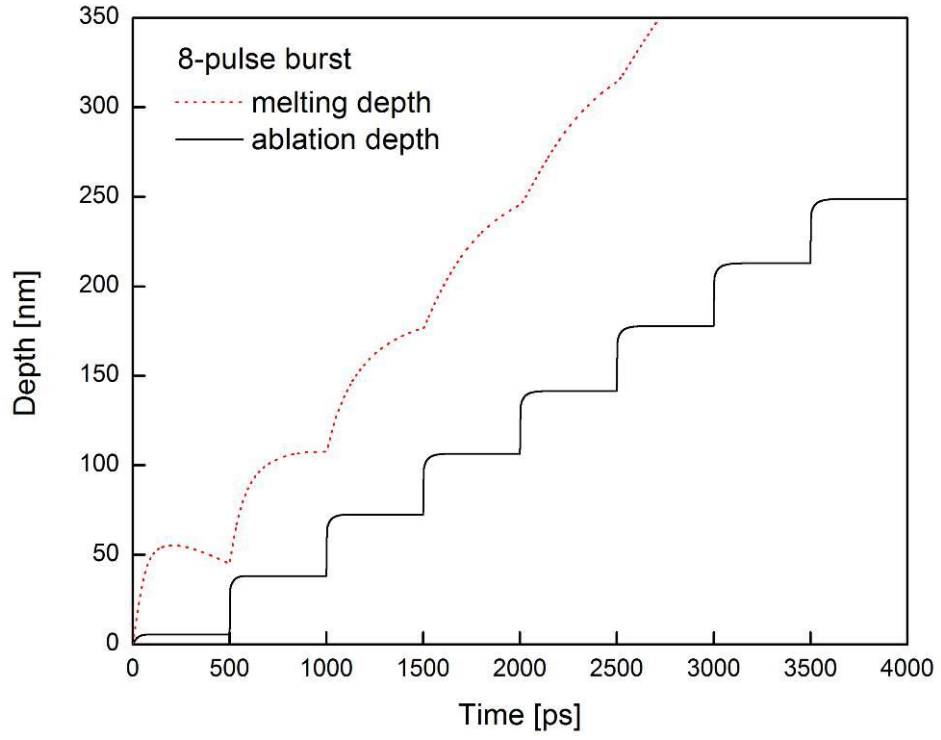

(d) 8-pulse burst

Figure 7. 9 Melting and ablation process for different pulse number with 500 ps separation time: (a) 2-pulse burst, (b) 4-pulse burst, (c) 6-pulse burst, (d) 8-burst

diffusing to the inner part of material during the long separation time between the pulses, the ablation depths generally are smaller than those yielded by the bursts with the 100-ps separation time.

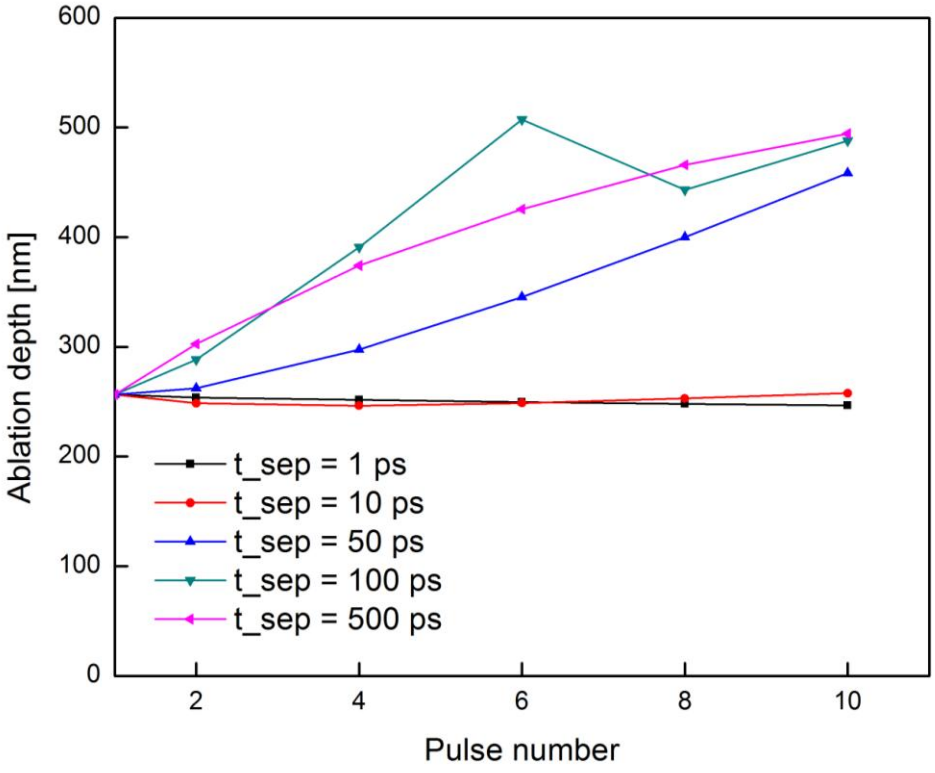

Figure 7. 10 Ablation depths induced by single shot and burst mode with total fluence of 10 J/cm^2

Figure 7.10 shows the ablation depths for the bursts having a total laser fluence of 10 J/cm^2. In general, more material can be ablated by this burst mode if the pulse separation time is not too short. It is noted that the trend of ablation depths against pulse number is not identical to that found in the case of 5 J/cm^2. This is attributed to the different dependency of each of the four competing mechanisms, absorption of laser energy, electron-lattice thermalization, heat conduction, and material ablation, on the total laser energy. Together with the results of material ablation by the laser bursts at the total

fluence 5 J/cm^2 shown previously, it may be concluded that for a given fluence, material ablation can be optimized by properly selecting a combination of pulse number and separation time in an ultrashort laser burst.

It should be noted here that the simulated temperatures in an superheated solid lattice shown in Fig. 7.7(a) are over 32,000 K, which seems to be impossible. Interestingly, the similar results for such high temperatures in an overheated solid phase have also been reported recently by Mazhukin et al. [82]. Whether such an incredibly high temperature is real or not remains unknown. Further investigation of high temperature material science on this bizarre result is suggested.

7.3 Conclusion

In this chapter, numerical simulations of laser ablation of copper films were carried out using the proposed comprehensive thermal model, including a two temperature model, two phase change models for melting and evaporation under superheating, and a phase explosion criterion for ejection of metastable liquid and vapor. It was shown that the model simulations of material ablation by a single pulse correlate well with the experimental data over a broad range of laser fluences from 0.6 – 30 J/cm^2. The good correlation suggests that the present model is an efficient and accurate tool for predicting ultrafast laser material ablation. The study of material ablation by burst modes found that four mechanisms - absorption of laser energy, heat conduction, electron-lattice thermalization, and material ablation – are competing with one another during the entire laser ablation process. For pulse separation times of 50 ps or longer, a burst mode can

significantly increase the amount of material ablated, compared to a single pulse with the same fluence of the burst. It was also shown that with a given laser fluence the material ablation can be optimized by properly selecting a combination of pulse number and separation time in a laser burst. One interesting result was that the simulated temperature in the overheated solid lattice is over 32,000 K, which was also reported recently by Mazhukin et al. [82]. Further investigation of high temperature material science on this bizarre result is suggested.

CHAPTER 8: CONCLUSION

The extended Drude model and the critical point model with three Lorentzian terms were proposed to characterize temperature-dependent optical reflectivity and absorption coefficient for gold and copper, respectively. These optical models were first validated with experimental data at room temperature. After that, the models were incorporated into a classical and semi-classical two temperature model (TTM) together with temperature-dependent thermophysical properties to simulate energy transport, rapid phase changes, and thermal ablation of metal films induced by ultrashort-pulsed lasers.

It was found that significant changes in surface reflectivity and absorption coefficient due to rapid rises of electron and lattice temperature could drastically alter laser energy deposition and in turn, the thermal response in a metal film. This suggests that the constant values of reflectivity and absorption coefficient at room temperature that have been widely employed in a TTM are only adequate for very low laser fluencies. For a metal target subjected to ultrafast pulse irradiation with fluences exceeding melting threshold, temperature-dependent optical properties should be adopted in the TTM.

The critical point model with three Lorentzian terms was used to study the energy transport and phase changes in copper films irradiated by a single ultrafast laser pulse. The averaged absorption of laser energy is matched well with experimental results. It was also shown that for the same peak laser intensity the longer the laser pulse, the higher the energy absorption. In addition, the laser energy density distribution in a metal film could

no longer follow Beer's law when temperature-dependent optical properties are used.

The difference between the classical and semi-classical TTM was investigated by employing temperature-dependent optical and thermophysical properties. The results showed that the semi-classical TTM generally predicts lower electron and lattice temperature due to the electron drifting effect. The difference could be more distinct with increase of laser fluence and/or increase of laser pulse duration. The peak electron temperatures at the irradiated surface obtained from the two models could be close for 100-fs pulse but be quite different for longer pulses such as a 10-ps pulse.

The investigation of the effects of pulse number and separation time in a laser burst on thermal response showed that with the same total energy in a femtosecond laser burst, more pulses with shorter separation time or fewer pulses with longer separation time could induce higher lattice temperature. For a dual laser beam consisting of a nanosecond pulse and a femtosecond laser burst, the lattice temperature can be increased by setting the pulse separation time in a burst as short as possible.

Thermal ablation of copper films by a single pulse was also investigated. The simulated material ablation correlated well with the experimental data over a broad range of laser fluences from 0.6 – 30 J/cm^2. This suggests that the proposed comprehensive thermal model is an efficient and accurate tool for predicting ultrafast laser material ablation. It was also found that phase explosion is the dominating mechanism for laser ablation at high fluences, and vaporization at low fluences.

The study for laser material ablation by laser bursts showed that for very short separation time, e.g., 1 ps and 10 ps, the ablation depth by a ultrashort laser burst is close to that by a single pulse. With longer separation time, e.g., 50 ps or longer, the advantage of burst mode becomes evident. In general, the more the pulse number, the deeper the ablation depth. At a given fluence, the material ablation can be optimized by properly selecting a combination of pulse separation time and pulse number in an ultrashort laser burst.

Further investigations on the axisymmetric and 3D problems using the present model are suggested. In these problems, the walls of ablated craters or grooves will be inclined if laser beams are Gaussian in space and could considerably change beam reflection. Therefore, the laser energy deposition into the targets must be characterized by taking into account the beam deflection effects. In addition, the changing in the surface optical properties due to increasing roughness should be addressed. These are particularly important for the laser bursts. Also, proper algorithms for numerical analysis of multi-dimensional material removal by vaporization and phase explosion should be implemented. More different metal materials such as aluminum, nickel, and steel are suggested in these studies for real applications.

REFERENCES

[1] http://en.wikipedia.org/wiki/Laser

[2] M. J. Weber, *Handbook of Laser Wavelengths*, CRC Press, Boca Raton, 1999.

[3] S. I. Anisimov, B. L. Kapeliovich, T. L. Perel'man, Electron emission from metal surfaces exposed to ultrashort laser pulses, Sov. Phys. JETP, 39, 1974, 375-377.

[4] G. L. Eesley, Generation of nonequilibrium electron and lattice temperatures in copper by picosecond laser pulses, Physical Review B, 33, 1986, 2144-2152.

[5] S. -S. Wellershoff, J. Hohlfeld, J. Güdde, E. Matthias, The role of electron-phonon coupling in femtosecond laser damage of metals, Applied Physics A: Materials Science & Processing, 69 [Suppl.], 1999, S99-S107.

[6] S. Nolte, C. Momma, H. Jacobs, A. Tunnermann, B. N. Chichkov, B. Wellegehausen, Ablation of metals by ultrashort laser pulses, J. Opt. Soc. Am. B, 14, 1997, 2716-2722.

[7] S. Kuper, M. Stuke, Ablation of polytetrafluoroethylene (Teflon) with femtosecond UV excimer laser pulses, Applied Physics Letters, 54, 1988, 4-6.

[8] B. N. Chichkov, C. Momma, S. Nolte, F. von Alvensleben, A. Tunnermann, Femtosecond, picosecond, and nanosecond laser ablation of solids, Applied Physics A: Solids Surface, 63, 1996, 109-115.

[9] P. P. Pronko, S. K. Dutta, J. Squier, J. V. Rudd, D. Du, G. Mourou, Machining of sub-micron holes using a femtosecond laser at 800 nm, Optical Communications, 114, 1995, 106-110.

[10] G. Herbst, M. Stainer, G. Marowsky, E. Matthias, Ablation of Si and Ge using UV femtosecond laser pulses, Mater. Res. Soc. Symp. Proc., 397, 1996, 69-74.

[11] E. N. Glezer, L. Huang, Y. Siegal, J. P. Callan, E. Mazur, Phase transition induced by femtosecond pulses, Mater. Res. Soc. Symp. Proc., 397, 1996, 3-20.

[12] K. Baheti, An axisymmetric Interfacial tracking model for melting-vaporization -resolidification in a thin metal film irradiated by pico to femtosecond pulse lasers, University of Missouri-Columbia, 2010.

[13] Y. Zhang, J. K. Chen, An interfacial tracking method for ultrashort pulse laser melting and resolidification of a thin metal film, Journal of Heat Transfer, 130, 2008, 062401.

[14] F. J. Duarte, *Tunable Laser Applications* (2nd ed.), CRC Press, Boca Raton, 2008.

[15] F. J. Duarte, L. M. Hillman, *Dye Laser Principles*, Academic Press, Boston, 1990.

[16] A. V. Borovsky, A. L. Galkin, O. B. Shiryaev, T. Auguste, *Laser Physics at Relativistic Intensities*, Springer, New York, 2010.

[17] M. Braun, P. Gilch, W. Zinth, *Ultrashort Laser Pulses in Biology and Medicine*, Springer, New York, 2010.

[18] P.-H. Barret, M. Palmer, *High-Power and Femtosecond Lasers: Properties, Materials and Applications*, Nova, New York, 2009.

[19] K. Sugioka, M. Meunier, A. Piqué, *Laser Precision Microfabrication*, Springer, New York, 2010.

[20] A. Miotello, P. M. Ossi, *Laser-Surface Interactions for New Materials Production*, Springer, New York, 2010.

[21] J. Hohlfeld, S. -S. Wellershoff, J. Gudde, U. Conrad, V. Jahnke, E. Matthias, Electron and lattice dynamics following optical excitation of metals, Chem. Phys.,

251, 2000, 237–258.

[22] T. Q. Qiu, C. L. Tien, Heat transfer mechanisms during short-pulse laser heating of metals, ASME Journal of Heat Transfer, 115, 1993, 835-841.

[23] D. Y. Tzou, *Macro-Microscale Heat Transfer*, Taylor & Francis, Washington DC, 1997.

[24] J. K. Chen, J. E. Beraun, Numerical study of ultrashort laser pulse interactions with metal films, Numerical Heat Transfer A, 40, 2001, 1-20.

[25] N. W. Ashcroft, N. D. Mermin, *Solid State Physics*, Saunders College, Philadelphia, 1976.

[26] C. M. Snowden, *Introduction to Semiconductor Device Modeling*, World Science, Singapore, 1986.

[27] J. K. Chen, D. Y. Tzou, J. E. Beraun, A semiclassical two temperature model for ultrafast laser heating, International Journal of Heat and Mass Transfer, 49, 2006, 307-316.

[28] T. Q. Qiu, C. L. Tien, Femtosecond laser heating of multi-layer metals-I. Analysis, International Journal of Heat and Mass Transfer, 37, 1994, 2789-2797.

[29] S. I. Anisimov, B. Rethfeld, On the theory of ultrashort laser pulse interaction with metal, SPIE, 3093, 1997, 192-203.

[30] L. Jiang, H. L. Tsai, Energy transport and material removal in wide bandgap materials by a femtosecond laser pulse, International Journal of Heat and Mass Transfer, 48, 2005, 487-499.

[31] Z. Lin, L. V. Zhigilei, Electron-phonon coupling and electron heat capacity of metals under conditions of strong electron-phonon nonequilibrium, Physical Review B, 77,

2008, 075133.

[32] L. Jiang, H. L. Tsai, Prediction of crater shape in femtosecond laser ablation of dielectrics, Journal of Physics D: Applied Physics, 37, 2004, 1492-1496.

[33] L. Jiang, H. L. Tsai, Modeling of ultrashort laser pulse-train processing of metal thin films, International Journal of Heat and Mass Transfer, 50, 2007, 3461-3470.

[34] H. S. Sim, S. Park, T.-H. Kim, Y. K. Choi, J. S. Lee, S. H. Lee, Femtosecond laser pulse train effect on optical characteristics and nonequilibrium heat transfer in thin metal films, Materials Transactions, 51, 2010, 1156-1162.

[35] D. Fisher, M. Fraenkel, Z. Henis, E. Moshe, S. Eliezer, Interband and intraband (Drude) contributions to femtosecond laser absorption in aluminum, Physical Review E, 65, 2001, 016409.

[36] D. Fisher, M. Fraenkel, Z. Zinamon, Z. Henis, E. Moshe, Y. Horovitz, E. Luzon, S. Maman, S. Eliezer, Intraband and interband absorption of femtosecond laser pulse in copper, Laser and Particle Beams, 23, 2005, 391-393.

[37] A. Y. Vorobyev, C. Guo, Change in absorptance of metals follwing multi-pulse femtosecond laser ablation, Journal of Physics: Conference Series, 59, 2007, 579-584.

[38] A. Y. Vorobyev, C. Guo, Femtosecond laser blackening of metals, Midwest Symposium on Circuits and Systems, 5235913, 2009, 905-908.

[39] L. -S. Kuo, T. Qiu, Microscale energy transfer during picosecond laser melting of metal films, ASME National Heat Transfer Conference, 1, 1996, 149-157.

[40] J. K. Chen, J. E. Beraun, Modeling of ultrashort laser ablation of gold films in vacuum, Journal of Optics A: Pure and Applied Optics, 5, 2003, 168-173.

[41] X. Xu, G. Chen, K. H. Song, Experimental and numerical investigation of heat

transfer and phase change phenomena during excimer laser interaction with nickel, International Journal of Heat and Mass Transfer, 42, 1999, 1371-1382.

[42] J. Huang, Y. Zhang, J. K. Chen, Superheating in liquid and solid phases during femtosecond-laser pulse interaction with thin metal Film, Applied Physics A: Material Science and Processing, 102, 2011, 1-9.

[43] F. D. Bennett, in Physics of High Energy Density, edited by P. Caldirola, and H. Knoepfel, Academic Press, New York, 1971.

[44] I. H. Chowdhury, X. Xu, Heat transfer in femtosecond laser processing of metal, Numerical Heat Transfer, Part A, 44, 2003, 219-232.

[45] J. Huang, Y. Zhang, J. K. Chen, M. Yang, Modeling of ultrafast phase change processes in a thin metal film irradiated by femtosecond laser pulse trains, Journal of Heat Transfer, 133, 2011, 031003.

[46] D. Bäuerle, *Laser Processing and Chemistry*, Springer, New York, 2000.

[47] C. Schäfer, H. M. Urbassek, L. V. Zhigilei, Metal ablation by picosecond laser pulses: a hybrid simulation," Physics Review B, 66, 2002, 115404.

[48] S. Nolte, C. Momma, H. Jacobs, A. Tunnermann, B. N. Chichkov, B. Wellegehausen, Ablation of metals by ultrashort laser pulses, J. Opt. Soc. Am. B, 14, 1997, 2716-2722.

[49] S. Preuss, A. Demchuk, M. Stuke, Sub-picosecond UV laser ablation of metals, Appl. Phys. A: Mater. Sci. Process, 61, 1995, 33-37.

[50] R. Fang, D. Zhang, H. Wei, Z. Li, F. Yang, Y. Gao, Improved two-temperature model and its application in femtosecond laser ablation of metal target, Laser and Particle Beams, 28, 2010, 157-164.

[51] A. M. Chen, H. F. Xu, Y. F. Jiang, L. Z. Sui, D. J. Ding, H. Liu, M. X. Jin, Modeling of femtosecond laser damage threshold on the two-layer metal films, Applied Surface Science, 257, 2010, 1678-1683.

[52] M. M. Martynyuk, Vaporization and boiling of liquid metal in an exploding wire, Sov. Phys.-Tech. Phys., 19, 1974, 793-797.

[53] J. Zhang, Y. Zhao, X. Zhu, Theoretical studies of ultrafast ablation of metal targets dominated by phase explosion, Applied Physics A, 89, 2007, 571-578.

[54] R. Kelly, A. Miotello, Comments on explosive mechanisms of laser sputtering, Appl. Surf. Sci. 96-98, 1996, 205-215.

[55] D. A. Willis, X. Xu, Heat transfer and phase change during picosecond laser ablation of nickel, Int. J. Heat Mass Tran., 45, 2002, 3911-3918.

[56] Y. Ren, J. K. Chen, Y. Zhang, Optical properties and thermal response of copper films induced by ultrashort-pulsed lasers, Journal of Applied Physics, 110, 2011, 113102.

[57] P. G. Klemens, R. K. Williams, Thermal conductivity of metals and alloys, International Metals Review, 31, 1986, 197-244.

[58] J. K. Chen, W. P. Latham, J. E. Beraun, The role of electron-phonon coupling in ultrafast laser heating, Journal of Laser Applications, 17, 2005, 63-68.

[59] Y. Ren, J. K. Chen, Y. Zhang, J. Huang, Ultrashort laser pulse energy deposition in metal films with phase changes, Applied Physics Letters, 98, 2011, 191105.

[60] A. D. Rakić, A. B. Djurišić, J. M. Elazar, M. L. Majewski, Optical properties of metallic films for vertical-cavity optoelectronic devices, Applied Optics, 37, 1998, 5271-5283.

[61] P. G. Etchegoin, E. C. Le Ru, M. Meyer, An analytical model for the optical properties of gold, Journal of Chemical Physics, 125, 2006, 164705.

[62] A. Vial, T. Laroche, Comparison of gold and silver dispersion laws suitable for FDTD simulations, Applied Physics B, 93, 2008, 139-143.

[63] S. Kirkpatrick, C. D. Gelatt, M. P. Vecchi, Optimization by simulated annealing, Science, 220, 1983, 671-680.

[64] M. Fox, *Optical Properties of Solids*, Oxford University Press, New York, 2010.

[65] A. Faghri, Y. Zhang, *Transport Phenomena in Multiphase Systems*, Elsevier Academic Press, Burlington, 2006.

[66] R. Courant, K. O. Friedrichs, *Supersonic Flow and Shock Waves*, Interscience Publishers, New York, 1976.

[67] F. D. Bennett, Vaporization-wave transitions, Physics of High Energy Density, edited by P. Caldirola, H. Knoepfel, 1969, 217-229.

[68] G. D. Kahl, Generalization of the Maxwell criterion for Van der Waals equation, Physical Review, 155, 1967, 78-80.

[69] J. Huang, Y. Zhang, J. K. Chen, Ultrafast solid-liquid-vapor phase change of a gold film induced by pico- to femtosecond lasers, Applied Physics A, 95, 2009, 643-653.

[70] R. Kelly, A. Miotello, Contribution of vaporization and boiling to thermal-spike sputtering by ions or laser pulses, Physical Review E, 60, 1999, 2616-2625.

[71] N. M. Bulgakova, I. M. Bourakov, Phase explosion under ultrashort pulsed laser ablation: modeling with analysis of metastable state of melt, Applied Surface Science, 197-198, 2002, 41-44.

[72] V. R. Voller, An overview of numerical methods for solving phase change problems,

Advances in Numerical Heat Transfer, 1, 1997, 341-380.

[73] K. Sasaguchi, A. Ishihara, H. Zhang, Numerical study on utilization of melting of phase change material for cooling of a heated surface at a constant rate, Numerical Heat Transfer, Part A, 29, 1996, 19–31.

[74] B. Binet, M. Lacroix, Melting from heat sources flush mounted on a conducting vertical qall, International Journal of Numerical Methods Heat Fluid Flow, 10, 2000, 286–306.

[75] K. Morgan, A numerical analysis of freezing and melting with convection, Comput. Methods Appl. Mech. Eng., 28, 1981, 275–284.

[76] J. S. Hsiao, An efficient algorithm for finite difference analysis of heat transfer with melting and solidification, 1984, ASME Paper No. 84-WA/HT-42.

[77] Y. Cao, A. Faghri, A numerical analysis of phase change problem including natural convection, ASME J. Heat Transfer, 112, 1990, 812–815.

[78] P. B. Johnson, R. W. Christy, Optical constant of the noble metals, Physical Review B, 6, 1972, 4370-4379.

[79] J. Huang, Y. Zhang, J. K. Chen, M. Yang, Modeling of ultrafast phase change processes in a thin meta film irradiated by femtosecond laser pulse trains, Journal of Heat Transfer, 133, 2011, 031003.

[80] H. Hess, Critical data and vapor pressures of aluminium and copper, Z. Metallkd. 89, 1998, 388-393.

[81] M. Hashida, A. F. Semerok, O. Gobert, G. Petite, Y. Izawa, J. F. Wagner, Ablation threshold dependence on pulse duration for copper, Appl. Surf. Sci. 197, 2002, 862-867.

[82] A. V. Mazhukin, V. I. Mazhukin, M. M. Demin, Modeling of femtosecond ablation of aluminum film with single laser pulses, Appl. Surf. Sci. 257, 2011, 5443-5446.

VITA

The author, Yunpeng Ren, was born in Shandong province, China in 1982. In 2005, he got a Bachelor degree of Materials Science and Engineering from China University of Petroleum in China, and in 2008, he obtained a Master degree of Materials Science from China University of Petroleum in China. After that, in May 2008, he came to University of Missouri-Columbia to pursue PhD degree of Mechanical Engineering. Research interests include materials science, heat transfer, and mechanical engineering.